$\mathbb{E}$ Double-polarisation Observable for $\gamma n \to K^+\Sigma^-$ from $g14$ (HDice) Data

Jamie A. Fleming
University of Edinburgh

CLAS Analysis Note
Draft 1.1
Feb 2017

Abstract

This analysis note presents the first measurement of the $\mathbb{E}$ double-polarisation observable for the exclusive $\gamma n \rightarrow K^+\Sigma^-$ reaction using a polarised hydrogen-deuterium target from the $g14$ (HDice) run period at CLAS. Circularly polarised photons of energies between 1.1 and 2.3 GeV were used, with results shown in 200 MeV bins in E_γ and bins of 0.4 in $\cos\theta_{K^+}^{C.M.}$.

The $g14$ experiment ran, and data were collected, during the period December 2011 to May 2012.

Preface

The material for this analysis note is based on the CLAS thesis "First Measurement of the $\mathbb{E}$ Double-polarization Observable for the $\gamma n \rightarrow K^{+}\Sigma^{-}$ with CLAS & a New Forward Tagger Hodoscope for CLAS12" by Jamie A. Fleming (*November* 2016)[1].

[1]https://www.jlab.org/Hall-B/general/thesis/Fleming_thesis.pdf

Contents

List of Figures

List of Tables

Chapter 1

Introduction

Experiments involving photoproduction are now commonly used in order to study the excitation spectrum of the nucleon. In this chapter, the motivation for such experiments will be discussed, as well as the method for extracting the $\mathbb{E}$ double-polarisation observable. The basis of the theoretical models used to compare with data will also be discussed.

1.1 Motivation

Establishing the excitation spectrum of the nucleon would be a key advance to further our understanding of nucleon structure and Quantum Chromodynamics (QCD). Recent theoretical advances allow predictions of the excitation spectrum of the nucleon and other nucleon properties directly from QCD in the non-perturbative regime, via numerical methods (such as Lattice QCD), which complements existing phenomenological theories such as constituent quark models. The excited states are predicted to have different couplings to the proton and neutron; experimental data on neutron targets is therefore of paramount importance for a full determination of the spectrum.

1.2 Extracting the $\mathbb{E}$ Double-Polarisation Observable

The channel described in this note is the $\gamma n \to K^+\Sigma^-$ with a circularly polarised photon beam and a longitudinally polarised neutron target.

The differential cross section for meson photoproduction from a polarised nucleon target using a polarised photon beam, can be separated into three expressions dependent upon the type of double-polarisation experiment being conducted [1]. Considering an experiment with polarised photons incident on a polarised target:

$$\begin{aligned} \frac{d\sigma}{d\Omega} = \left(\frac{d\sigma}{d\Omega}\right)_0 [1 &- P_{lin}\Sigma\cos(2\phi) \\ &+ P_x(-P_{lin}\mathbb{H}\sin(2\phi) + P_{circ}\mathbb{F}) \\ &+ P_y(\mathbb{T} - P_{lin}\mathbb{P}\cos(2\phi)) \\ &+ P_z(P_{lin}\mathbb{G}\sin(2\phi) - P_{circ}\mathbb{E})]. \end{aligned} \tag{1.1}$$

Considering an experiment with Beam-Recoil measurements:

$$\begin{aligned} \frac{d\sigma}{d\Omega} = \left(\frac{d\sigma}{d\Omega}\right)_0 [1 &- P_{lin}\Sigma\cos(2\phi) \\ &+ P_{x'}(-P_{lin}\mathbb{O}_{x'}\sin(2\phi) - P_{circ}\mathbb{C}_{x'}) \\ &+ P_{y'}(\mathbb{P} - P_{lin}\mathbb{T}\cos(2\phi)) \\ &+ P_{z'}(-P_{lin}\mathbb{O}_{z'}\sin(2\phi) - P_{circ}\mathbb{C}_{z'})]. \end{aligned} \tag{1.2}$$

Finally, considering an experiment with Target-Recoil measurements:

$$\begin{aligned} \frac{d\sigma}{d\Omega} = \left(\frac{d\sigma}{d\Omega}\right)_0 [1 &+ P_y\mathbb{T} + P_{y'}\mathbb{P} \\ &+ P_{x'}(P_x\mathbb{T}_{x'} - P_z\mathbb{L}_{x'}) \\ &+ P_{y'}P_y\Sigma \\ &+ P_{z'}(P_x\mathbb{T}_{z'} + P_z\mathbb{L}_{z'})]. \end{aligned} \tag{1.3}$$

In this analysis note, the observable of interest is the Beam-Target observable $\mathbb{E}$. In order to isolate the observable $\mathbb{E}$, a circularly polarised photon beam and a longitudinally polarised target must be used. Other components of the target polarisation are therefore zero, $P_x = P_y = 0$, while there is no contribution from a linearly polarised photon beam, $P_{lin} = 0$. We simplify our expression for the Beam-Target differential cross section, Equation 1.1, using these conditions:

$$\frac{d\sigma}{d\Omega} = \left(\frac{d\sigma}{d\Omega}\right)_0 [1 - P_\gamma P_\oplus \mathbb{E}], \tag{1.4}$$

where P_γ is the polarisation of the incident photon and $P_\oplus$ is the polarisation of the target. The observable $\mathbb{E}$ can be extracted from the beam-asymmetry [2], $\mathcal{A}$, which is defined as:

$$\mathcal{A} = \frac{N_{\frac{1}{2}}(\rightarrow\Leftarrow) - N_{\frac{3}{2}}(\leftarrow\Leftarrow)}{N_{\frac{1}{2}}(\rightarrow\Rightarrow) + N_{\frac{3}{2}}(\leftarrow\Rightarrow)}, \tag{1.5}$$

where N represents the appropriate number of events for the corresponding target ($\rightarrow$) and beam ($\Rightarrow$) polarisation vectors. The beam-asymmetry is then used in conjunction with the target and photon polarisations to give an expression for the double-polarisation observable $\mathbb{E}$:

$$\mathbb{E} = \frac{1}{P_\gamma P_\oplus}\mathcal{A}. \tag{1.6}$$

1.3 Theoretical Models for Meson Photoproduction

Information on the nucleon resonance spectrum is extracted by fitting a model to experimental data and fitting parameters in the model to extract the masses, widths and quantum numbers of the contributing resonances [3]. This fitting separates the contributions from different angular momenta, referred to as a ***P***artial ***W***ave ***A***nalysis (PWA) [4].

These models consider the processes as being comprised of a resonant and background component. These components are parametrised and extracted from the experimental data through fitting. As with many models, the more experimental data which is available, the more constraints can be placed upon the reaction channel to provide more accurate and less ambiguous results.

If we consider a generic reaction where we have a photon-nucleon interaction, a, with some intermediate resonance state, c, which finally ends in a meson-nucleon system, b, the Hamiltonian can be written as:

$$\mathcal{H} = \mathcal{H}_0 + \mathcal{V}, \tag{1.7}$$

where the first term is the free Hamiltonian, $\mathcal{H}_0$, and the second is the interaction term, $\mathcal{V}$. As is a common feature of reaction models, this interaction term is split into a resonant component, $\mathcal{V}_R$, and a background component, $\mathcal{V}_B$:

$$\mathcal{V} = \mathcal{V}_R(E) + \mathcal{V}_B, \tag{1.8}$$

where the resonant component is a function of the total energy, E.

The probability of the process to occur is governed by a transition matrix, T_{ba}, which can be similarly reduced into components:

$$T_{ba}(E) = T^R_{ba}(E) + T^B_{ba}. \tag{1.9}$$

The resonant component of this transition matrix can be expanded by summing over all possible paths in the process $a \to c \to b$, and introducing a propagator of state c, g_c:

$$T_{ba}(E) = \sum_c \mathcal{V}_{ba} g_c(E) T_{bc}(E) + \mathcal{V}_{ba}. \tag{1.10}$$

1.3.1 Isobar Models

Isobar models attempt to use an *effective* Lagrangian to simulate the properties of interactions. They do this by evaluating tree-level Feynman diagrams for the resonant and non-resonant exchange of mesons and baryons. By considering the possible exchanges which take place in s-, t- and u-channel reactions, excited states can be identified. This tree-level method is useful to simplify the interaction to first order, but neglects to take into account effects such as interactions in the final state or coupled-channel effects.

The isobar model we will consider in this analysis note is the KaonMAID model [5][1]. The model considers low-order diagrams for the interaction, which are then split into resonant and non-resonant terms (Born terms). The s-channel mechanism represents the resonant contributions, while the t- and u-channel mechanisms represent the background contribution.

These isobar models have seen much use in the energy region under 2 GeV due to the smaller importance of higher order diagrams and Born terms at lower energies. The models attempt to produce theoretical predictions of polarisation observables using various combinations of resonances, which allows for comparison between data and prediction in order to infer the presence or absence of a resonance. This is not a trivial procedure as many partial waves can be present and interfere strongly.

1.3.2 Coupled-Channel Analysis

Coupled-***C***hannel (CC) analysis is an attempt to improve the accuracy of the isobar model to include final state particle interactions, as well as intermediate states such as πN[2]. These processes can be described as production of a non-resonant state which rescatters from the nucleon in order to produce a resonance.

Coupled-channel analysis also hopes to reduce the ambiguity of resonance combinations used to fit data [6]. As it is possible for more than one combination of resonances to fit the data well, this disambiguous nature can be removed by considering multiple observables on multiple final states. This analysis method allows more constraints to be added to the channel which acts as a filter to remove resonances which do not contribute to the final state.

The model we consider in this analysis note is the ***Bo***nn-***Ga***tchina (BoGa) model[3]. This coupled-channel model aims to consider multiple decay channels at once, with angular and energy dependencies of different observables are analysed simultaneously [7]. This provides stable fits for partial waves with high spin and provides a smooth behaviour in energy.

Two particle final states, such as πN, ηN, $K\Lambda$, $K\Sigma$, ωN and $K^*\Lambda$ are

[1]Maintained and developed by the Institut für Kernphysik, Universität Mainz, Germany.

[2]Amplitudes of $\gamma N \rightarrow \pi N$ process is thought to play a considerable effect in the overall process $\gamma N \rightarrow \pi N \rightarrow KY$, where Y is a final state hyperon.

[3]Maintained and developed by the Helmholtz-Institut für Strahlen- und Kernphysik, Universität Bonn, Germany; and Kurchatov Institute, ***P***etersburg ***N***uclear ***P***hysics ***I***nstitute (PNPI), Gatchina, Russia.

fitted with the χ^2 method. At fixed energies, the unpolarised cross section of pseudoscalar mesons is characterised by the differential cross section only. For vector mesons however, the unpolarised cross section is characterised by the differential cross section and three spin density matrix elements.

Chapter 2

The $g14$ Experiment

In this chapter, the data obtained from the $g14$ run period will be discussed. This includes an overview of the HDice target, and details such as run conditions, data skimming methods and corrections made to CLAS data.

2.1 The HDice Target

The target was designed such that it would be able to achieve high polarisation of both "free" protons (from *Hydrogen*) and neutrons (from *Deuterium*) with frozen spins ('ice').

The advantage of using HD as a polarised (bound) neutron target is manyfold. Firstly, the HD target material requires conditions (with respect to magnetic field and temperature) achievable in CLAS and it can maintain its polarisation for long periods under experimental conditions. Secondly, when compared to other bound neutron targets, such as ammonia and butanol (as in the FROST target at CLAS [8]), there is less background from unpolarised target material. Thirdly, it contains also a highly polarisable proton source.

In principle very high polarisations are achievable for this set-up; as high as 90% H polarisation and up to 60% D polarisation [9] [10]. The drawbacks for such a target are that the handling procedures are complex and, as was experienced during the $g14$ run, the risk of losing target polarisation is significant. Compounding this, while polarisation can quickly be lost, if no targets are waiting to replace a failed target, new targets take months to properly produce.

2.1.1 HD-ice Target Geometry

The cells used for the HDice target have dimensions of 15 $mm\phi \times 50$ mm; an exploded-view of a target cell is shown in Figure 2.1.

Figure 2.1: Photograph of a deconstructed HDice target, showing the cell, copper ring and aluminium wires [10].

The aluminium wires are used to mitigate any heat build up in the solid HD, these are inserted into holes in a copper ring. This copper ring is double-threaded such that it allows the cell to be transferred between dewers without violating the magnetic field or temperature conditions. The cell walls are made from ***P***oly***C***hloro***T***ri***F***luoro***E***thylene (PCTFE - C_2ClF_3), also referred to as $KelF$, which provides a clean cell with no background for H and D from ***N***uclear ***M***agnetic ***R***esonance (NMR) measurements. A more detailed schematic of a constructed HD target is shown in Figure 2.2.

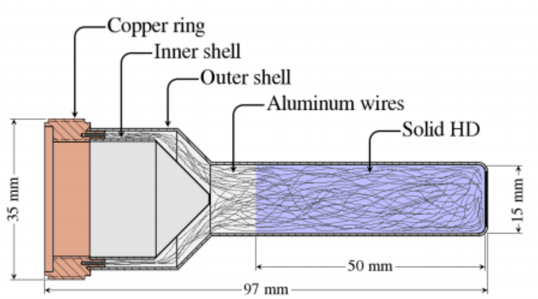

Figure 2.2: HD target schematic, indicating dimensions within the target[11].

The constituent materials in the target are broken down into their relative abundances in Table 2.1.

Material	Abundance (%)
HD	77
Al	16
$KelF$	7

Table 2.1: Target material abundances by mass.

2.1.2 Produced Targets

Only three targets were produced for use with production running during $g14$, although others were used for beam tests. The details of these targets are presented in Table 2.2.

Target Cell	Cell Name	$\rho(g/cm^2)$	ρ wrt $21a$	Beam Conditions Used
$21a$	*Silver*	0.028	1.0	Circularly polarised
$19b$	*Gold*	0.020	0.70	Circularly/linearly polarised
$22b$	*Last*	0.027	0.96	Linearly polarised

Table 2.2: Summary of the targets produced for the $g14$ run period and their characteristics.

2.2 $g14$ Run Overview

The $g14$ run period, also known as the HDice experiment, ran for seven months from November 2011 to May 2012. The dataset was subdivided into smaller sets based on conditions such as the target cell used, its polarisation and the polarisation direction. A breakdown of these periods are shown in Table 2.3.

Unfortunately during the run period several incidents occurred which led to accidental reduction of target polarisation. These occurred in both target $21a$ (periods labelled $Silver1/2/3/4/5$) and in target $19b$ ($Gold2$). At the end of

Period	Beam Energy (GeV)	e^- Beam pol (%)	Run Range	Date Range	Events (10^6)	Torus Current (A)	Target Pol. (%)
$Silver1$	2.281	$81.5 \pm 1.4 \pm 3.3$	68021 – 68092	01/12 – 06/12	830	+1920	$+25.6 \pm 0.7 \pm 1.5$
$Silver2$	2.281	$81.5 \pm 1.4 \pm 3.3$	68094 – 68176	06/12 – 11/12	1170	+1920	$+23.2 \pm 0.7 \pm 1.4$
$Silver3$	2.281	$76.2 \pm 1.4 \pm 3.1$	68188 – 68230	12/12 – 16/12	250	−1500	$+21.2 \pm 0.8 \pm 1.3$
$Silver4$	2.281	$88.8 \pm 1.5 \pm 3.6$	68232 – 68305	16/12 – 04/01	820	−1500	$-6.4 \pm 0.4 \pm 0.4$
$Silver5$	2.258	$88.8 \pm 1.5 \pm 3.6$	68335 – 68769	04/01 – 05/02	5210	−1500	$-5.9 \pm 0.2 \pm 0.4$
$Gold2$	2.542	$83.4 \pm 1.5 \pm 3.3$	69227 – 69364	10/04 – 18/04	2100	−1500	$+26.8 \pm 1.0 \pm 1.6$
$EmptyA$	3.356	$88.2 \pm 1.5 \pm 3.6$	68993 – 69037	08/03 – 11/03	660	−1500	0
$EmptyBb$	3.356	$88.2 \pm 1.5 \pm 3.6$	69038 – 69044	11/03 – 12/03	120	+1920	0

Table 2.3: Summary of the $g14$ run period. This shows each sub-period, including the beam, torus and target characteristics [12].

$Silver5b$ the target lost almost all polarisation; subsequently the $21a$ target was used in order to take data for an empty target. This is a target which contains no polarised material, only unpolarised HD. Note that for empty target data it is necessary to produce runs with both positive and negative torus setting, to account for any differing acceptance effects; these were labelled *emptyA* and *emptyB* for negative and positive torus settings respectively. Due to the unexpected drop in polarisation seen in $Silver5b$, another target had to be installed prematurely, before it was fully polarised and ready for data taking. Target $19b$ was substituted for the $21a$ target, giving a good set of runs with highly polarised HD.

2.2.1 Estimating Target Polarisations for Periods Silver 4 and 5

Some discrepancies were raised with initial results obtained from the $Silver4$ and 5 periods. This manifested in a drop in the magnitude of the $\mathbb{E}$ observable when compared to other periods. This indicated that the true polarisation values for $Silver4$ and 5 were smaller than originally calculated using NMR measurements. Members of the $g14$ group[1] studied this issue using the $\gamma n \to \pi^- p$ reaction, in order to see what the target polarisation would have had to be to produce the same $\mathbb{E}$ asymmetry in $\pi^- p$ as seen in the $Gold2$ period, assuming compatible and comparable beam helicities. The study indicated a disparity of the values given for the target polarisation using the NMR and what was seen for the target polarisation of the $Silver4$ and 5 periods.

Experimentally, at the start of the $Silver4$ period the target was rotated from spin $+Z$, parallel to the beam momentum, to $-Z$ anti-parallel to the beam momentum. During this process it was noted that there were some mechanical failures, although it is not believed that any of these issues should have caused significant polarisation loss and it is not known why there should be any disparity with the NMR measurement.

The result from the NMR was given as $\sim 25\%$ whereas the analysis method gave a target polarisation of only $\sim 6\%$. The true cause of this is unknown and still being considered within the group.

[1]Dao Ho and Peng Peng were responsible for providing this study to the group.

2.3 Organisation of the $g14$ Data

Data is collected from detectors into ***B**ank **O**bject **S**ystem* (BOS) files [13]. The dataset is then *cooked*, where it is converted into usable variables such as charge, momentum and particle beta. The cooking was done using the CLAS reconstruction and analysis package RECIS and was overseen by the $g14$ "chef", Franz Klein.

After the cooking was completed, each detector went though a detailed calibration procedure. These were to apply individual corrections to the data for each subsystem; ensuring consistency across all runs and indicating potential problems. Responsibility for these calibrations were split across the $g14$ group, indicated in Table 2.4.

Calibration	Responsible	Prerequisite
Tagger	Natalie Walford	None
Time-of-Flight	Haiyun Lu	Tagger
Start Counter	Jamie Fleming	Tagger
Drift Chamber	Dao Ho	Time-of-flight & Start Counter
Drift Chamber Alignment	Franz Klein	Drift Chamber
Electromagnetic Calorimeter	Irene Zonta	Time-of-flight & Start Counter

Table 2.4: Calibration responsibilities and prerequisites.

Once calibration is completed the datasets are cooked once again, allowing for the new calibration constants for all subsystems to be used. This iterative calibration-cooking cycle is continued until the calibration of the data is of a high standard and there are no misalignment artefacts in the data[2].

The files produced after cooking are in a compact ROOT ***D**ata **S**ummary **T**ape* (DST) format, which contains banks of the physical variables allowing for the reconstruction of events.

The analysis for this note was completed using an analysis framework based around the (`C++` based) object-orientated ROOT framework from CERN

[2]Detector calibrations are considered in the recent $g14$ analysis note for the channel $\pi^- p$ [14].

[15]. This framework is named ROOT ***B***ank ***E***vent ***E***xtraction ***R***outines (ROOTBEER), which allows the reading of DST files in a form which is independent of CLAS analysis programs and allowing analysis code to be made into executables [16].

2.4 Data Banks and Skimming

The information reconstructed for each event is stored in "banks", which can be considered as tables of information stored independently for each event. These banks are numerous and organised in various ways, such as by detector or by reconstruction method.

2.4.1 Banks

During the process of data reduction, banks can be kept or removed as required. From the complete list of banks retained from the skim[3] only a handful were used in the final analysis, although others were useful for diagnostic purposes. The main bank used in the analysis was the GPID bank [17].

The GPID bank contains particle information, as well as information from the time-of-flight scintillators, start counter and tagger. Initially during the selection the ***P***article ***ID***entification (PID) variable of this bank was used as some initial particle selection, though this is not a very robust method. The PID variable was mainly considered for some initial diagnostic tests and was later dropped in favour of a more robust method of selection.

The PID variable is defined as follows; the momentum is determined from the bending of the particles in the DC magnetic field. From this, values of the particle β are trialled using the PDG particle masses. The value of β is measured using time-of-flight information and the difference between these measured values and the trail values are minimised. This best suited identity is then assigned to the particle. This method has associated issues, particularly when particle corrections are not taken into account and particularly struggles to separate pions and kaons at high momenta.

[3]The full bank list is as follows: HEAD, TGBI, EPIC, CL01, ECHB, SCRC, STRE, TAGR, HBTR, HDPL, TBER, TDPL, MVRT, VERT, RGLK, PART, HBID, TBID, GPID, HEVT, EVNT, DCPB, TRPB, ECPB, SCPB, STPB, TGPB.

Other banks used in this analysis are outlined below:

- HEAD: Bank containing information about the run; primarily used to obtain the number of the current run.
- MVRT: Bank containing information about the event vertex.
- TBID: Bank containing information about time-based particle ID; using details from the time-of-flight, Cherenkov counter, electromagnetic calorimeter, start counter and large angle calorimeter.
- TAGR: Bank containing information from the photon tagger; primarily used for the selection of the event photon.

2.4.2 $K^+\Sigma^-$ Skim

The skim used in this analysis was an exclusive $K^+\Sigma^-$ skim. The particle identification for charged tracks were taken from the EVNT or PART banks of CLAS, and selecting particle β using momentum p (in GeV): $\beta_{min} < \beta < \beta_{max}$. The full requirements of the $K^+\Sigma^-$ skim were as follows:

- Pions:

$$\begin{aligned} \beta_{min} &= \frac{p}{\sqrt{p^2 + 0.3^2}} - 0.03, \\ \beta_{max} &= \frac{p}{\sqrt{p^2 + 0.05^2}} + 0.03. \end{aligned} \tag{2.1}$$

- Kaons:

$$\begin{aligned} \beta_{min} &= \frac{p}{\sqrt{p^2 + 0.6^2}} - 0.05, \\ \beta_{max} &= \frac{p}{\sqrt{p^2 + 0.4^2}} + 0.05. \end{aligned} \tag{2.2}$$

- Protons:

$$\begin{aligned} \beta_{min} &= \frac{p}{\sqrt{p^2 + 1.1^2}} - 0.06, \\ \beta_{max} &= \frac{p}{\sqrt{p^2 + 0.8^2}} + 0.06. \end{aligned} \tag{2.3}$$

- Z vertex distance for a $\pi^+\pi^-$ pair must be $< 2.0\ cm$.
- No particle identification cut for neutral particles.
- Event particles: $K^+ = 1$, $\pi^- = 1$, $\pi^+ = 0$, $p = 0$, $neutrals < 3$.

2.4.3 Selection of Experimental Data to be Analysed

Some individual files and runs were removed due to poor quality data or corrupted files. This included runs which were not production quality, either due to the stability of the beam delivered to the Hall or simply that these runs were designed for some diagnostic reason. The removal of these data was primarily carried out during cooking and calibration phases.

2.5 Applied Corrections to Data

Although the data had undergone a cycle of calibration and cooking, other corrections were still required. These are to account for various systematic effects of detectors and the energy loss of particles during detection.

2.5.1 Kinematic Fitting

A measured quantity, the particle 4-vector, must fulfil certain kinematic constraints, such as the conservation of momentum. Since these measured quantities have some associated uncertainty, the constraints are not perfectly satisfied. The constraint boundaries can then be used to slightly change the measured values, within the parameters of their uncertainties, without breaking conservation.

The goal of kinematic fitting is to have an event-by-event least squares fitting to ensure the measured values fulfil the constraints. The software used for this iterative procedure was developed at ***C***arnegie ***M***ellon ***U***niversity (CMU) [18] [19].

Least squares fitting, utilises the minimisation of the sum of the squares of the data offsets from some fit, commonly referred to as *residuals*. If we consider the sum of the residuals for a set of n points for some function f:

$$R^2 = \sum_i [y_i - f(x_i, a_1, a_2, ..., a_n)]^2, \tag{2.4}$$

where y_i is the measured value for each of the n events.

The sum of the squares is used so we can exploit the fact that the residuals can be treated as a continuous differentiable quantity. This does mean however that outlying points are given disproportionately large weighting due to the construction of R^2. The condition to minimise R^2 for some dataset $i = 1, ..., n$ is:

$$\frac{\partial(R^2)}{\partial a_i} = 0. \tag{2.5}$$

If some measurable quantity is considered, we can write:

$$\overrightarrow{\eta} = \overrightarrow{y} + \overrightarrow{\epsilon}, \tag{2.6}$$

where $\overrightarrow{y}$ are the estimator variables as given by a fit and $\overrightarrow{\epsilon}$ are the set of deviations needed to shift the observed values of $\overrightarrow{\eta}$ to satisfy the constraints. Ideally these shifts in $\overrightarrow{\eta}$ should have a Gaussian distribution around zero. The shift distributions are checked at each iteration, which is done by using pull distributions in order to measure the relative difference of the values and their uncertainties, reminiscent of the residuals. The pulls are defined as:

$$z = \frac{\eta_{it} - y_{it}}{\sigma^2_{\eta_{it}} - \sigma^2_{y_{it}}}. \tag{2.7}$$

The iterations continue until they converge on an ideal Gaussian distribution, $\mu = 0; \sigma^2 = 1$.

2.5.2 CLAS tracking parameters

Three separate coordinate systems are used in CLAS. These are the tracking system, lab system and sector system. It is important to consider the transition from the tracking system to the lab system within CLAS for use with the correction methods. The track system defines x along the beam line; y through the sector centre and z along the average magnetic field direction. Whilst the lab system defines the x through the centre of sector 1; y is vertically upwards and z is along the direction of the beam line. These systems are shown in Figure 2.3.

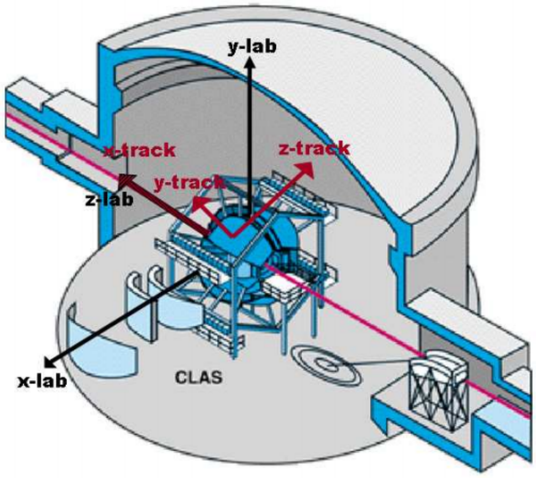

Figure 2.3: Diagram outlining the two coordinate systems used in CLAS [20].

The track system can be related to the lab system as follows:

$$\begin{pmatrix} x_{track} \\ y_{track} \\ z_{track} \end{pmatrix} = \begin{pmatrix} z_{lab} \\ \cos(\alpha)x_{lab} + \sin(\alpha)y_{lab} \\ -\sin(\alpha)x_{lab} + \cos(\alpha)y_{lab} \end{pmatrix}, \tag{2.8}$$

where $\alpha = \frac{\pi}{3}(N_{sector} - 1)$.

The momenta of the tracks are considered in terms of the ratio of momentum and charge, $q/|p|$, the dipolar angle relative to the sector plane, λ and the angle in the sector plane relative to the x_{track} axis, ϕ [21]:

$$\begin{pmatrix} p_{x_{lab}} \\ p_{y_{lab}} \\ p_{z_{lab}} \end{pmatrix} = \begin{pmatrix} p(\cos(\lambda)\sin(\phi)\cos(\alpha) - \sin(\lambda)\sin(\alpha)) \\ p(\cos(\lambda)\sin(\phi)\sin(\alpha) + \sin(\lambda)\cos(\alpha)) \\ p\cos(\lambda)\cos(\phi) \end{pmatrix}. \tag{2.9}$$

2.5.3 Energy Loss Correction

CLAS uses the curvature of charged particle tracks in the DC to determine particle momentum. However, the code used during the reconstruction does not take into account the energy loss due to material the particle encounters before it reaches the drift chambers. This becomes critically important for photon runs as the start counter is placed surrounding the target, removing yet more energy. This is particularly important for low momentum particles which lose their energy easily. The Eloss software[4] attempts to correct for these energy losses.

From the event vertex to the drift chambers, the particle must pass through a significant amount of material such as the start counter paddles, beam pipe and target cell material/wall. The software looks at the path of the particle to identify which materials it has passed through. The thicknesses of the various materials are calculated and the software attempts to correct the 4-vector for the energy which would be lost in the material. Although this has been done for many previous experiments at CLAS, the software target was updated specifically for the HDice target geometry and material [22].

2.5.4 Momentum Correction

The goal of using a correction to particle momentum is to improve the resolution of the data; for the $g14$ period this was done using kinematic fitting. Several factors lead to the need for momentum corrections after the calibration phase. The CLAS reconstruction momentum is taken from DC information; which means that any errors in the alignment of the DC or inaccuracies in the field map will be propagated into the reconstructed momenta. The reaction $\gamma p \to p\pi^+\pi^-$ was studied to obtain the corrections. The Eloss correction was applied to the final state particles before the event was kinematically fitted.

The correction works in terms of considering three hypotheses; wherein one of the final state particles is considered "missing":

- $\gamma p \to (p)_{missing}\pi^+\pi^-$,
- $\gamma p \to p(\pi^+)_{missing}\pi^-$,
- $\gamma p \to p\pi^+(\pi^-)_{missing}$.

The corrections applied are:

$$\begin{aligned} \Delta p_x &= p_x^{kfit} - p_x^{meas}, \\ \Delta\lambda_x &= \lambda_x^{kfit} - \lambda_x^{meas}, \\ \Delta\phi_x &= \phi_x^{kfit} - \phi_x^{meas}, \end{aligned} \tag{2.10}$$

[4]The Eloss software was written and updated for the $g14$ run by Eugene Pasyuk of Jefferson Lab.

where p is the magnitude of the momentum vector; λ is the dipolar angle relative to the sectors (x, y) for the track and ϕ is the angle of the x_{track} relative to the (x, y) plane.

2.5.5 Tagger Correction

An additional correction must be added to the tagger after calibration, as alignment issues lead to photon energies being reconstructed with some offset [21]. This misalignment comes from the weight of the paddles over time moving them from their original alignment, leading to inaccurate values given by certain tagger channels. Note that these corrections will also differ according to the energy of the electron beam and so must be considered for each beam setting. The reaction $\gamma p \to p\pi^+\pi^-$ was again studied after the Eloss correction was applied. The events were then kinematically fitted, and events with a ***C***onfidence ***L***evel (CL) greater than 10% were used to determine the correction. The correction for each beam energy, E_{beam} is:

$$\Delta E_{tag} = \frac{E_\gamma^{kfit} - E_\gamma^{meas}}{E_{beam}}, \tag{2.11}$$

where E_γ^{kfit} is the photon energy value from the kinematic fitting and E_γ^{meas} is the photon energy from the tagger system. The correction was then used for the associated beam period and then for each tagger paddle on an event-by-event basis.

2.5.6 Neutron Vertex Correction

If the neutron was able to be reliably detected and the complete final state $K^+\pi^-n$ identified, more corrections would need to be made. This consideration is not required for this work but would become important during any higher statistics experiments.

Neutrons are detected finally in the CLAS EC. Due to the large interaction length for the neutron in the EC, it is difficult to accurately pinpoint the hit coordinates. Any offsets in the interaction vertex within the EC can be considered using a careful study of the channel $\gamma D \to \pi^+\pi^- pn$. This takes advantage of a common production vertex, therefore giving a reliable neutron vertex in the target.

When considering the $K^+\Sigma^-$ channel rather than $\pi^+\pi^-pn$, there is a subtlety. The neutron that we would consider has a displaced vertex as the decay length of the Σ^- is $\sim 4.43cm$. Although generally when CLAS assigns vertex it chooses the vertex of the fastest particle in the event (e.g. a fast $\pi^\pm$). This is usually a good approximation when the neutron comes from the primary interaction vertex, but something more subtle would have to be considered and studied to have some idea what influence this vertex choice would have in the data.

These neutron corrections were implemented in the previous measurements in CLAS [23] [24].

Chapter 3

$\gamma N \to K^+\Sigma^-$ Event Selection

This chapter details the use of the $g14$ period dataset to reconstruct and identify the reaction yield of:

$$\gamma n \to K^+\Sigma^- \to K^+\pi^- n. \tag{3.1}$$

3.1 Outline

The $g14$ experiment is one of the first measurements of the photoproduction of mesons from a polarised neutron target and will be instrumental in the world programme to better establish the excitation spectrum of the nucleon. Expected rates are given in [10] as ratios to other decay channels. It is expected that the cross section of $K^+\Sigma^-$ is one fifth of the cross section of $K^0\Lambda$. An estimate of $K^0\Lambda$ was made by JLab of 10^4 events for the experimental period, giving 2000 expected events for $K^+\Sigma^-$. It has since been thought that this initial ratio of $1:5$ is a large underestimate, from a relative comparison of other run periods. Previous experiments at JLab have shown that this ratio may be much closer to $1:1$[1]. Since this was clearly uncertain, a rough event study was undertaken before the full analysis was initiated. This study confirmed that enough events were present to warrant a complete analysis.

This channel is particularly challenging for several reasons other than the low relative cross section. Firstly, power of the polarisation observable measurement is correlated with the available target polarisation, which was predicted to be able

[1]From private correspondence with Franz Klein.

to have values of 75% for H and 40% for D. In practice typical values of 15-25% were obtained for both H and D. Secondly, CLAS itself was not designed as a neutral particle detector, with a neutron efficiency of only 5-7% [10], so with a final state neutron this becomes problematic. Misidentification is also a concern, specifically the false ID of K^+ as π^+. Finally, because the target neutron is bound inside deuterium, there will be Fermi motion of the nucleon.

3.2 Event Selection

After the data is skimmed, as outlined in Section 2.4.2, the files were transferred to a storage space at the University of Edinburgh. These individual run files were arranged and merged into periods as outlined in Table 2.3. Once this was complete the event selection procedure could begin. Each stage of selection was carefully monitored in terms of statistics of events removed, in order to ensure sensible reductions.

3.2.1 Coarse Data Reduction

The skimmed CLAS data contains the events of interest, as well as other reaction channels not studied in this analysis note. Initial coarse selection cuts were applied to the skimmed data to further reduced the data sample.

The multiplicity of an event is the number of particles successfully identified in the final state. Of course, ideally for this analysis all three final state particles would be identified, $K^+\pi^-n$. However, due to the restrictions of CLAS to identify neutral particles this is not always possible. This means that the two particles, non-exclusive, final state, $K^+\pi^-$, where the neutron has not been detected is the primary consideration. For this case the (undetected) neutron can be reconstructed from the missing mass : $\gamma n \to K^+\pi^-X$. M_x can be evaluated on an event-by-event basis to select neutron candidates from the reaction yield.

By considering the hit multiplicity in CLAS and selecting events with two and three particle final states we can reduce the data to be processed. Furthermore, we can improve the quality of the data selected by requiring that events also have a valid hit in the tagger. The distribution of the selected final states are shown in Figure 3.1:

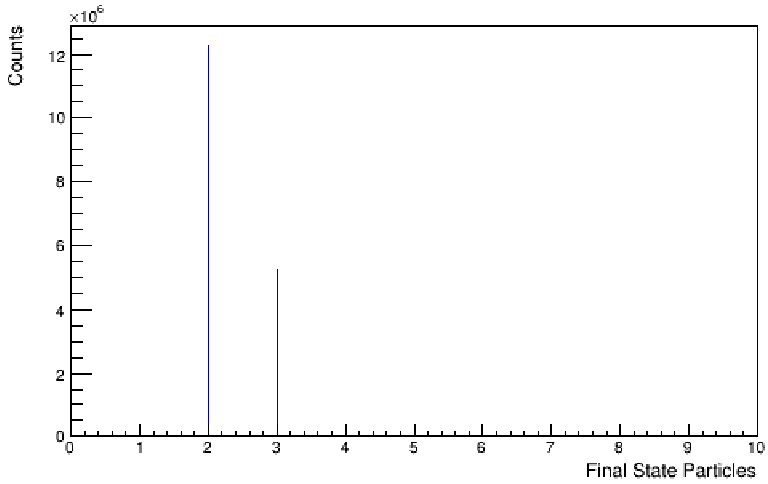

Figure 3.1: Event multiplicity selection.

- 2 or 3 final state particles ***and*** a corresponding hit in the tagger.

Events which do not meet this requirement are removed from the analysis.

3.2.2 Detector Hits

Some simple detector requirements can be used to attempt to identify "good" events. That is to say, that events are required to have a certain amount of information associated with it. The requirements are as follows:

- All events require at least one corresponding hit in the focal plane detector.
- All charged particles require a valid event in the drift chamber and the time-of-flight paddles.
- All charged particles require a charge of only one unit.
- All neutral particles require a valid hit in the electromagnetic calorimeter and no hit in the DC.

Events which do not meet these requirements are removed from the analysis.

3.2.3 Particle Mass^2 Windows

The particle mass is calculated using the momentum from the track curvature and the particle velocity:

$$M_{calc}^2 = \frac{p^2(1-\beta^2)}{\beta^2}. \quad (3.2)$$

Events of interest in the analysis were kept using a selection on the mass of the particles of interest (K^+ or π^-). A typical mass squared spectra for positive particles in CLAS is shown in 3.2. The particle selection cuts were kept wide for this initial stage, as refinements to the energy and momentum reconstruction of the particles can be carried out at a later stage, as described in Section 2.5.

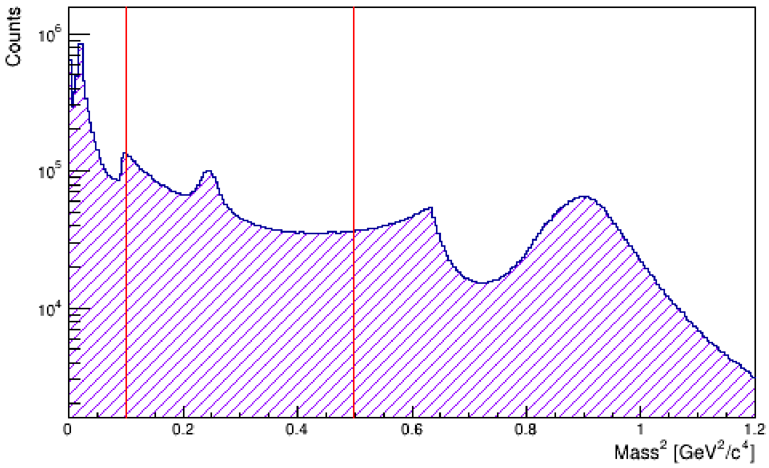

Figure 3.2: Histogram showing the mass squared distribution of positive particles after skimming (*log scale*). The selection windows are shown in red.

If we consider Figure 3.2, the well defined peaks of the pion (π^+), kaon (K^+) and proton (p) can clearly be seen. For the channel of interest, the final state particles are initially selected using charge in tandem with the chosen M^2 windows. The following M^2 windows were chosen:

- Kaon : $0.1 < M_{K^+}^2 < 0.49\ GeV^2/c^4$ (PDG 0.244 GeV^2/c^4).
- Pion : $0.0 < M_{\pi^-}^2 < 0.1\ GeV^2/c^4$ (PDG 0.0196 GeV^2/c^4).

Particles which do not meet these mass requirements are removed from the analysis. Figure 3.3 shows the mass squared distribution for all (positive, negative and uncharged) particles. The distribution shows similar general features to Figure 3.2 but there is a large neutron spike as seen at $\sim 0.88\ GeV^2/c^4$. The identification of neutrons is discussed in 3.2.4.

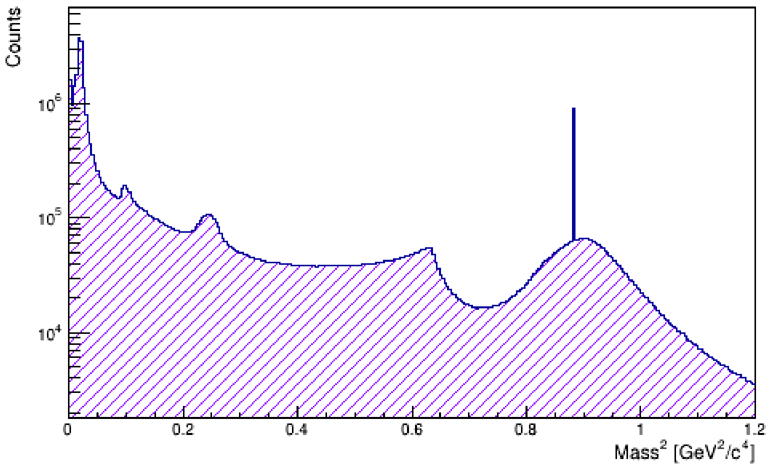

Figure 3.3: Histogram showing the mass squared distribution of all particles after skimming (*log scale*).

Once the mass squared windows are applied, these candidates particles are assigned a preliminary particle identification. Further cuts improve the quality of this identification and remove the background which is present.

3.2.4 Neutron Selection

Neutral particles in CLAS are assigned a nominal value ($0.939\ GeV/c^2$), therefore neutrons and photons must be separated. This separation is achieved using the particle β; the distribution for neutral particle β is shown in Figure 3.4.

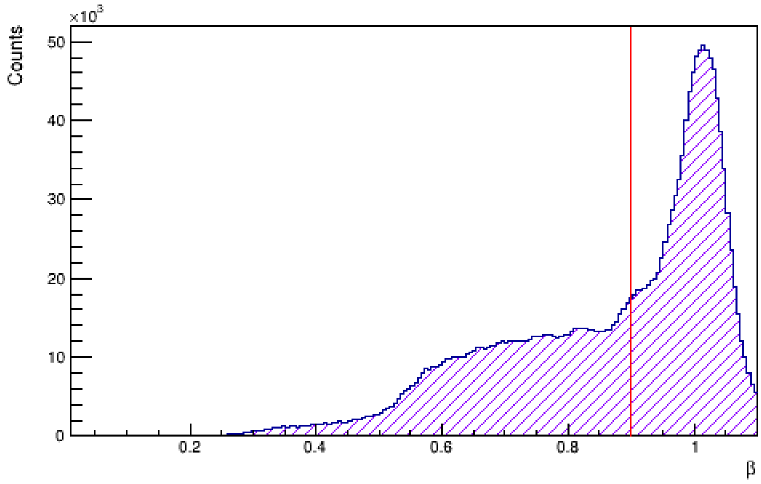

Figure 3.4: β distribution for neutral candidates. The selection cut is shown in red, with neutrons falling on the left and photons on the right.

The photon peak can be clearly seen centred around $\beta = 1$, with neutron populating the lower β regions. In order to decide where the cut should be placed to differentiate neutrons and photons, the peak was fitted and the width, σ, extracted. To eliminate the photons from the sample, a 3σ wide exclusion window was applied to the data. From the extracted σ this corresponded to:

- Neutrons $\beta_n < 0.9$.

Particles which do not meet this requirement in β are removed from the analysis.

3.2.5 Topology

Following the initial particle identification, a cut on the channel topology for the channel of interest was employed. This cut is dependent on the multiplicity of the final state:

- If 2 final state particles; these must have the identities of $K^+\pi^-$.
- if 3 final state particles; these must have the identities of $K^+\pi^-n$.

Events which do not meet these requirements are removed from the analysis.

3.2.6 Momentum vs $\Delta\beta$

Further refinements to the particle ID are carried out by utilising the correlation between the independently measured momentum (from the DC) and the measured time-of-flight (from the SC). The momentum vs β distribution for positive and negative particles is shown in Figure 3.5. The proton and pion bands are clearly seen in red, while the kaons can be made out in between. The other bandings, having a more horizontal locus, can be attributed to misidentified particles. The shadows in the bands (i.e. a mirror band occurring at a different β) are attributed to events where the photon was taken to be from the wrong beam bucket and as the time-of-flight was calculated by using an incorrect start time. The error in the momentum from the track curvature is of the order of $\sim 1\%$, while in β it is up to $\sim 5\%$ as the uncertainty comes from the time-of-flight and path length [25].

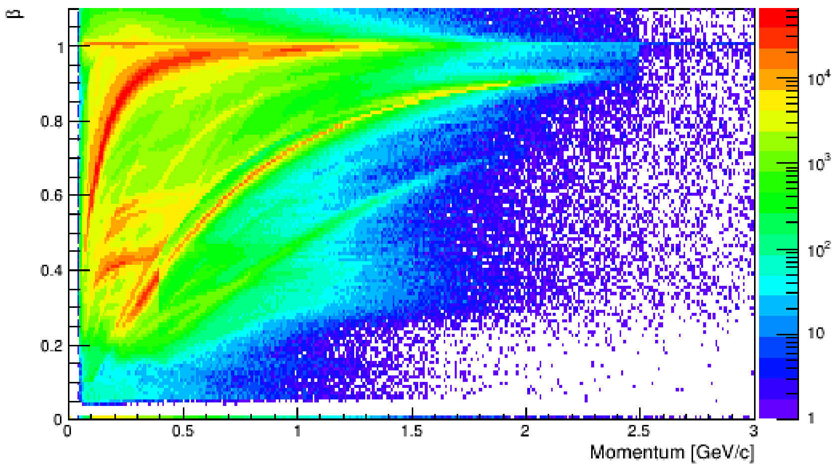

Figure 3.5: Momentum vs β distribution for positive and negative particles (*log scale*).

Figure 3.5 shows that at higher momenta the kaon and pion candidates begin to converge, particularly at $> 1.5\ GeV/c$. At these higher momenta their separation becomes difficult due to the worsening β resolution and the proximity of their loci.

To allow more simple particle ID regions to be identified, it is useful to present the data as the difference between the calculated and measured β, referred to as $\Delta\beta$.

The calculated β is obtained using the measured momentum and the PDG mass of the particle. By using the PDG mass, we assume that the particle ID is correct and the mass is absolute. $\Delta\beta$ is calculated as follows:

$$\beta_{meas} = \frac{path_{DC}}{ct_{ToF}}, \tag{3.3}$$

$$\beta_{calc} = \sqrt{\frac{p^2}{m_{PDG}^2 + p^2}}, \tag{3.4}$$

$$\Delta\beta = \beta_{meas} - \beta_{calc}. \tag{3.5}$$

$\Delta\beta$ is calculated separately for the kaon and pion candidates, with the distributions plotted against momenta, as shown in Figure 3.6.

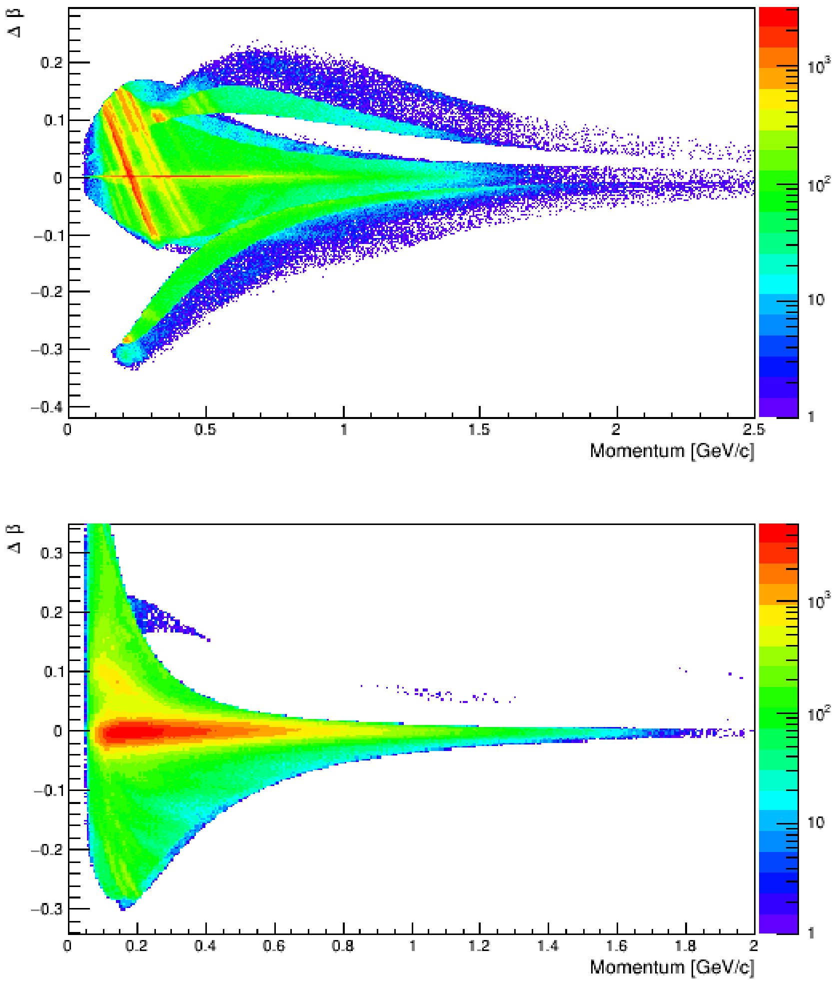

Figure 3.6: Momentum vs $\Delta\beta$ distribution (*log scale*) for K^+ candidates (upper) and for π^- candidates (lower).

If we consider the kaon plot, we can see that misidentification of π^+ at this stage of the analysis is a large problem. Also present, are events which correspond to photons from adjacent beam buckets, since no timing selections have yet been implemented. We can remove the obvious misidentified pions, the curved band, by using $2D$ momentum dependent $\Delta\beta$ cuts, this is kept deliberately wide as its only purpose is for misID removal.

For the π^- candidates the selection is already relatively clean and we use a simple 3σ cut in $\Delta\beta$.

After the boundaries of the cuts were decided they were applied to the sample, the result of which can be seen in Figure 3.7.

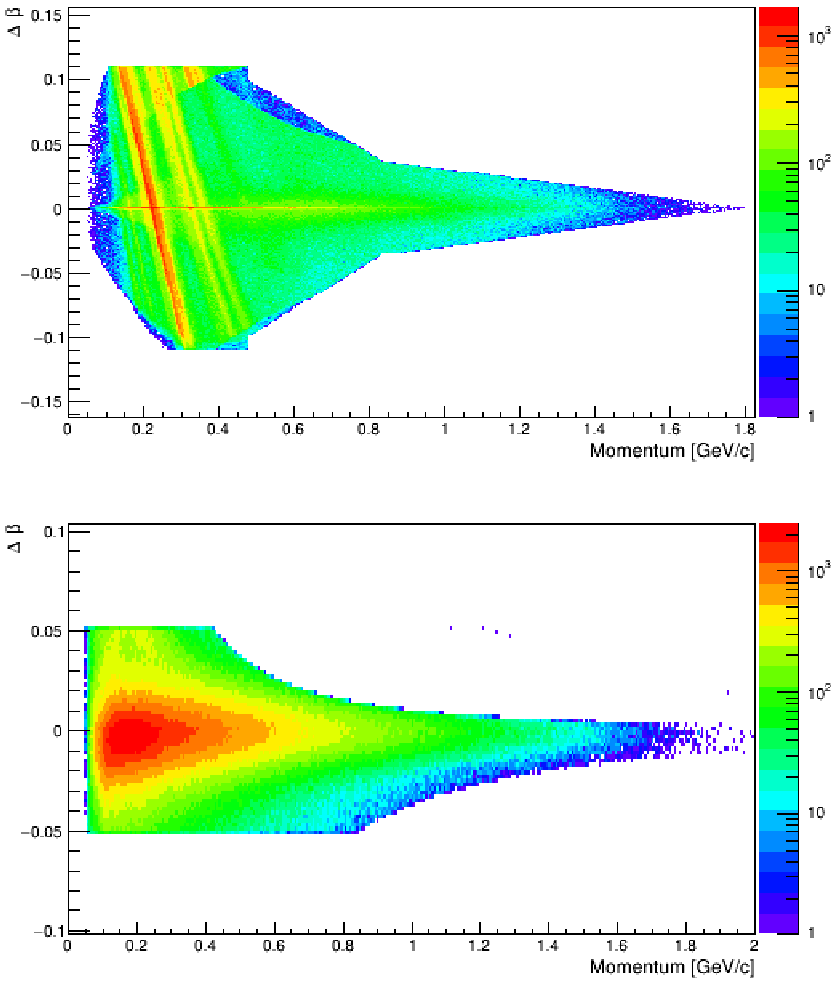

Figure 3.7: Momentum vs $\Delta\beta$ distribution (*log scale*) for K^+ candidates (upper) and π^- candidates (lower) after cuts in $2D$.

Particles which do not meet these requirements in $\Delta\beta$ and momenta are removed from the analysis.

3.2.7 Candidate Photons and Tagger ID

Removing "accidental events" is used to clean up the timing spectra before more formal timing cuts are introduced. Key variables used for this are NGRF and

TAGRID from the GPID bank. NGRF stores the number of candidate photons associated with an event, while TARGID stores an indexing to the TAGR bank indicating which candidate photon corresponds to a particle. The requirements introduced were:

- Number of candidate photons in same RF bucket, must be 1 for K^+ and π^- candidates.
- The tagger ID of the event must be the same for both the K^+ and π^-, showing they came from the same photon.

Events which do not meet these requirements are removed from the analysis.

3.2.8 Photon Identification

An important step in selection is to clarify the photon corresponding to an event. In order to do this, it must be shown that the timing from the tagger and ToF are consistent i.e. their difference is in the form of a Gaussian centred around zero. The tagger and the photon flight time are used to calculate the arrival time of the photon at the vertex, t_γ. The ToF and tracking information are used to calculate the vertex time from CLAS, t_v. The difference between these quantities should be minimised in order to identify the photon which most accurately represents the event.

The CLAS time-of-flight vertex time is calculated as:

$$\begin{aligned} t_v &= t_{SC} - t_{est}, \\ t_v &= t_{SC} - \frac{l}{c\beta}, \end{aligned} \tag{3.6}$$

where t_{SC} is the time-of-flight with respect to the global start time, measured by the scintillation counters (SC) and t_{est} is the estimated time-of-flight, obtained by using the length of the particle track from the vertex to the SC, l.

The photon time is calculated from the time of the photon to arrive at the target centre, t_{centre}, and the time for the photon to propagate from the target centre to the interaction vertex, t_{prop}:

$$t_\gamma = t_{centre} + t_{prop}. \tag{3.7}$$

The propagation time can be expanded:

$$t_{prop} = \frac{z_{vert} + d_{targ}}{c}, \tag{3.8}$$

where z is the coordinate of the event vertex on the beam axis and d_{targ} is the offset of the centre of the target on the z-axis[2]. This then gives:

$$t_{\gamma} = t_{centre} + \frac{z_{vert} + z_{targ}}{c}. \tag{3.9}$$

Some offset in the x and y directions will also be present due to the spot size of the beam (of order cm) but it should be noted that these will be comparable to the vertex resolution.

The photon coincidence time can then be calculated using Equation 3.6 and 3.9:

$$\Delta t = t_{\gamma} - t_{v}. \tag{3.10}$$

This is shown in Figure 3.8 for both kaons and pions. This plot also gives some indication of how well the time-of-flight and tagger were calibrated, as the times should be the distributed around zero; in this respect, this plot is a useful diagnostic aid during iterations of calibration.

We see a clear structure oscillating at a characteristic 2 ns; the structure is a symptom of the beam timing, indicating these are photons from other beam buckets taken in as a random correlation between a particle and the event trigger.

[2]In the $g14$ run period, the offset for the HDice target was -7.5 cm.

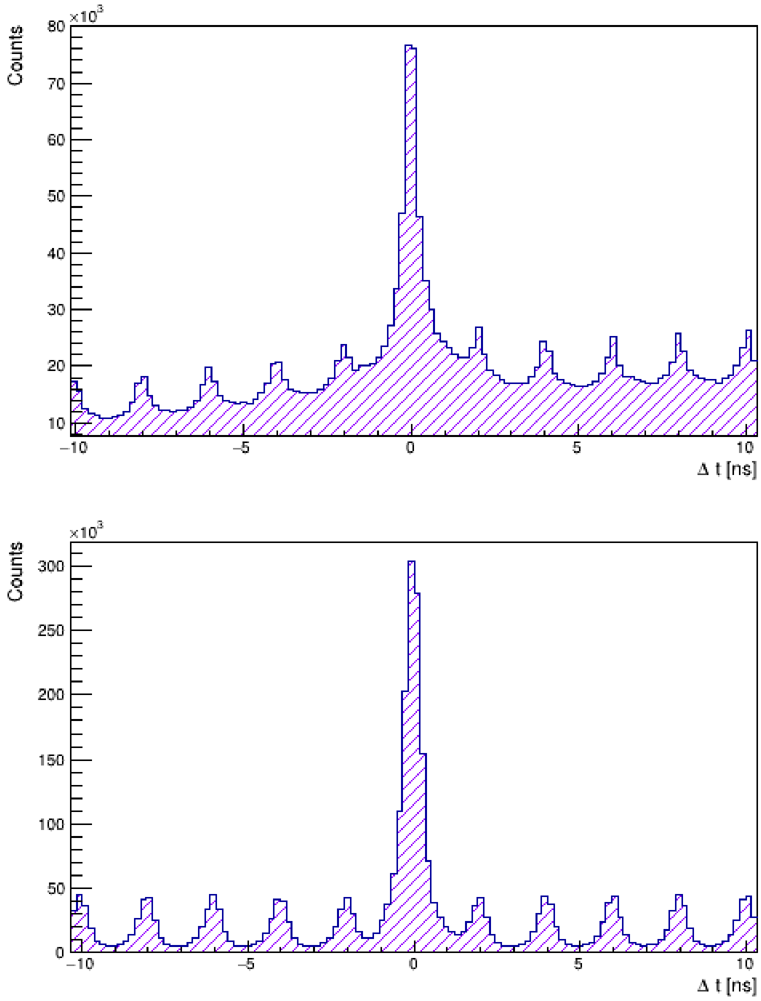

Figure 3.8: K^+ (upper) and π^- (lower) timing difference between the start counter and time-of-flight scintillators.

There is a clear background present in the kaon distribution, which is partially derived from the dependence of the vertex time on the momentum but the underlying background gives a much clearer indication that there are many misidentified pions in the sample. From these plots, it is clear the pions would give a cleaner timing selection due to the smaller background. The main consideration in doing this is, if we use this do we still select the same the best photon? A study addressing this was done and this method actually selects the same photon $\sim 99\%$ of the time.

For many events there will be more than one photon registered in the tagger.

It is important to consider which of these is the *best* photon for the event. This is done by minimising the timing difference between the vertex and the photon time. As well as misidentification, the kaons are influenced by pions which come from hyperon decays. This occurs because the hyperon can travel some distance before decaying, giving a displaced vertex for these pions. It is thought that this is the cause for the asymmetric kaon timing spectrum seen.

The best photon for both the kaon and pion candidates are shown in Figure 3.9.

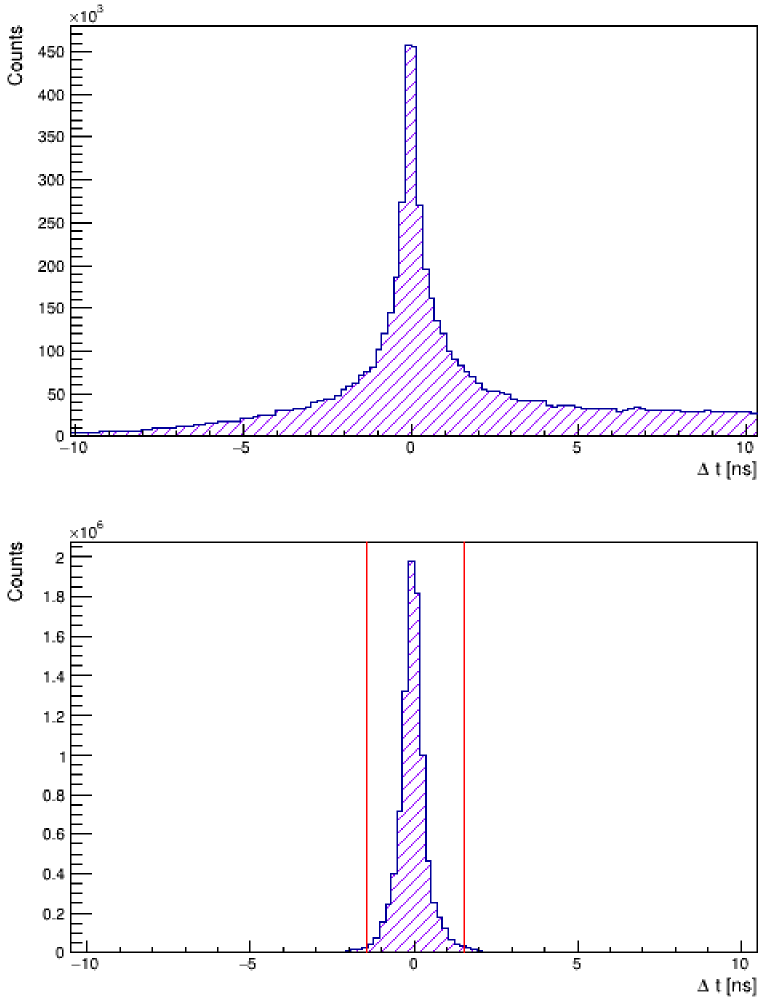

Figure 3.9: K^+ (upper) and π^- (lower) timing difference using the selected *best photon*. The selection cut is shown in red.

Once the best photon is chosen all external beam bucket structure is removed, although in the case of the kaon other candidates from outside the main peak can still be seen. Because of this, the time correlation for the event was taken from the pion alone.

The pion peak was fitted with a Gaussian and σ extracted; a 3σ selection was introduced to eliminate the background within the tails of the distribution. These backgrounds are generally from random hits which are correlated to an event but which do not correspond to the triggered event in CLAS. These events are removed by requiring that only a single photon hit is associated with the central beam bucket.

- $|\Delta t_{\pi^-}| < 1.5\ ns$.

Events which do not meet this timing requirement are removed from the analysis.

3.2.9 Data Corrections

At this stage in the analysis, tagger, momentum and Eloss corrections are applied to the data. These corrections were outlined in Section 2.5.

3.2.10 Corrected $\Delta\beta$ Selection

After the corrections to the data were complete, another $\Delta\beta$ selection could be done. The $\Delta\beta$ distributions after the data corrections are shown in Figure 3.10. These plots use the newly corrected β to construct this $\Delta\beta$.

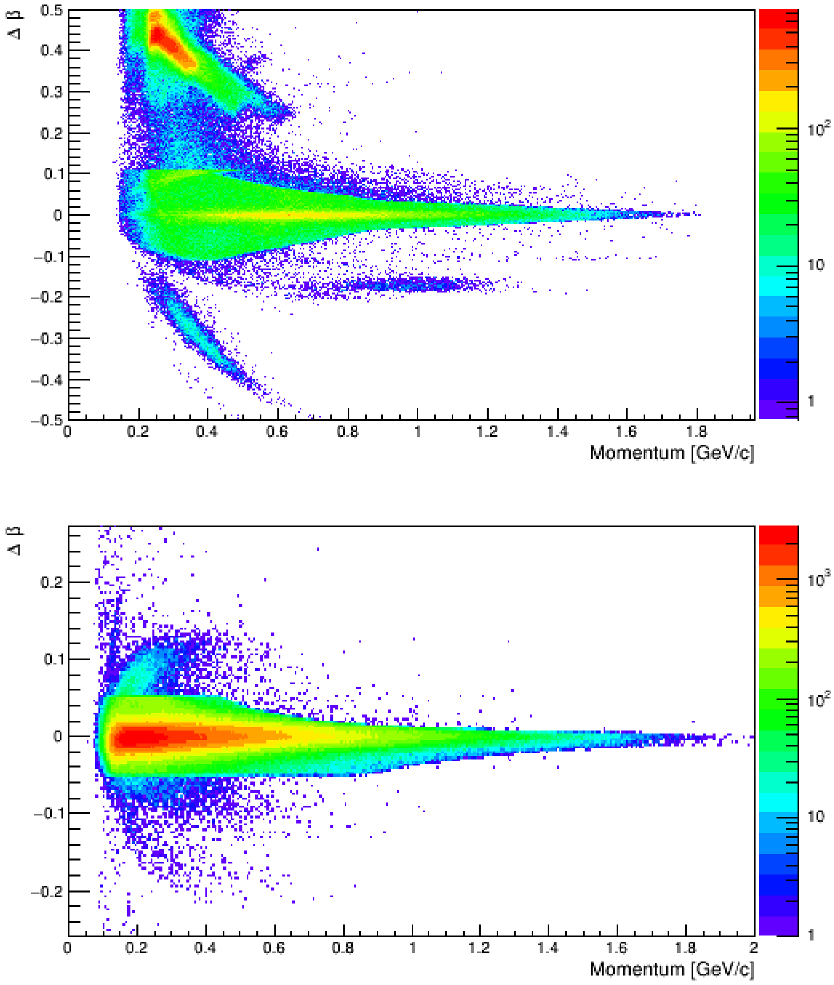

Figure 3.10: Momentum vs $\Delta\beta$ distribution (*log scale*) for K^+ (upper) and π^- (lower) after data corrections.

For the case of the K^+, the background of misidentified events has been strongly suppressed. Though pions can be seen in the curving loci coming from above, leave some residual signal in the K^+ selection region at high momenta. This means that even a subtle use of momentum dependent cuts will not sufficiently remove the background. Due to this fact a simple linear cut was used, as a more complex and sophisticated cut would not yield any great benefits. After a Gaussian fit, 3σ cuts were used on the main peaks, allowing the outlying misidentified particles to be removed. Note that in Figure 3.11 there is still background present, particularly at higher momenta, which is considered in forthcoming sections.

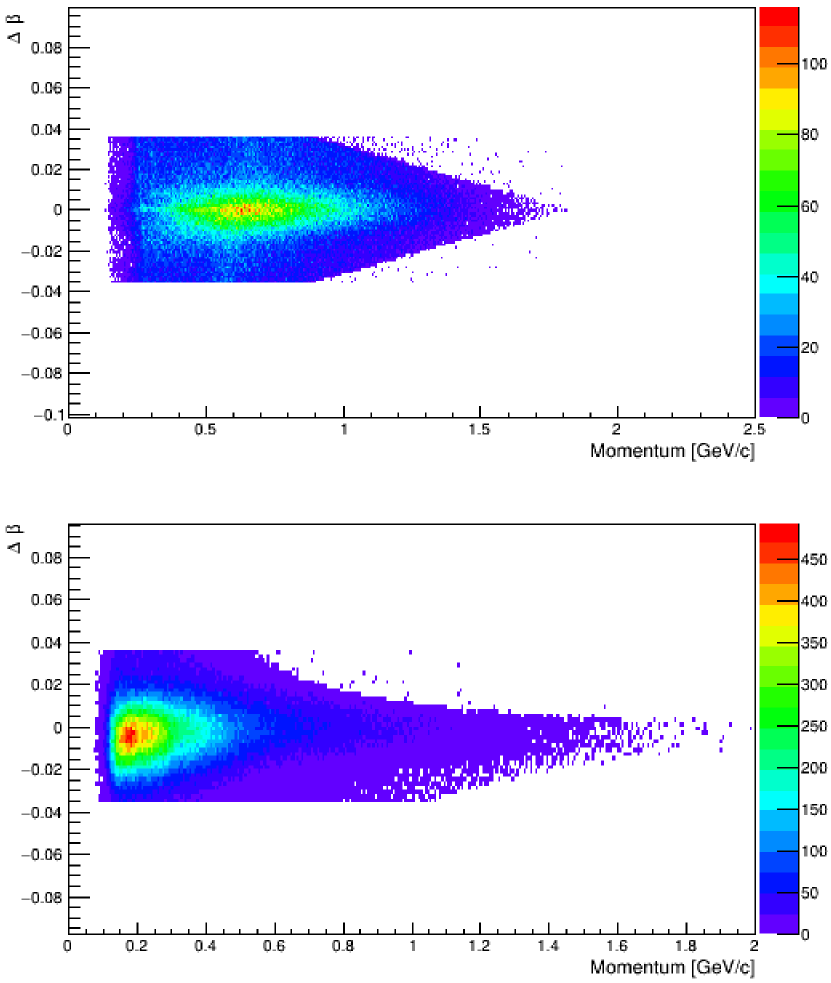

Figure 3.11: Momentum vs $\Delta\beta_{corrected}$ distribution (*log scale*) for K^+ (upper) and π^- (lower) after a further selection cut.

- $|\Delta\beta_{K^+\pi^-}| < 0.036$.

Events which do not meet these requirements in $\Delta\beta$ are removed from the analysis.

3.2.11 Reaction 4-Vectors

Considering the 4-vectors of the particles involved[3], we can represent the $K^+\Sigma^-$ reaction as:

$$\underline{\underline{\gamma}} + \underline{\underline{n}} = \underline{\underline{K}}^+ + \underline{\underline{\Sigma}}^-, \tag{3.11}$$

which due to 4-momentum conservation is equivalent to:

$$\underline{\underline{\gamma}} + \underline{\underline{n}} = \underline{\underline{K}}^+ + \underline{\underline{\pi}}^- + \underline{\underline{n}}. \tag{3.12}$$

However since we have difficulty detecting the neutron, the Σ^- must be reconstructed from the missing mass of the kaon, rather than the invariant mass of the $\pi^- n$ system, leading to:

$$\begin{aligned} \underline{\underline{\Sigma}}^- &= \underline{\underline{\gamma}} + \underline{\underline{n}} - \underline{\underline{K}}^+, \\ MM(K^+) &= \underline{\underline{\gamma}} + \underline{\underline{n}} - \underline{\underline{K}}^+. \end{aligned} \tag{3.13}$$

This allows for the reconstruction of the Σ^-. Similarly, the neutron may be reconstructed using K^+ and π^-:

$$\begin{aligned} \underline{\underline{n}}_{recon} &= \underline{\underline{\gamma}} + \underline{\underline{n}} - \underline{\underline{K}}^+ - \underline{\underline{\pi}}^-, \\ MM(K^+\pi^-) &= \underline{\underline{\gamma}} + \underline{\underline{n}} - \underline{\underline{K}}^+ - \underline{\underline{\pi}}^-. \end{aligned} \tag{3.14}$$

3.2.12 Misidentification of Particles

A common problem with all kaon analyses in CLAS is the ***misID***entification (misID) of pions as kaons. Although initially we established a wide M_K^2 window, there is still contamination from pions - and to a lesser extent protons. The backgrounds can be thought of in two categories:

- background correlated with the Σ^-.
- background uncorrelated with the Σ^-.

[3] Where we use the notation $\underline{\underline{X}}$ to denote the 4-vector of particle X.

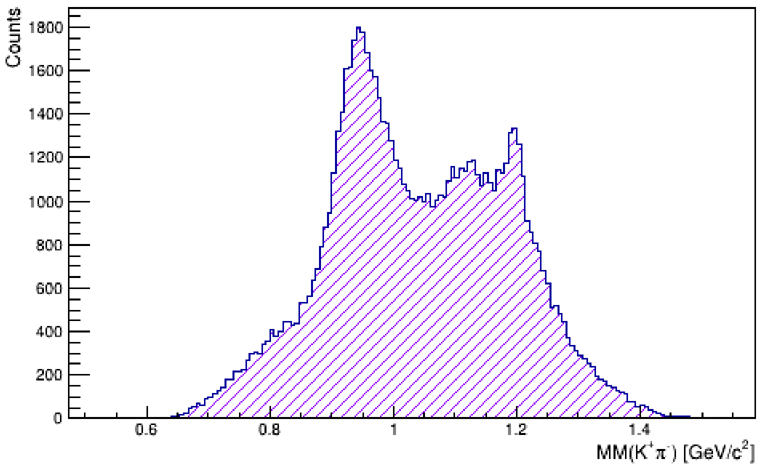

Figure 3.12: Correlated background seen in the neutron mass spectrum, reconstructed using the missing mass method.

The mass of the neutron, as reconstructed from the missing mass of $K^+\pi^-$, is show in Figure 3.12. The correlated background appears as a bump peaking around 1.1 GeV/c^2, mainly coming from the reactions:

- $\gamma D \to K^{+*}\Sigma^-(p_s)$,
- $\gamma D \to K^+\Sigma^{-*}(p_s)$,

with K^{+*} and Σ^{-*} decay into $K^+\pi^0$ and $\Sigma^-\pi^0$ respectively[4]. These therefore contribute to $\gamma D \to K^+\Sigma^-(p_s)$ with an additional final state π^0.

The uncorrelated background is a smaller shoulder around 0.8 GeV/c^2 in the missing mass, related to misidentification, prominently from:

- $\gamma D \to \pi^+\pi^- n(p_s)$,
- $\gamma D \to \pi^+\pi^- n(p_s)\pi^0$,

where the π^+ is misidentified as our final state K^+.

The method of using photon timing (Section 3.2.8) and momentum-dependent $\Delta\beta$ cuts (Sections 3.2.6 & 3.2.10) remove large proportion of these misidentified

[4]It should be noted that the notation of (p_s) indicates the spectator proton within deuterium.

particles, however the sample of events selected is still not clean. Figure 3.13 shows the M^2 window for kaon candidates initially and after the timing/$\Delta\beta$ selection; from this the reduction in the background is clearly shown. The final distribution however shows several features that indicate contamination, as highlighted in Figure 3.11.

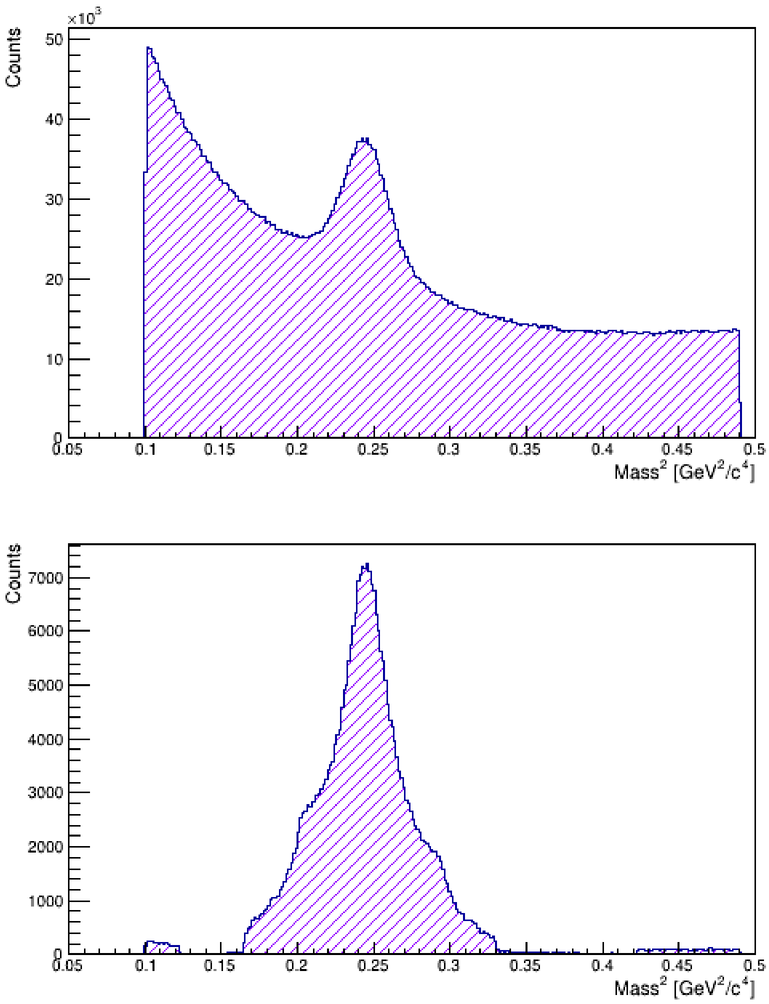

Figure 3.13: Initial K^+ candidates (upper) in comparison to the K^+ candidates after selections performed using $\Delta\beta$ and photon timing (lower).

These background events are dealt with by implementing cuts in the following sections, specifically formulated to identify misidentified particles by looking reaction kinematics, including missing mass distributions and the reconstructed (undetected) neutron mass.

3.2.12.1 Misidentification of π^+ as K^+

The misID of pions as kaons is the major source of background to be contended with in the $K^+\Sigma^-$ channel. In order to separate out the contribution from pions we can exploit the use of the particle PDG masses. The final state $K^+\pi^-$ can be considered for a single event as follows: What if the selected K^+ is really a misidentified π^+, such that the final state is really $\pi^+\pi^-$? If we assign the 'kaon' to have the PDG mass of a pion we can look at a $2D$ representation, allowing us to separate events where the kaons are correctly identified from events where this is incorrect. In this vein Equation 3.13 becomes:

$$MM(K^+_{\pi^+_{PDG}}) = \underline{\underline{\gamma}} + \underline{\underline{n}} - \underline{\underline{K}}^+_{\pi^+_{PDG}}, \tag{3.15}$$

where $K^+_{\pi^+_{PDG}}$, is a kaon candidate which has been assigned the PDG mass of the pion.

This idea can be simply extended, when the reconstruction of the undetected neutron is considered, from Equation 3.14:

$$MM(K^+_{\pi^+_{PDG}}\pi^-) = \underline{\underline{\gamma}} + \underline{\underline{n}} - \underline{\underline{K}}^+_{\pi^+_{PDG}} - \underline{\underline{\pi}}^-. \tag{3.16}$$

The 4-vectors outlined in Equations 3.15 and 3.16 can be plotted in $2D$, as in Figure 3.14.

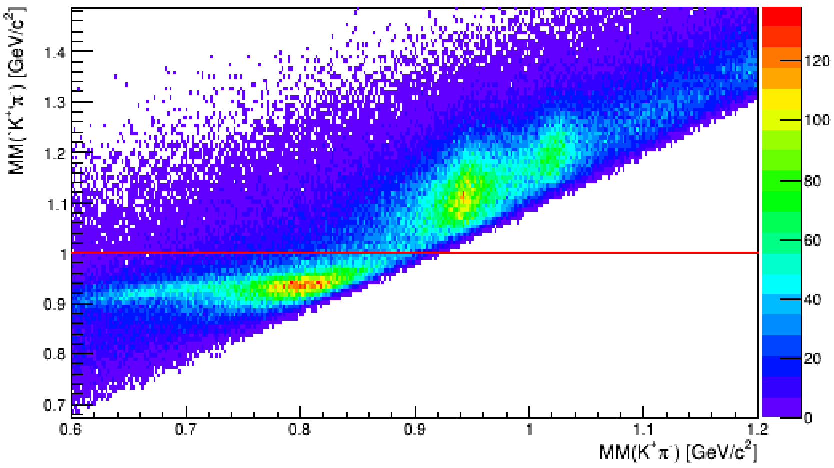

Figure 3.14: Missing mass of $K^+\pi^-$ vs 'K^+'π^-, where 'K^+' has the PDG mass of a π^+. The selection cut is shown in red.

Here the pion band can be seen corresponding to $\sim 0.9\, GeV/c^2$ in $MM($'K^+'$\pi^-)$. This band was analysed by taking projections in $MM($'K^+'$\pi^-)$ and fitting with a Gaussian. These fits were found to be consistent within both the signal and background peaks, therefore a horizontal cut may be applied at $1.0\, GeV$ to remove a large proportion its contribution. The remaining background is not as cleanly separated and will need to be removed by another method.

- $MM(K^+{}_{\pi^+_{PDG}}\pi^-) > 1.0\, GeV$.

Events which do not meet this requirement are removed from the analysis.

3.2.12.2 Misidentification of K^- as π^-

$$MM(K^+\pi^-_{K^-_{PDG}}) = \underline{\underline{\gamma}} + \underline{\underline{n}} - \underline{\underline{K}}^+ - \underline{\underline{\pi}}^-_{K^-_{PDG}}. \tag{3.17}$$

We can consider kaons which are misidentified as pions using a similar method, as in Equation 3.17, although this contribution is far lower than that shown in Section 3.2.12.1. This is plotted in the same way, shown in Figure 3.15.

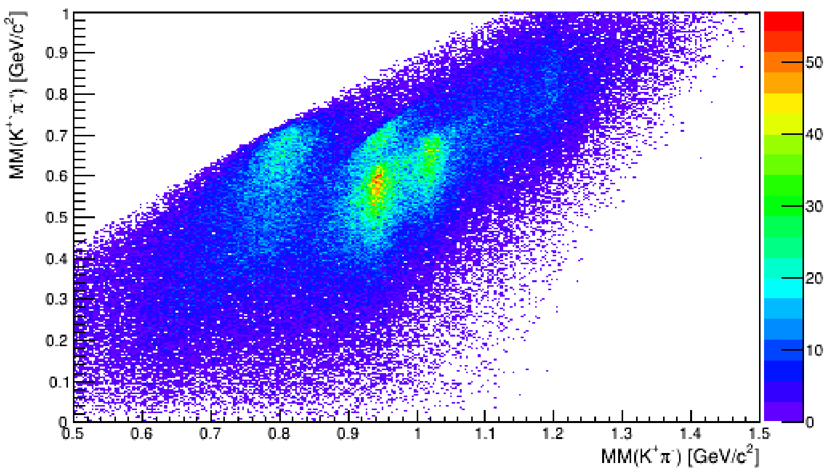

Figure 3.15: Missing mass of $K^+\pi^-$ vs K^+'π^-', where 'π^-' has the PDG mass of a K^-.

The main central peak corresponds to a reconstructed neutron while the right-hand peak shows a neutron plus an additional π^0. These come from the decays; $\gamma D \to K^{+*}\Sigma^-(p_s)$ and $\gamma D \to K^+\Sigma^{-*}(p_s)$. The events we wish to separate are the uncorrelated background present above the neutron peak, as these are kaons which have been misidentified as pions. In order to parameterise a cut in $2D$, projections were taken in $MM($'K^+'$\pi^-)$ and fitted with Gaussians. Due to the proximity of the peaks a width of 1σ in each fit was considered to parameterise a linear cut in $2D$. The majority of this uncorrelated background was removed using this linear cut, shown in Figure 3.16.

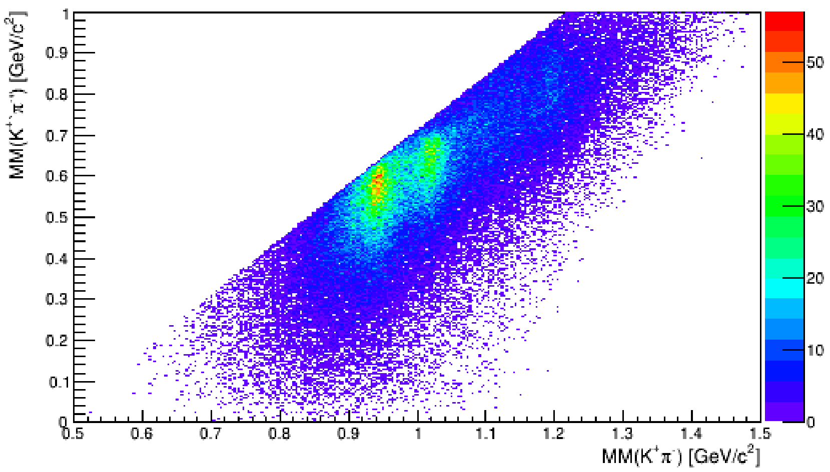

Figure 3.16: Missing mass of $K^+\pi^-$ vs K^+'π^-', after the $2D$ selection cut has been applied.

3.2.12.3 Misidentification of p as K^+

The final, and smallest, contribution from misidentified particles is from protons being falsely identified as kaons. Again, the missing mass can be considered as:

$$MM(K^+_{p_{PDG}}\pi^-) = \underline{\underline{\gamma}} + \underline{\underline{n}} - \underline{\underline{K}}^+_{p_{PDG}} - \underline{\underline{\pi}}^-. \tag{3.18}$$

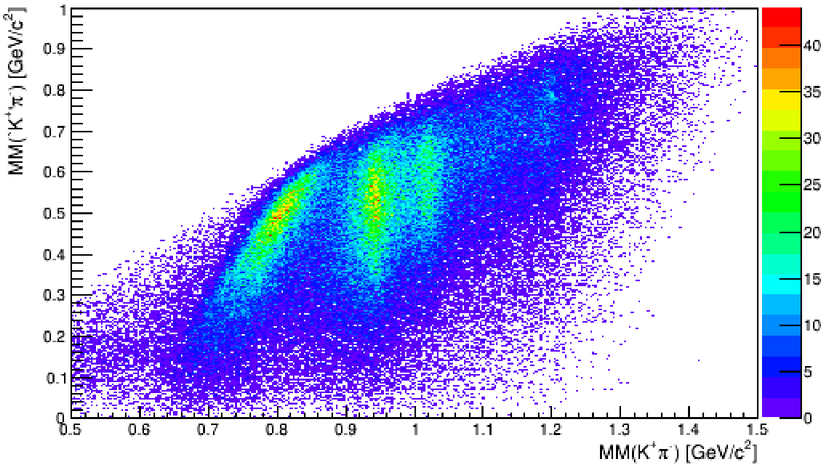

Figure 3.17: Missing mass of $K^+\pi^-$ vs 'K^+'π^-, where 'K^+' has the PDG mass of a p.

This 4-vector is plotted as before and similarly we remove the left peak, as seen in Figure 3.18. This was done by taking projections in $MM(K^+\pi^-)$and fitting with Gaussians. A width of 3σ was considered, in order to parameterise a linear cut in $2D$.

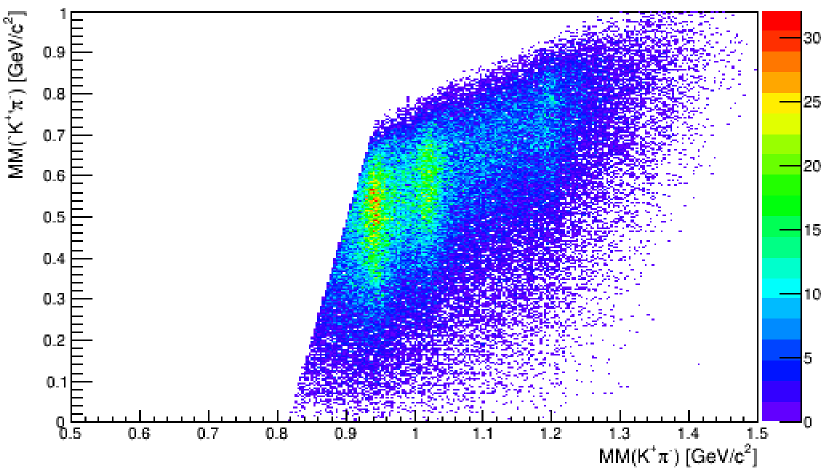

Figure 3.18: Missing mass of $K^+\pi^-$ vs 'K^+'π^-, after the $2D$ selection cut has been applied.

3.2.13 $\Sigma\Lambda$ Separation

In $1D$, we can consider the spectrum of the reconstructed Σ^-, as in Figure 3.19. This explicitly shows the missing mass from the selected kaon. Although there is a clear peak of the Σ^-, there are still peaks present from Λ and $\Sigma^*(1385)$ channels.

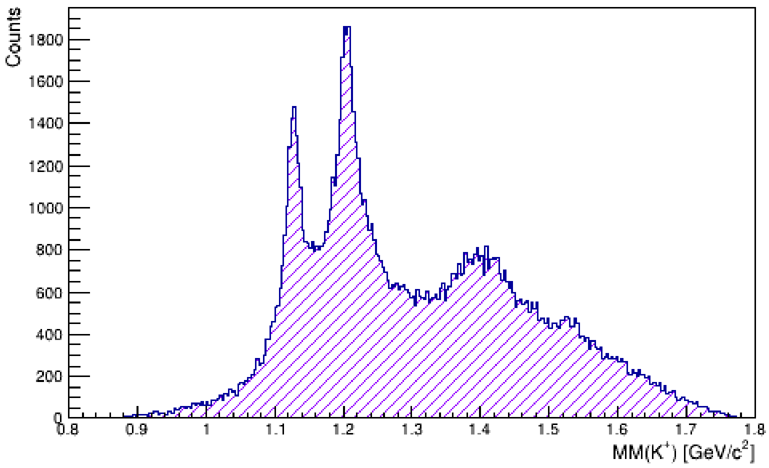

Figure 3.19: Missing mass spectrum of the K^+, clearly showing the Λ, Σ^- and $\Sigma(1385)$.

These background channels decay as follows:

- Λ

$$\begin{aligned} p\pi^- &\propto 63.9\%, \\ n\pi^0 &\propto 35.8\%. \end{aligned} \tag{3.19}$$

- $\Sigma(1385)$

$$\begin{aligned} \Lambda\pi &\propto 87.0\%, \\ \Sigma\pi &\propto 11.7\%, \\ \Lambda\gamma &\propto 1.25\%. \end{aligned} \tag{3.20}$$

This distribution can be considered far more clearly when plotted in $2D$ with $MM(K^+\pi^-)$, as shown in Figure 3.21.

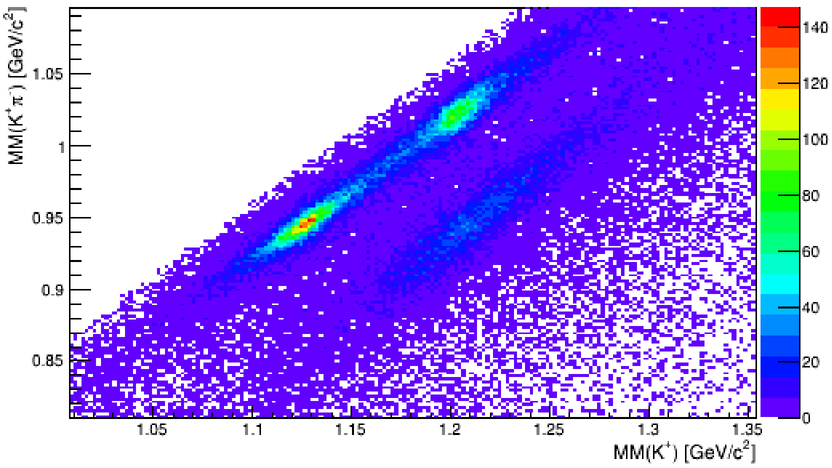

Figure 3.20: $2D$ plot of the reconstructed Σ^- $[MM(K^+)]$ vs. the reconstructed neutron $[MM(K^+\pi^-)]$.

In this plot, the $\Sigma^-(PDG\ 1198\ MeV)$ can be seen; in addition the Λ $(PDG\ 1116\ MeV)$ is also present at lower mass, although clear separation can only be seen in $2D$. Considering the $2D$ distribution also clearly shows a contribution from Σ^0 $(PDG\ 1193\ MeV)$, where there is an additional π^0 in the final state. The Σ^0 decays as follows:

- Σ^0

$$\Lambda\gamma \propto 100\%. \tag{3.21}$$

The Σ^- can then be isolated using a linear cut in $2D$, to remove contributions from Λ and Σ^0. This was parameterised using projections in both $MM(K^+)$ and $MM(K^+\pi^-)$; using 3σ widths to parameterise the selection cut. The distribution after this cut is shown in Figure 3.21.

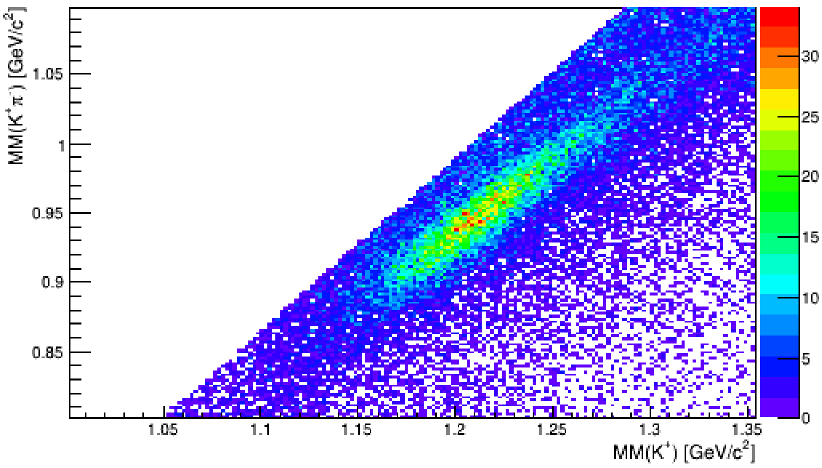

Figure 3.21: $2D$ plot of the reconstructed Σ^- vs the reconstructed neutron after introducing a linear $2D$ selection cut. Both the Λ and Σ^0 peaks are removed, leaving only Σ^-.

3.2.14 Neutron Reconstruction

In order to reconstruct the Σ^-, only the final state kaon is required, however this method comes with a large amount of associated background, mostly in the form of misidentification. To overcome this it is key to also detect the final state pion, in order to reconstruct the neutron from the non-exclusive reaction. Using the missing mass technique, we are able to reconstruct the neutron from the kaon and the pion produced from the Σ^- decay.

The missing mass distribution from Equation 3.14 can be seen in Figure 3.22. The neutron peak (PDG 939.56 MeV) is clear, although a higher mass background can be seen.

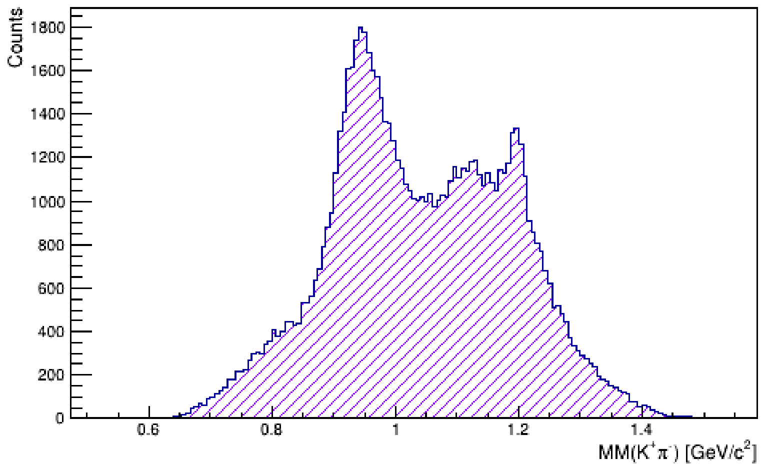

Figure 3.22: Reconstructed neutron using the missing mass technique $[MM(K^{+}\pi^{-})]$ after misID selections have been applied.

The nature of this background is clearer when presented in $2D$ versus momentum of the K^{+}, Figure 3.23. The neutron peak was fitted with a Gaussian, in $1D$, and 1σ cut introduced.

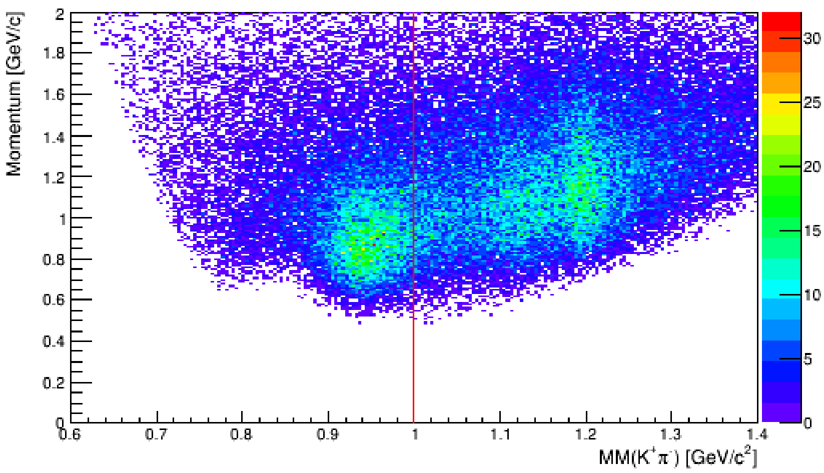

Figure 3.23: Reconstructed neutron using the missing mass technique vs Momentum. The selection cut is shown in red.

- $MM(K^{+}\pi^{-}) < 1.0\ GeV/c^{2}$.

Events which do not meet this requirement are removed from the analysis.

3.2.15 Quasi-free Selection for the Complete Final State

Considering the reaction $\gamma D \rightarrow K^+\Sigma^-(p_s)$ is a different proposal than $\gamma n \rightarrow K^+\Sigma^-$. There are two contributions to this channel, one where the proton is a spectator to the reaction and one where it has an interaction with the produced particles. The former is the quasi-free reaction, where the proton momentum distribution is mainly dominated by the Fermi motion; the latter represents rescattering in which the proton is hit by a kaon or a sigma and gains momentum.

If the final state neutron can be detected, the proton in the deuterium nucleus can be reconstructed. The hope is then that quasi-free regions in this proton can be identified such that the proton is truly a spectator, p_s. For this the spectator proton will recoil with the Fermi momentum of the initial state. In our case, the inability to detect the final state neutron without compromising the available statistical data sample, means that this is not applicable to the main data set but as a formality this procedure will be briefly discussed. The 4-vector equation can be constructed:

$$\underline{\underline{\gamma}} + \underline{\underline{D}} = \underline{\underline{p_s}} + \underline{\underline{K^+}} + \underline{\underline{\pi^-}} + \underline{\underline{n}}. \tag{3.22}$$

Provided the final state neutron can be detected, the undetected proton can then be reconstructed using the missing 4-momentum method:

$$\underline{\underline{p}}_{missing} = \underline{\underline{\gamma}} + \underline{\underline{D}} - \underline{\underline{K}}^+ - \underline{\underline{\pi}}^- - \underline{\underline{n}}. \tag{3.23}$$

The distributions of the reconstructed spectator proton mass and momentum are shown in Figures 3.24 and 3.25 respectively.

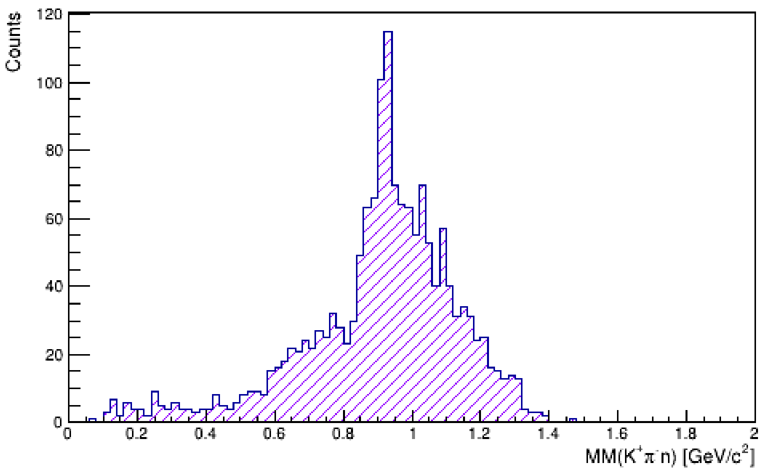

Figure 3.24: Missing mass of the spectator proton, p_s, from the missing mass technique.

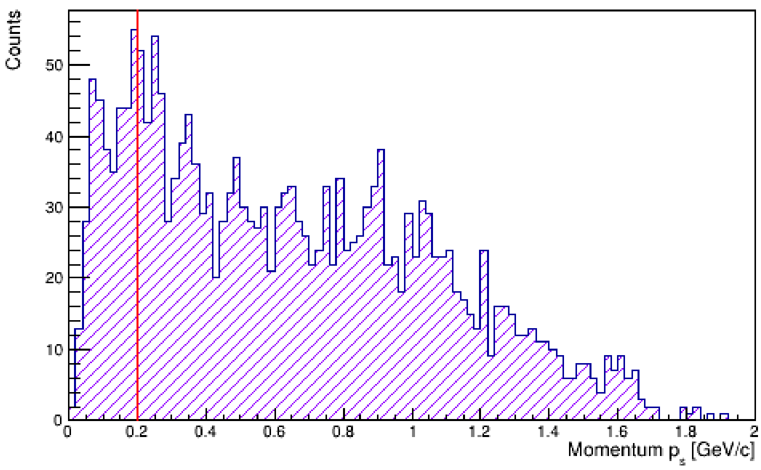

Figure 3.25: Missing momentum of the spectator proton, p_s. The selection cut is shown in red.

The form the missing momentum the quasi-free events can be isolated. The Fermi motion inside the deuteron nucleus results in final state interactions having a greater contribution at high momenta. There should therefore be a restriction placed upon the momentum of the (reconstructed) spectator proton.

- Momentum $p_s < 0.2\ GeV/c$.

For the cases where the neutron is detected, events which do not meet this requirement are removed from the analysis. Note that the fraction of data in which the neutron is detected is small ($\sim 5\%$). The main results for $\mathbb{E}$ are extracted from the larger yield where the final state neutron is not detected.

3.2.16 $K^+\Sigma^-$ Threshold Energy

When considering the $K^+\Sigma^-$ channel, in order to create the final state particles there is a minimum photon energy required. This can be calculated and the minimum threshold energy for the incident photon applied. A typical distribution of the photon energies is given in Figure 3.26.

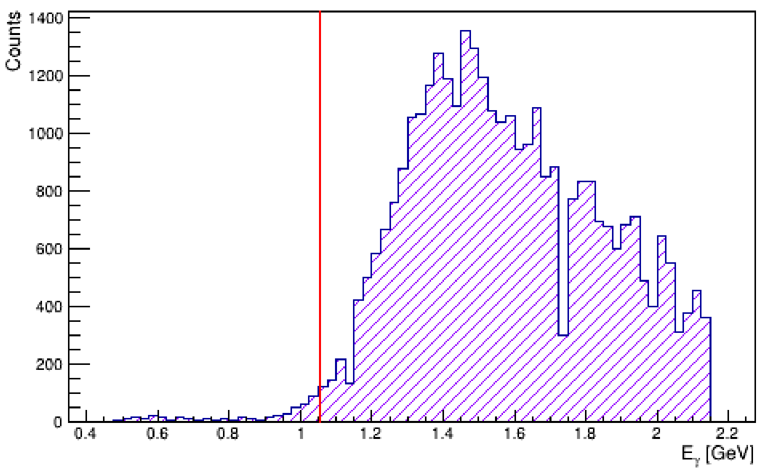

Figure 3.26: A typical spectrum of photon energy when using circularly polarised beam. The selection cut is shown in red.

The energy-momentum relation is used to relate the total energy E, rest mass m_0 and momentum p:

$$E^2 = (pc)^2 + (m_0 c^2)^2, \tag{3.24}$$

where c is the speed of light. This can be reduced, using natural units to:

$$E^2 = p^2 + m_0^2. \tag{3.25}$$

It can then be extended into a many-body equation:

$$\left(\sum_{n}^{n=1,2,...} E_n\right)^2 = \left(\sum_{n}^{n=1,2,...} p_n\right)^2 + (m_0)^2. \tag{3.26}$$

Specifically, considering the final state of $K^+\Sigma^-$, this becomes:

$$(E_\gamma + m_n)^2 = (p_\gamma + p_n)^2 + (m_{K^+} + m_{\Sigma^-})^2. \tag{3.27}$$

We assume that the neutron is at rest in this case for simplicity (although in reality it will have some intrinsic Fermi momentum). This leads to:

$$\begin{aligned} E_\gamma^2 + 2E_\gamma m_n + m_n^2 &= p_\gamma^2 + (m_{K^+} + m_{\Sigma^-})^2, \\ E_\gamma &= \frac{(m_{K^+} + m_{\Sigma^-})^2 - m_n^2}{2m_n}. \end{aligned} \tag{3.28}$$

Substituting the *PDG* particle masses, we find the minimum energy required to produce this final state.

- Threshold energy for photons: $E_\gamma > 1.055\ GeV$.

Events which do not meet this requirement are removed from the analysis.

3.2.17 Event z-vertex

Events must be consistent with a vertex originating from the polarised target material rather than any of the surrounding unpolarised material, thus a selection in the z-vertex must be added. In the case of our reaction channel only the final state kaon originates from the target, whereas the pion has a displaced vertex, as this is a decay product of the Σ^- which will have a decay distance of $c\tau \sim 4.43$ cm. Although this may still decay within the target area, there is a considerable proportion of Σ^- decays which will take place outside of the target. Therefore, it would be unwise to exclude all pion event from out-with the target, as these may-well be consistent with good $K^+\Sigma^-$ events.

The events from the HD were selected by simply looking at the z-vertex (reconstructed from the incident beam and the measured kaon) and applying a cut from -10.5 to -5.5 cm, this excludes events originating from the target cell windows. The distribution of kaons in the z-vertex is shown in Figure 3.27.

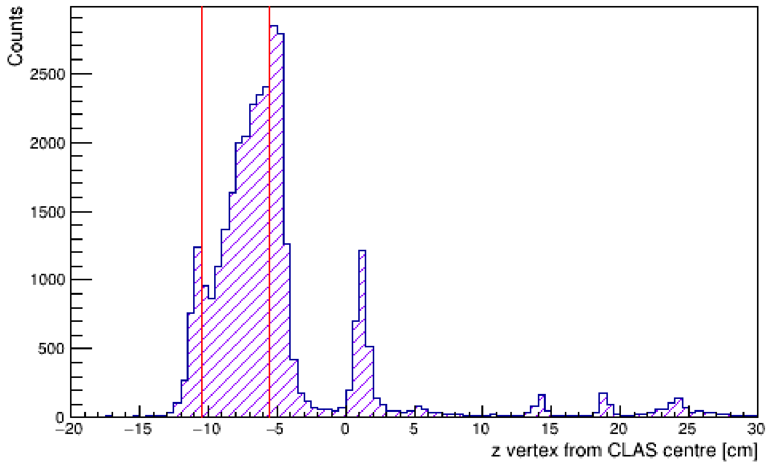

Figure 3.27: K^+ z-vertex from the centre of CLAS. The selection cut is shown in red.

- $(-10.5) < Z_{vert}^{K+} < (-5.5)$ cm.

Events which do not meet this requirement are removed from the analysis.

3.2.17.1 Cell Contributions

It is important to note that although a cut in the z-vertex has been performed, there are still unpolarised events within the sample present from the empty target. In order to maintain the low temperatures required in the cell, the design required aluminium cooling wires to be placed inside and the cell walls to be made of KelF. These materials contain only unpolarised protons and neutrons and so events which consider these as the target proton or neutron will have no analysing power.

Runs with an empty target (containing no polarised material) were conducted in order to assess the contribution from the cell. Note that these runs were conducted for each torus setting ($+1920$ A and -1500 A). The z-vertex distribution from the empty target can be compared to the production target. The peaks outside the polarised target area were normalised by considering the integrals of the region -2 to +30 cm. The empty target data was then scaled to reflect the true contribution in the data, as shown in Figure 3.28. An explicit discussion of the method to account for this target background is given in Section 4.2.

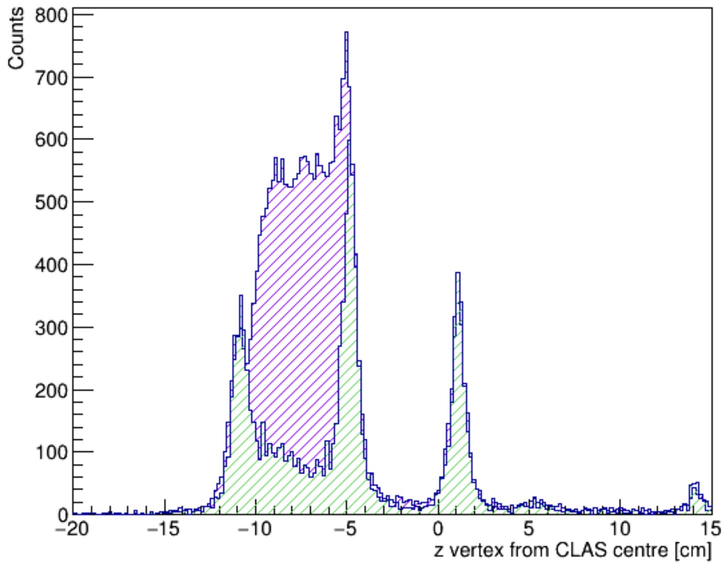

Figure 3.28: K^+ z vertex from the centre of CLAS, compared with scaled empty target data.

3.2.18 Fiducial Cuts

The segmented design of the CLAS detector, using six superconducting coils of the torus magnet leads to low acceptance regions around the sector boundaries, these can be seen in Figure 3.29. These regions are primarily used for placement of cabling and electronics for CLAS sub-detectors, monitoring and are considered as dead regions of the detector. These acceptances are non-uniform close to the sector boundaries and difficult to model accurately as the magnetic field changes quickly.

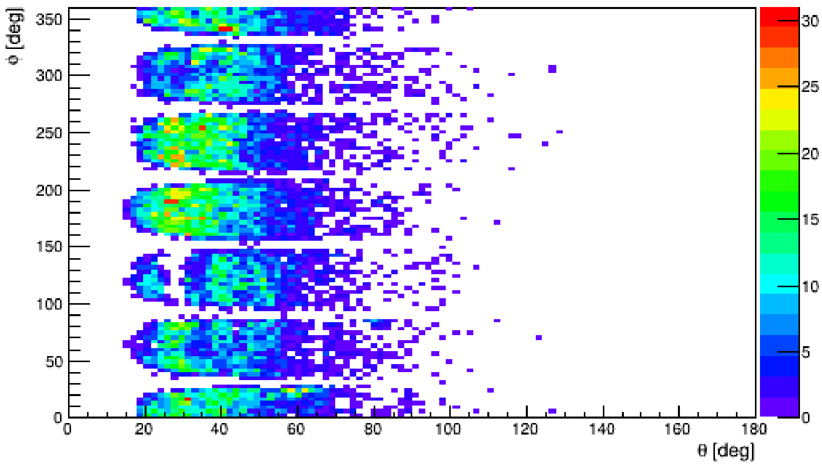

Figure 3.29: K^+ polar vs azimuthal angles.

Events which are detected around these areas tend to have much larger uncertainties and cannot be thought of as reliable, so a standard cut is implemented to remove the regions close to the coils. This selection introduces a 5° band on the azimuthal angle around each coil, the effect of this cut is shown in Figure 3.30.

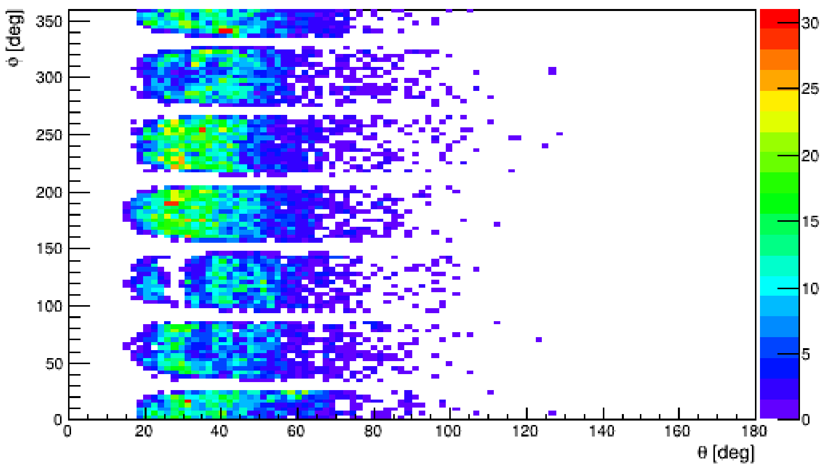

Figure 3.30: K^+ polar vs azimuthal angles, after the removal of the fiducial regions around the CLAS sectors.

The areas removed around the coils are as detailed in Table 4.15.

Coil	Angular Range Removed (°)
1	25 – 35
2	85 – 95
3	145 – 155
4	205 – 215
5	265 – 275
6	325 – 335

Table 3.1: Removed azimuthal regions.

3.2.19 Final Reconstructed Σ^- Selection

The particles to be used in the construction of the $\mathbb{E}$ double-polarisation observable are finally chosen with a selection cut on the mass of the reconstructed Σ^-. A typical distribution of the events is shown in Figure 3.31.

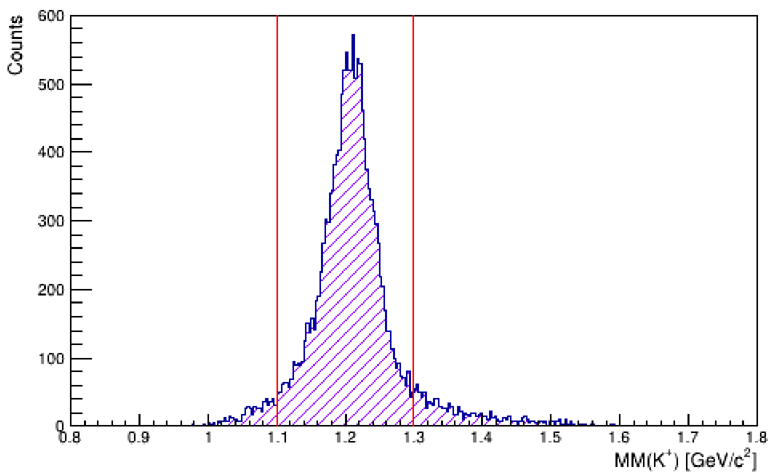

Figure 3.31: Events which have been selected, reconstructed as Σ^-, using the $MM(K^+)$. The selection cut is shown in red.

This is simply fitted with a Gaussian and a 3σ cut applied, giving the final selection of particles used in the construction of the asymmetry.

- $1.10 < M_{\Sigma^-} < 1.30\ GeV/c^2$.

Events which do not meet this requirement are removed from the analysis.

3.2.20 Three particle final state

The desired final state to identify is the full $K^+\pi^-n$, rather than the incomplete $K^+\pi^-$. The detection efficiency of neutrals in CLAS is low and combining this with the relatively low cross section of the channel, this leaves too few events for a useful analysis.

The Σ^- can be reconstructed given a three particle final state using both the missing-mass of the kaon, Figure 3.32, and the invariant mass of the π^-n system, Figure 3.33.

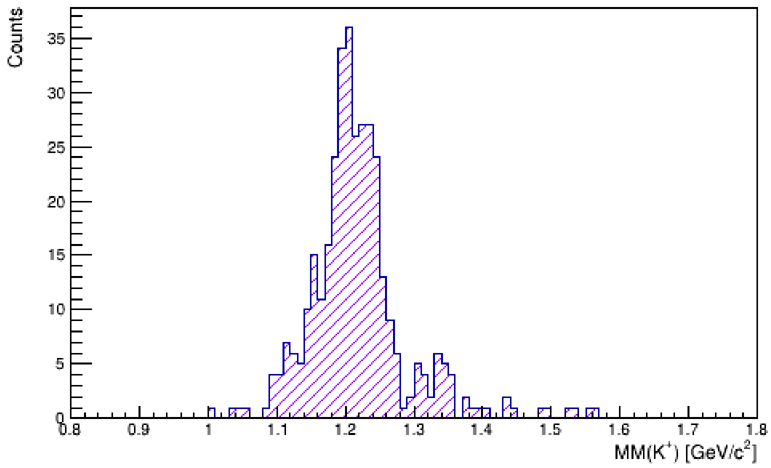

Figure 3.32: Events which has been selected, reconstructed as Σ^-, where the final state neutron has been identified.

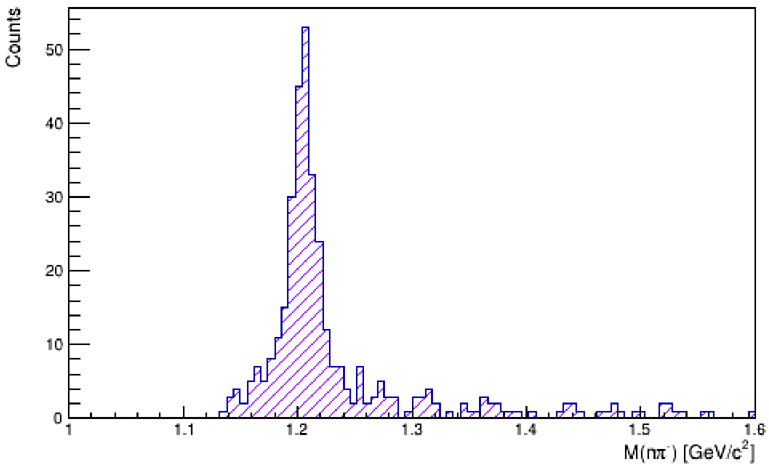

Figure 3.33: Reconstructed Σ^-, using the invariant mass method $[M(n\pi^-)]$.

Comparing these plots to the final selection in the two particle final state, we find a difference in statistics of a factor ~ 20. This would be a preferable final state to analyse, in terms of minimising background and taking advantage of the ability to use the invariant mass, as has been done in measurements of the cross section [24], however the statistics available for this work does not make this viable.

3.2.21 Summary

A summary of the applied selection cuts and corrections in this chapter are outlined below.

Cut	Constraint
Particle Multiplicity	2 or 3 final state particles
Tagger Condition	Events must have a valid hit in the tagger
DC Condition	For charged particles require an event in the DC
SC Condition	For charged particles require and event in the ToF
EC Condition	For neutral particle require an event in the EC
Charge Removal	For charged particles, require only one unit of charge
Kaon M^2	$0.1 < M^2_{K^+} < 0.49\ GeV^2/c^4$
Pion M^2	$0.0 < M^2_{\pi^-} < 0.1\ GeV^2/c^4$
Neutron β	$\beta_n < 0.9$
Topology	Final state $K^+\pi^-$ or $K^+\pi^-n$
Kaon $\Delta\beta$	Momentum dependant, see 3.2.6
Pion $\Delta\beta$	$\lvert\Delta\beta_{\pi^-}\rvert < 0.051$
Candidate Photons	$NGRF_{K^+} = NGRF_{\pi^-} = 1$
Event best photon	$TAGRID_{K^+} = TAGRID_{\pi^-}$
Best photon selection	$\lvert\Delta t_{\pi^-}\rvert < 1.5\ ns$
Post correction $\Delta\beta$	$\lvert\Delta\beta_{K^+/\pi^-}\rvert < 0.036$
Misidentification π^+	Remove π^+ selected as K^+
Misidentification K^-	Remove K^- selected as π^-
Misidentification p	Remove p selected as K^+
Σ^-/Λ Separation	see 3.2.13
Reconstructed neutron	$MM(K^+\pi^-) < 1.0\ GeV/c^2$
Threshold energy	$E_\gamma > 1.055\ GeV$
Z-vertex	$-10.5 < z_{K^+} < -5.5\ cm$
Fiducial	$\pm 5^\circ$ around sector boundaries
Sigma mass	$1.10 < M_{\Sigma^-} < 1.30\ GeV/c^2$

Table 3.2: Table summarising the particle identification cuts of the $K^+\Sigma^-$ channel.

Chapter 4

Systematic Studies

In this chapter, systematic studies performed on the $g14$ data are considered. These include the target subtraction method, as well as studies attempting to quantify the magnitude of systematics caused by the selection cuts imposed and the influence of the $K^+\Sigma^0$ background on the final results of the double-polarisation observable $\mathbb{E}$.

4.1 Asymmetry of Empty (Unpolarised) Targets

A first test of the integrity of the data and analysis method is to extract the asymmetry from the unpolarised (or empty) target. This of course should be consistent with zero as the target cell itself is made of only non-polarised protons and neutrons. The analysis also allows these events to be removed or accounted for when calculating the value of $\mathbb{E}$, as these target support structures will still contribute to the yield with the polarised material in place.

The plots given in Figures 4.1 - 4.4 show the $\mathbb{E}$ observable across all energy bins along with a linear fit for the *emptyA* period, the results of which are provided in Table 4.1. Similar results are shown for the *emptyB* period in Figures 4.5 - 4.8, with the results shown in Table 4.2. It should be noted that empty bins correspond to points which are not statistically defined due to insufficient events (i.e. the extracted value of $\mathbb{E}$ has errors greater than ± 1).

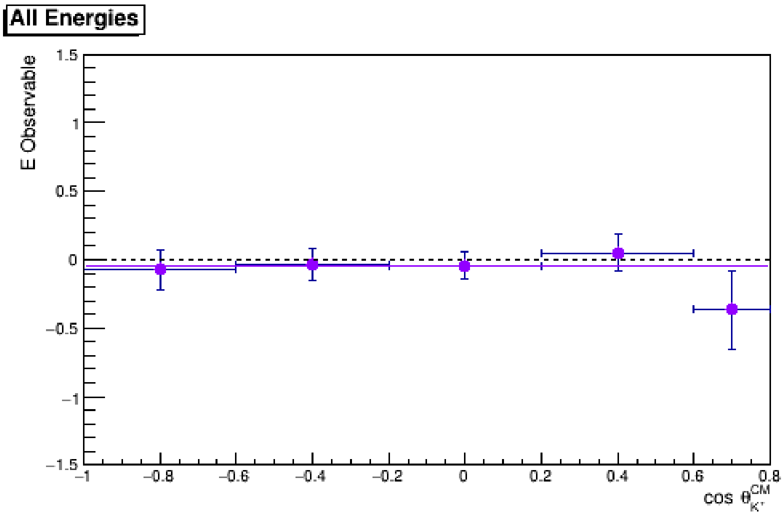

Figure 4.1: $\mathbb{E}$ double-polarisation observable for empty target period A: *all energies* (1.1-2.3 GeV).

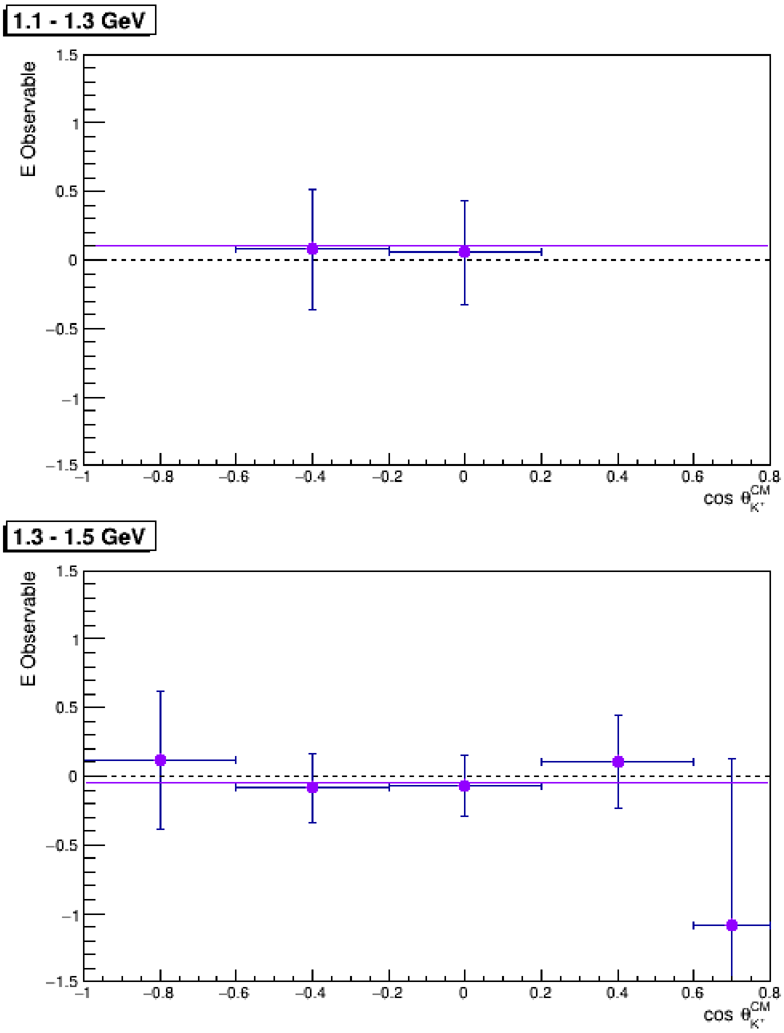

Figure 4.2: $\mathbb{E}$ double-polarisation observable for empty target period A: 1.1-1.3 GeV (upper), 1.3-1.5 GeV (lower).

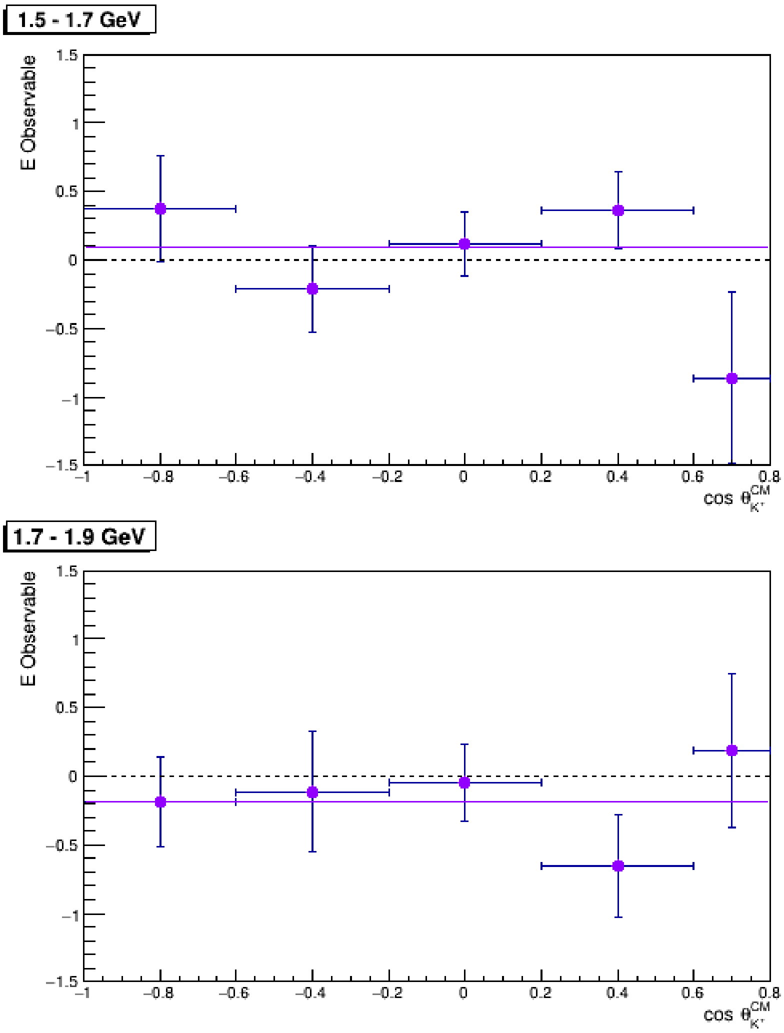

Figure 4.3: $\mathbb{E}$ double-polarisation observable for empty target period A: 1.5-1.7 GeV (upper), 1.7-1.9 GeV (lower).

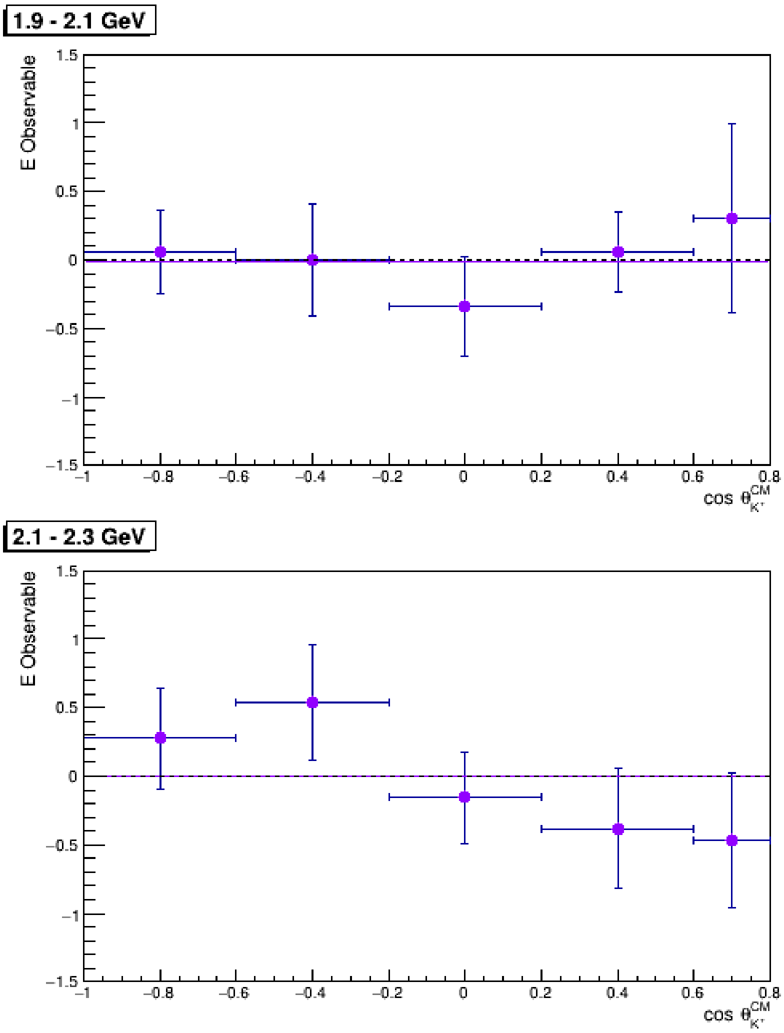

Figure 4.4: $\mathbb{E}$ double-polarisation observable for empty target period A: 1.9-2.1 *GeV* (upper), 2.1-2.3 *GeV* (lower).

Empty Target A			
E_γ Bin (GeV)	Fit value	Fit Error	χ^2/dof
All Energies	-0.04	0.06	0.45
1.1-1.3	0.10	0.26	1.51
1.3-1.5	-0.04	0.14	0.25
1.5-1.7	0.10	0.14	1.15
1.7-1.9	-0.18	0.16	0.57
1.9-2.1	-0.01	0.16	0.28
2.1-2.3	-0.01	0.18	1.03

Table 4.1: Summary of linear fitting to $\mathbb{E}$ double-polarisation observable for the empty target A.

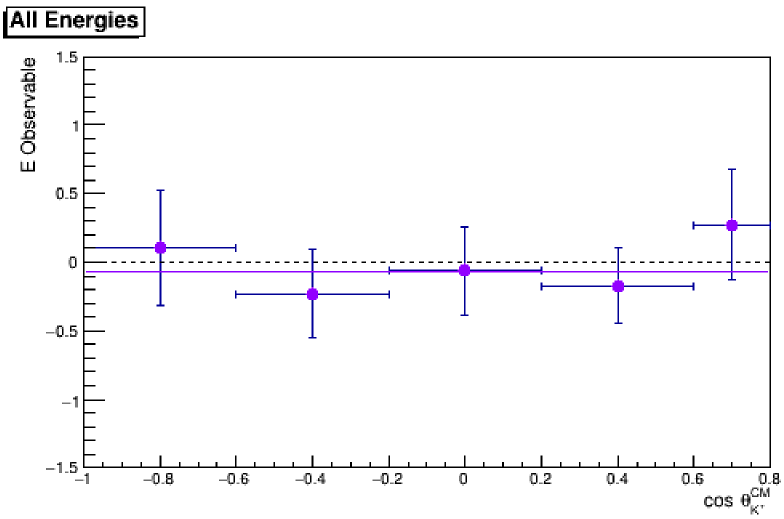

Figure 4.5: $\mathbb{E}$ double-polarisation observable for empty target period B: *all energies* (1.1-2.3 GeV).

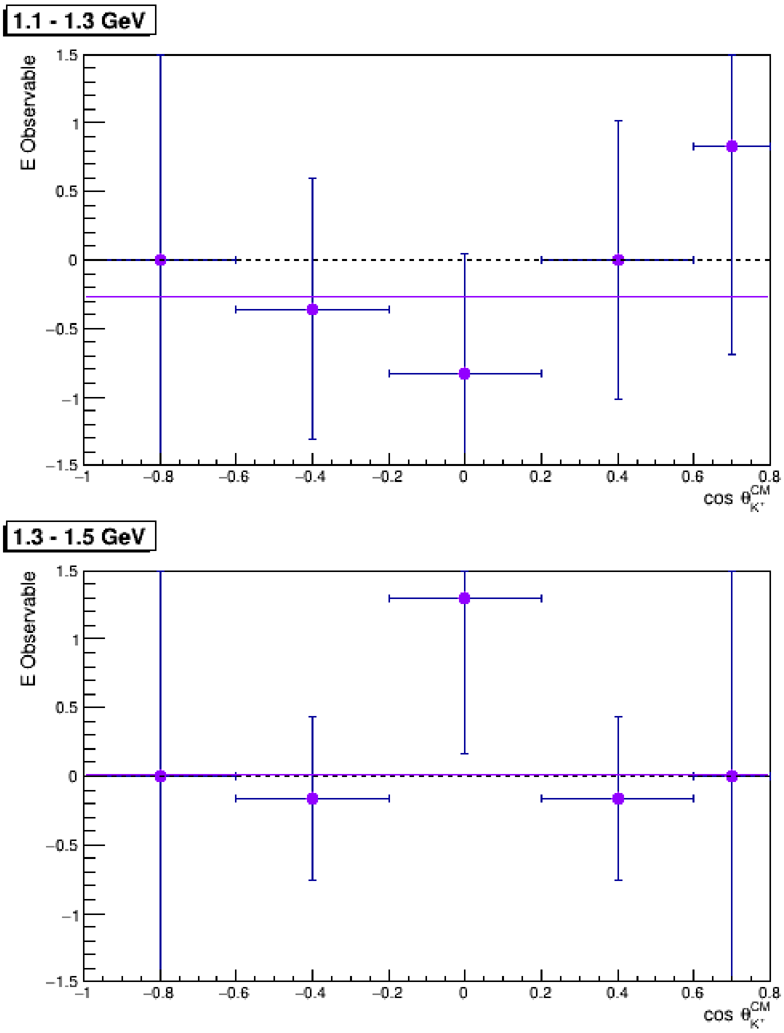

Figure 4.6: $\mathbb{E}$ double-polarisation observable for empty target period B: 1.1-1.3 GeV (upper), 1.3-1.5 GeV (lower).

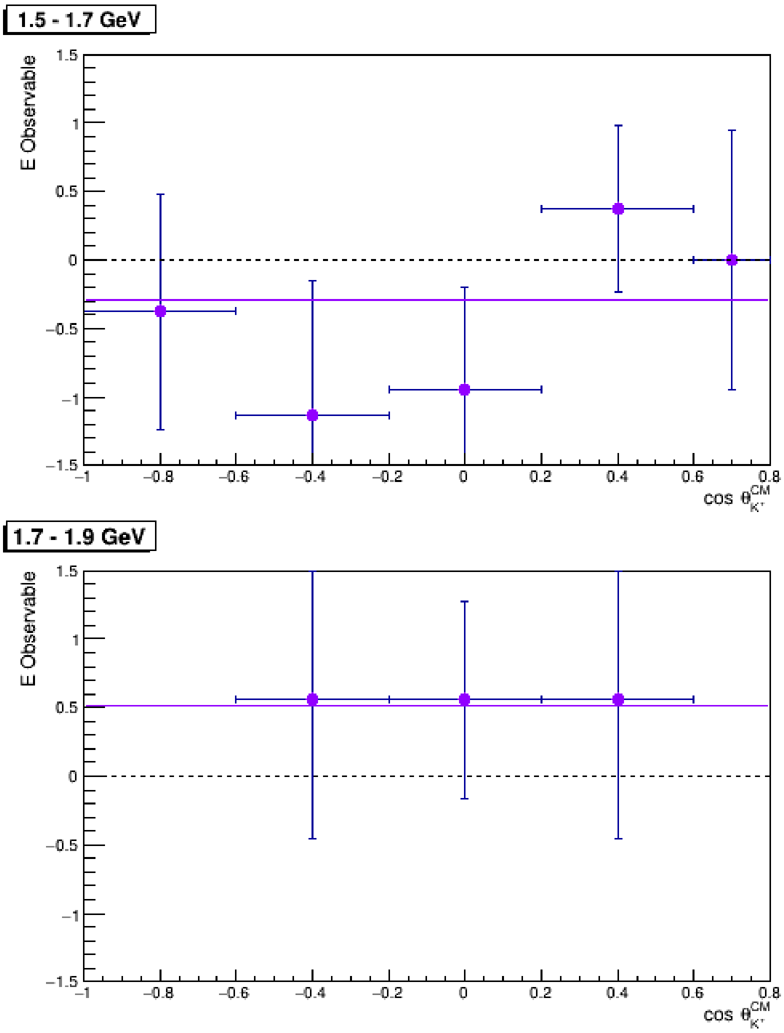

Figure 4.7: $\mathbb{E}$ double-polarisation observable for empty target period B: 1.5-1.7 GeV (upper), 1.7-1.9 GeV (lower).

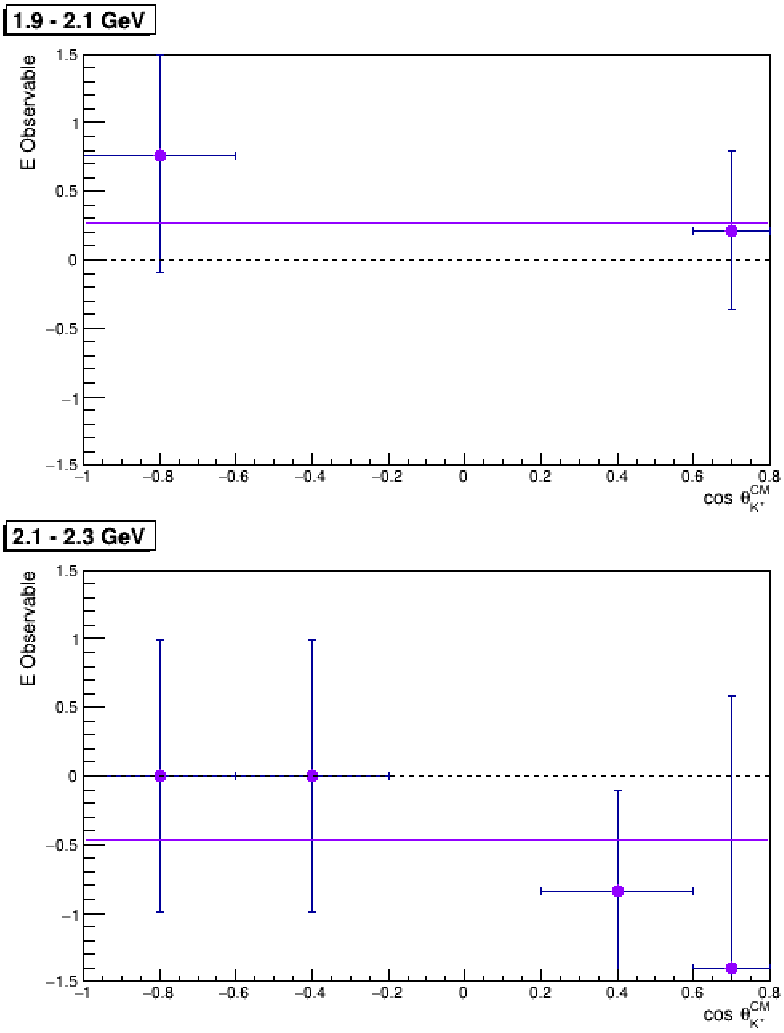

Figure 4.8: $\mathbb{E}$ double-polarisation observable for empty target period B: 1.9-2.1 *GeV* (upper), 2.1-2.3 *GeV* (lower).

From these results, we can see that the target value of $\mathbb{E}$ is consistent with zero for both targets at all energies as there is no statistically significant deviation from zero, with the typical χ^2/dof highlighting the small number of events present in the data-sample. Therefore, it can be said that an empty target cell does not contribute to the asymmetry.

Empty Target B			
E_γ Bin (GeV)	Fit value	Fit Error	χ^2/dof
All Energies	-0.06	0.15	0.32
1.1-1.3	-0.27	0.49	0.26
1.3-1.5	0.01	0.37	0.35
1.5-1.7	-0.29	0.35	0.7
1.7-1.9	0.51	0.48	0.28
1.9-2.1	0.27	0.44	0.69
2.1-2.3	-0.46	0.49	0.31

Table 4.2: Summary of linear fitting to $\mathbb{E}$ double-polarisation observable for the empty target B.

4.2 Empty Target Removal Methods

The cell walls of the HD target will remain present in the events selected. It is important to remove this contribution as these protons and neutrons are not polarised. Including these non-polarised events would lead to a dilution in the asymmetry and the value of the polarisation observable $\mathbb{E}$. To account for this effect, two paths can be taken. Firstly, the removal of the empty target data using a simple subtraction or secondly by diluting the asymmetry in order to account for the unpolarised material. Both methods are considered in this analysis note and compared for consistency.

4.2.1 Empty Target Subtraction

The first method attempts to subtract the yield from the unpolarised empty target cell material before calculating the $\mathbb{E}$ observable. To achieve this, a suitable normalisation of the empty target data must be made to accurately assess its contribution to the polarised target run period.

The method adopted was to normalise the yield from the empty and polarised run periods for beam-line components downstream of the target cell. These should give the same contribution to the yield from both run periods if the normalisation is correct. A typical target distribution is shown in Figure 4.9; the spikes seen at

$z > 0$ cm are peaks which characterise the physical structure of the cell.

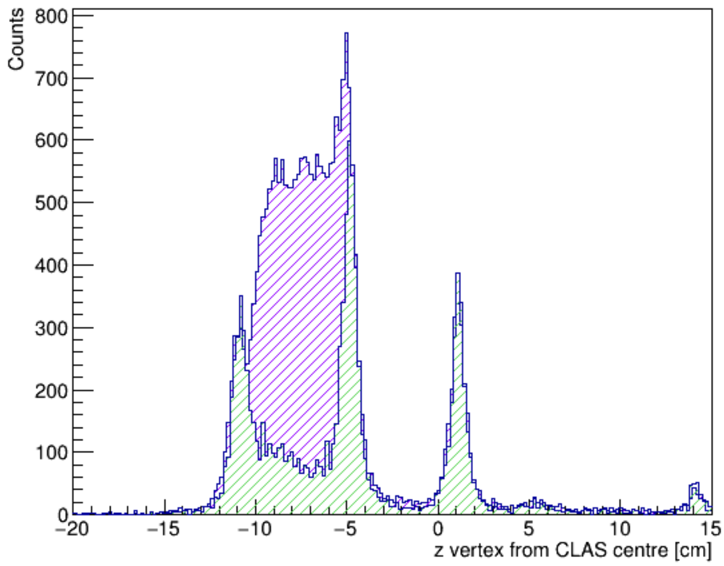

Figure 4.9: K^+ z vertex from the centre of CLAS, compared with scaled empty target data.

The yield of events, Y_{total}, from running with the polarised HD target can be expressed as having contributions from the polarised HD, Y_{HD}, and the non-polarised target cell, Y_{empty}:

$$Y_{total} = Y_{HD} + Y_{empty}. \tag{4.1}$$

This can then be separated into the aligned and anti-aligned helicity conditions, where the beam (magnitude 1) and target (magnitude 1/2) polarisation vectors are parallel and anti-parallel respectively:

$$\begin{aligned} Y_{HD}^{\frac{3}{2}} &= Y_{total}^{\frac{3}{2}} - \frac{\epsilon}{2} Y_{empty}, \\ Y_{HD}^{\frac{1}{2}} &= Y_{total}^{\frac{1}{2}} - \frac{\epsilon}{2} Y_{empty}, \end{aligned} \tag{4.2}$$

where we also introduce a normalisation factor, ϵ. The factor 2 is introduced to ensure a zero contribution to the asymmetry from the empty data.

The z component of the interaction vertex for empty target and full target runs are plotted, Figure 4.9. The histograms are scaled in order to account for differences in beam and run time[1].

It is clear that the yields from the downstream components in the beam-line are in good agreement between the production data and the scaled empty target data. Target scaling is done in each E_γ bin rather than across the whole energy range, in an attempt to account for variations seen across the energy range. The scaled empty target events are then subtracted from the production data. This is the used in association with the average photon beam polarisation of the energy bin, giving the total scaling factor. Typical scalings for each energy bin are presented in Table 4.3.

E_γ Bin (GeV)	Empty Target Scaling
1.1-2.3	6.5
1.1-1.3	9.5
1.3-1.5	8.1
1.5-1.7	7.1
1.7-1.9	6.2
1.9-2.1	5.6
2.1-2.3	5.2

Table 4.3: Summary of the empty target scaling factor with respect to the selected photon energy bins, $1/(\bar{P}_\gamma P_\oplus)$.

4.2.2 Empty Target Dilution Factor

The second approach to dealing with the empty target contribution is to leave the yield in the data sample used to calculate the asymmetry - but to calculate the resulting dilution of the extracted value due to the unpolarised contribution.

We can consider the yield of events, as in Equation 1.6, for the signal (S) and empty target (E) respectively:

[1] Note that there exists a special case for the $Gold2$ target, as there are less aluminium wires in the cell. As such, there is an additional factor of 0.7 introduced in the scaling.

$$Y_S^{\pm} = A_S^{\pm}(1 \mp \mathbb{E}P_{\gamma}P_{\oplus}), \tag{4.3}$$

$$Y_E^{\pm} = A_E^{\pm}(1 \mp \mathbb{E}P_{\gamma}P_{\oplus}), \tag{4.4}$$

where $\pm$ indicates the beam helicity and $A^{\pm}$ represents some acceptance present. As it has been shown in Section 4.1, the value of the $\mathbb{E}$ observable is consistent with zero for the empty target. Hence, the second term within Equation 4.4 is in fact zero.

If the total yield of events for a process is considered, where there is some weighting of the true signal and empty target, Equations 4.3 and 4.4 can be combined as follows:

$$\begin{aligned} Y_T^{\pm} &= Y_S^{\pm} + Y_E^{\pm}, \\ &= A_S^{\pm} + A_E^{\pm} \mp A_S^{\pm} E P_{\gamma} P_{\oplus}, \end{aligned} \tag{4.5}$$

$$Y_T^{\pm} = A_T^{\pm} \mp A_S^{\pm} E P_{\gamma} P_{\oplus}, \tag{4.6}$$

where $A_S^{\pm}$ and $A_E^{\pm}$ have been enveloped into some total acceptance $A_T^{\pm}$. Using this, the total asymmetry of yields can be constructed, similarly to Equation 1.5:

$$\begin{aligned} \mathcal{A} &= \frac{Y_T^- - Y_T^+}{Y_T^- + Y_T^+}, \\ &= \frac{(A_T^- + A_S^- E P_{\gamma} P_T) - (A_T^+ - A_S^+ E P_{\gamma} P_T)}{(A_T^- + A_S^- E P_{\gamma} P_T) + (A_T^+ - A_S^+ E P_{\gamma} P_T)}. \end{aligned} \tag{4.7}$$

We assume that the acceptance effects for both $\pm$ cases are equivalent, which then allows us to simplify to:

$$\mathcal{A} = \frac{A_S E P_{\gamma} P_{\oplus}}{A_T}. \tag{4.8}$$

It is important to note that A_S is not known as the signal cannot be sufficiently separated from the total and empty data. $\mathbb{E}$ can then be written:

$$\begin{aligned}
\mathbb{E} &= \frac{A_T}{A_S}\frac{1}{P_\gamma P_\oplus}\mathcal{A}, \\
&= \frac{A_T}{A_T - A_E}\frac{1}{P_\gamma P_\oplus}\mathcal{A}, \\
&= \frac{1}{\frac{A_T - A_E}{A_T}}\frac{1}{P_\gamma P_\oplus}\mathcal{A}, \\
&= \frac{1}{1 - \frac{A_E}{A_T}}\frac{1}{P_\gamma P_\oplus}\mathcal{A},
\end{aligned} \tag{4.9}$$

$$\mathbb{E} = \frac{1}{1 - \frac{\epsilon N_E}{N_T}}\frac{1}{P_\gamma P_\oplus}\mathcal{A}, \tag{4.10}$$

where $N_{E/T}$ are the number of events in the empty target and total data respectively, while ϵ is the scaling factor of the empty target in regions outside the target material.

The additional factor present in Equation 4.10 represents the dilution factor and uses the calculated scaling of the empty target to account for the contribution of the target cell to the polarisation observable $\mathbb{E}$.

4.2.3 Empty Target Results

The results for the $\mathbb{E}$ observable are shown, binned in 200 MeV energy bins (E_γ) as a function of the kaon centre-of-mass angle ($\cos\theta^{CM}_{K^+}$) with bins of width 0.4. A comparison is made between the empty target subtraction and dilution methods.

4.2.3.1 Empty Target Dilution Method

The motivation behind this method were outlined in Section 4.2.2, with the results for the $\mathbb{E}$ double-polarisation observable for the target dilution method shown in Figures 4.10 - 4.13:

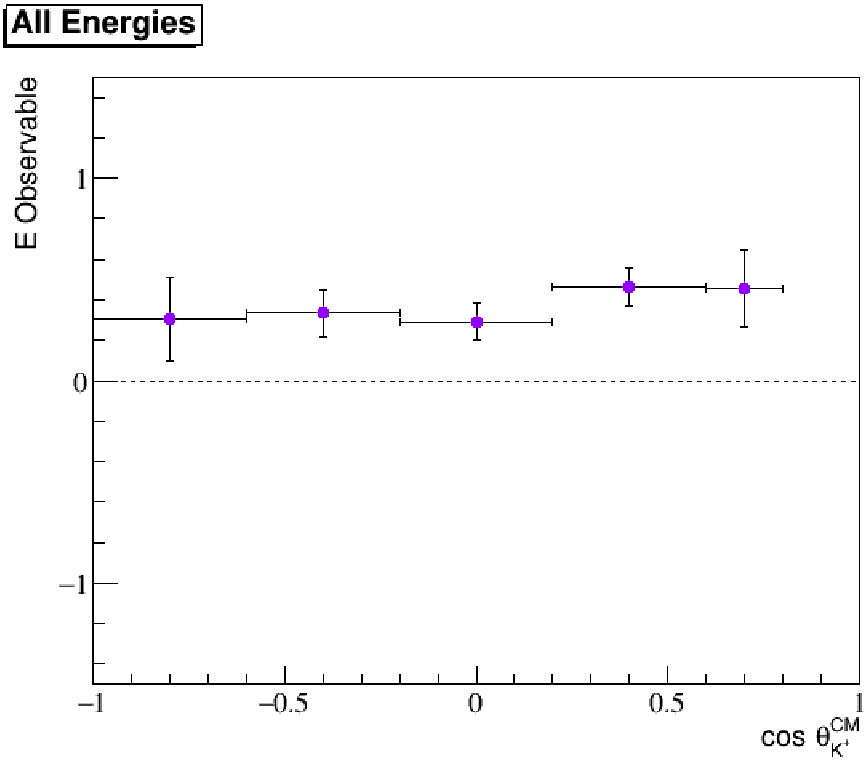

Figure 4.10: Results for the $\mathbb{E}$ double-polarisation observable using the target dilution method: *All energies* (1.1-2.3 *GeV*).

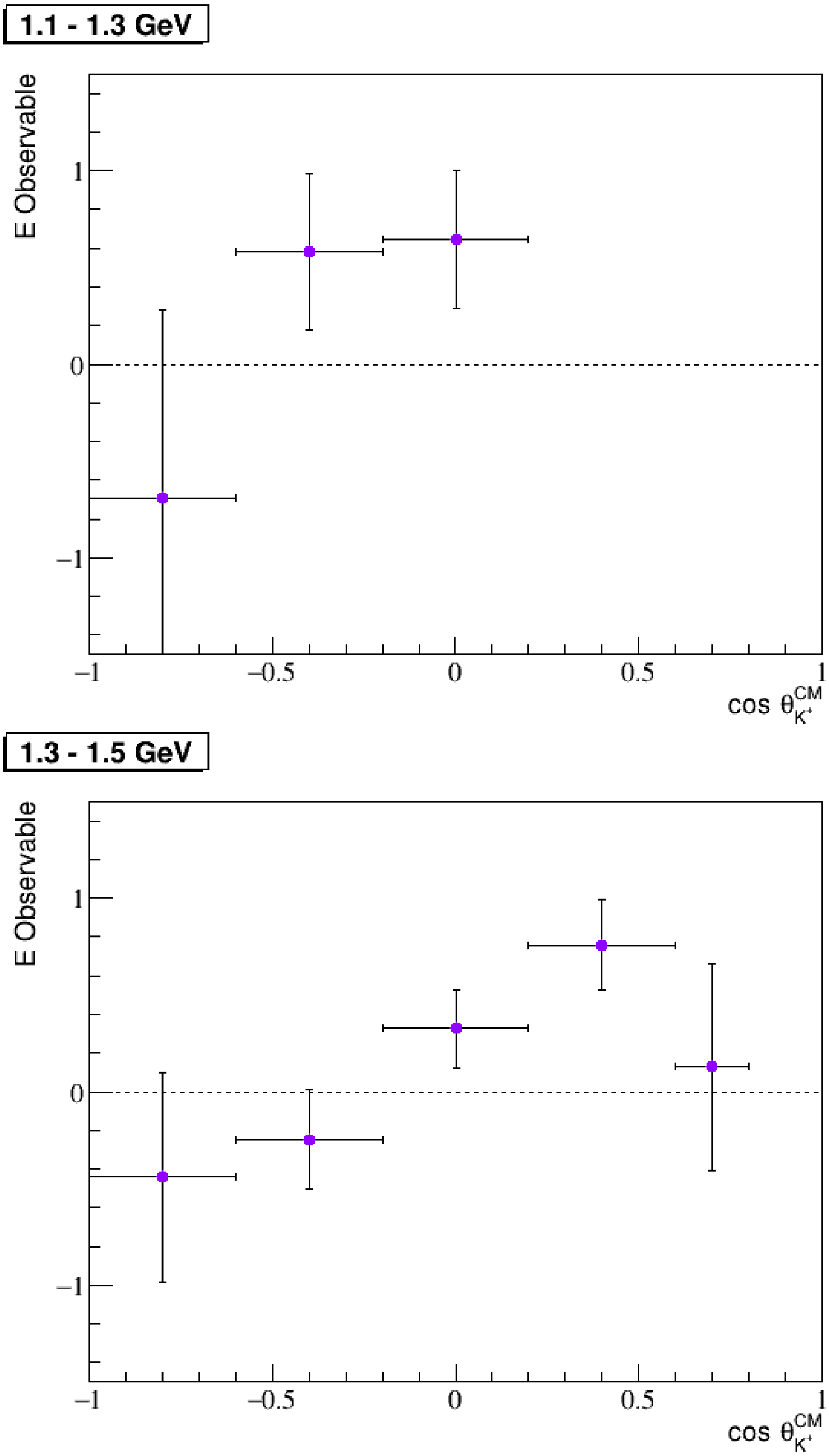

Figure 4.11: Results for the $\mathbb{E}$ double-polarisation observable using the target dilution method; 1.1-1.3 *GeV* (upper), 1.3-1.5 *GeV* (lower).

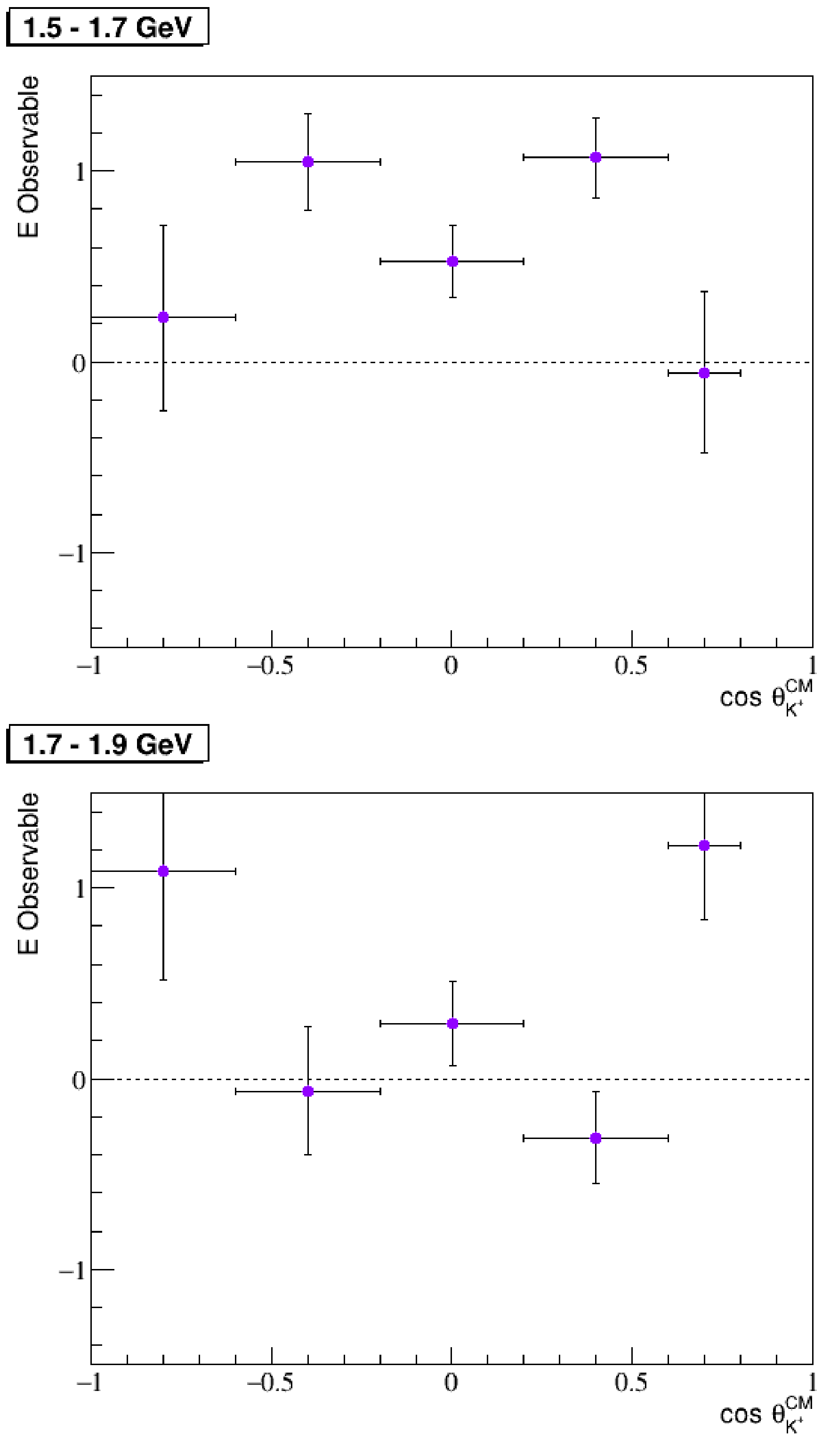

Figure 4.12: Results for the $\mathbb{E}$ double-polarisation observable using the target dilution method; 1.5-1.7 GeV (upper), 1.7-1.9 GeV (lower).

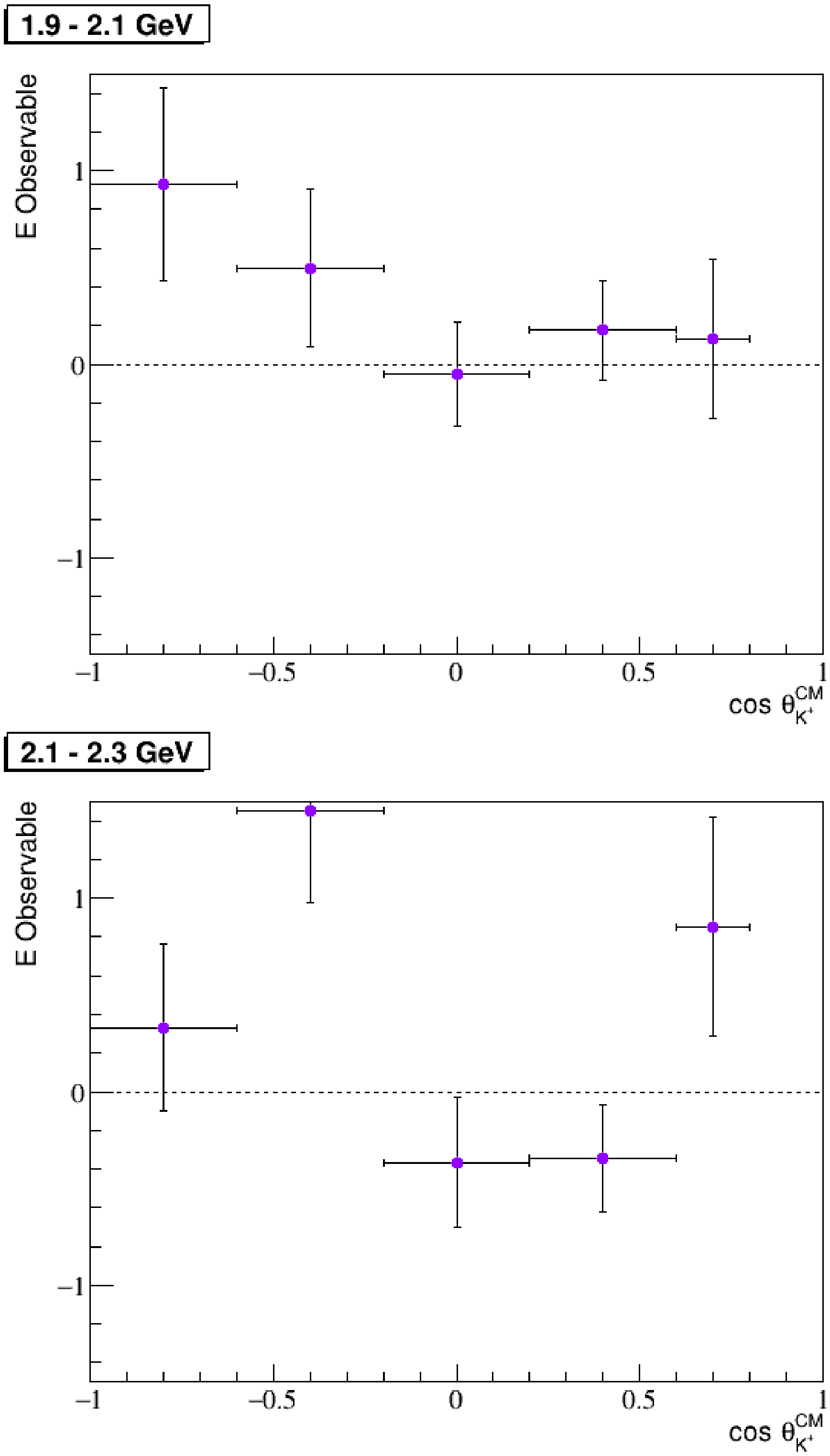

Figure 4.13: Results for the $\mathbb{E}$ double-polarisation observable using the target dilution method; 1.9-2.1 *GeV* (upper), 2.1-2.3 *GeV* (lower).

4.2.3.2 Empty Target Subtraction Method

The motivation behind this method were outlined in Section 4.2, with the results for the $\mathbb{E}$ double-polarisation observable for the target subtraction method shown in Figures 4.14 - 4.17:

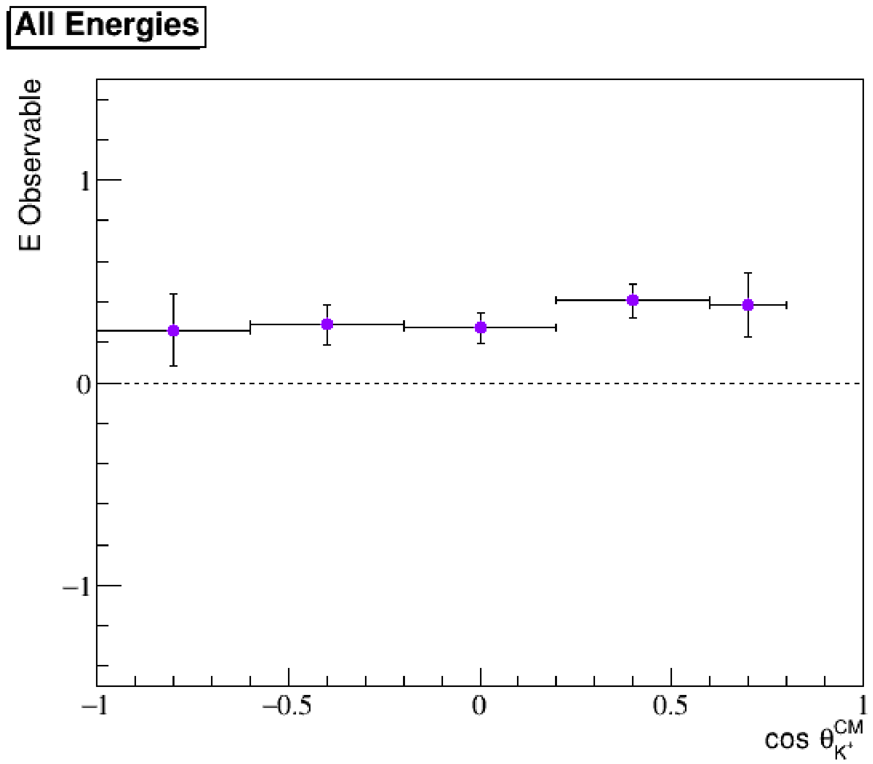

Figure 4.14: Results for the $\mathbb{E}$ double-polarisation observable using the target subtraction method: *All energies* (1.1-2.3 GeV).

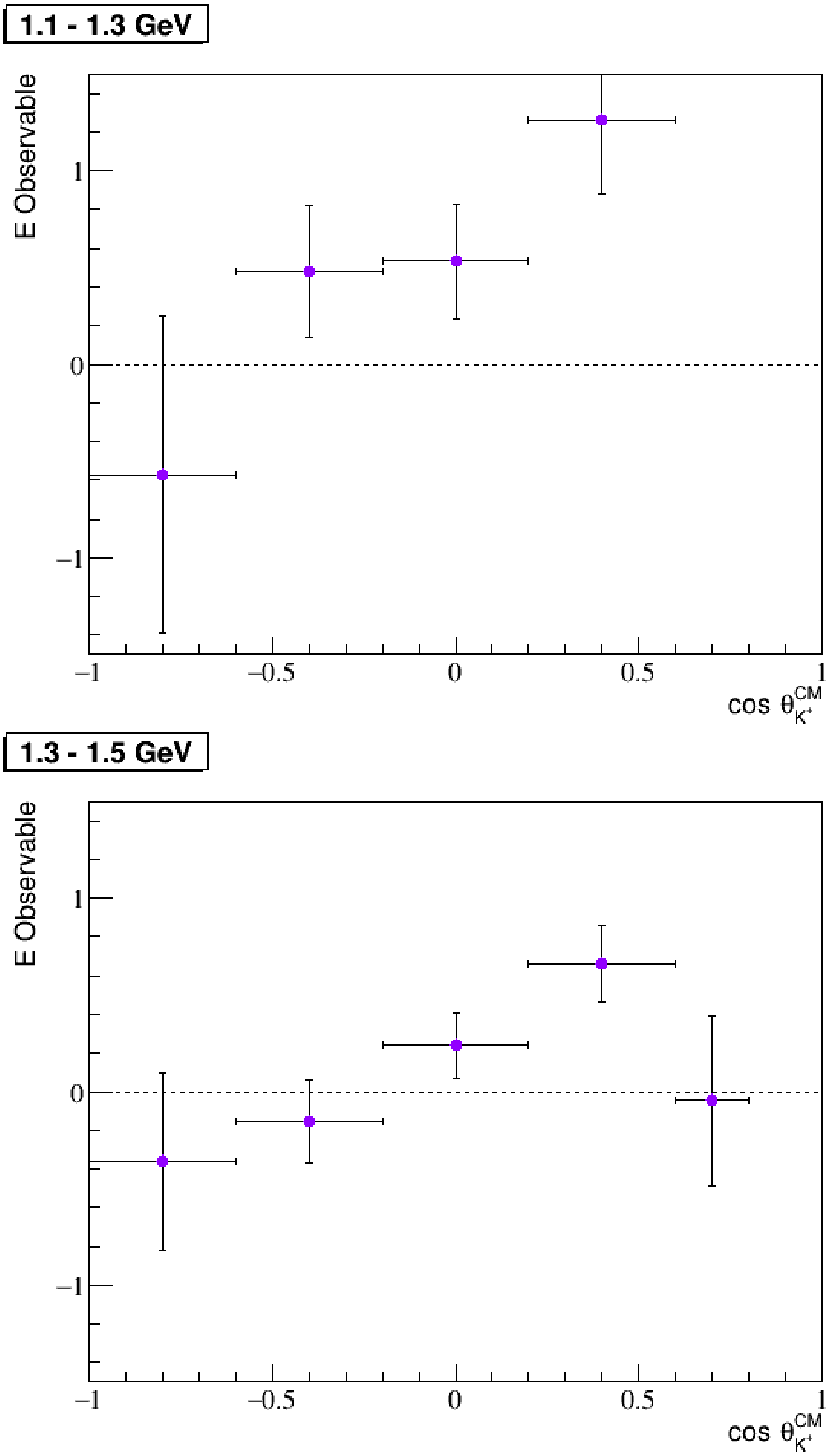

Figure 4.15: Results for the $\mathbb{E}$ double-polarisation observable using the target subtraction method; 1.1-1.3 GeV (upper), 1.3-1.5 GeV (lower).

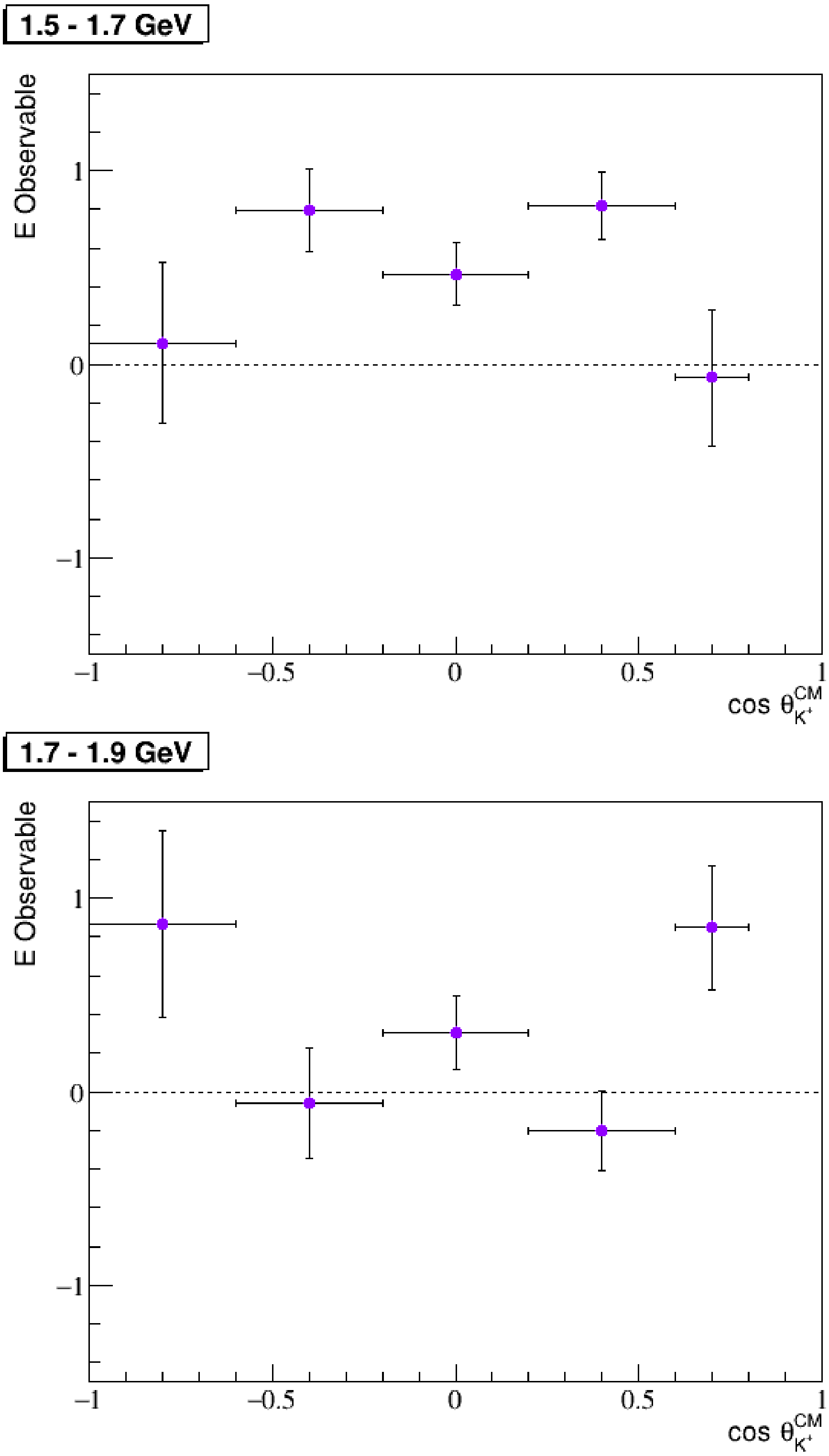

Figure 4.16: Results for the $\mathbb{E}$ double-polarisation observable using the target subtraction method; 1.5-1.7 GeV (upper), 1.7-1.9 GeV (lower).

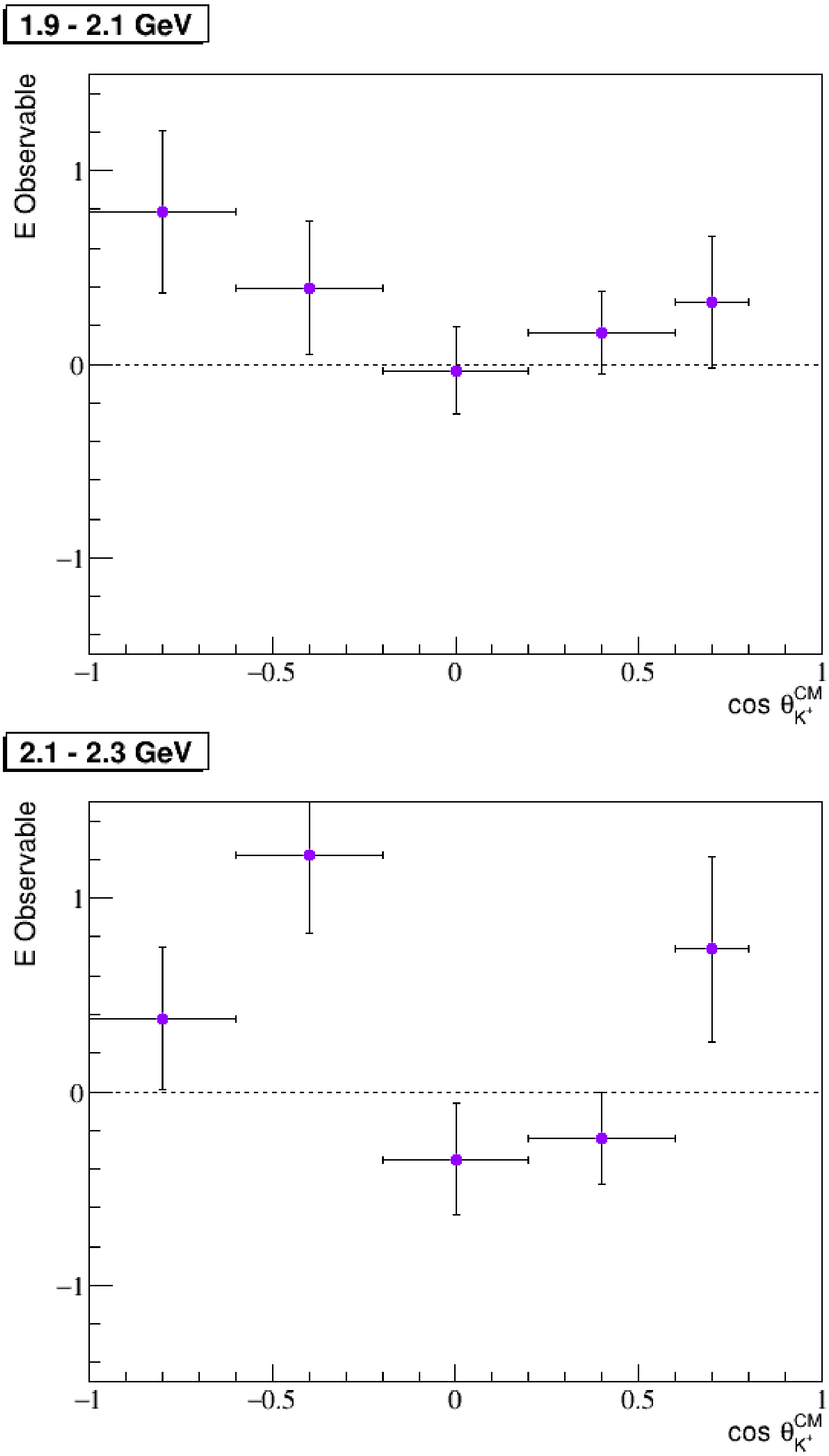

Figure 4.17: Results for the $\mathbb{E}$ double-polarisation observable using the target subtraction method; 1.9-2.1 GeV (upper), 2.1-2.3 GeV (lower).

4.2.3.3 Comparison of Empty Target Methods

It is important that the two empty target methods are shown to be consistent. To that end the differences in the value of $\mathbb{E}$ for the dilution and subtraction methods are shown in Figures 4.18 - 4.21. These are fitted with a 0^{th} order polynomial, the fit values of which are presented in Table 4.4.

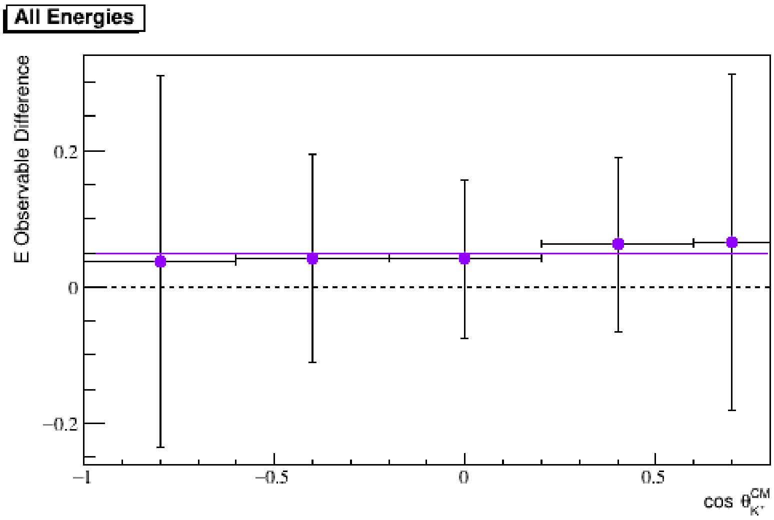

Figure 4.18: Difference in $\mathbb{E}$ for both target methods: *All energies* (1.1-2.3 GeV).

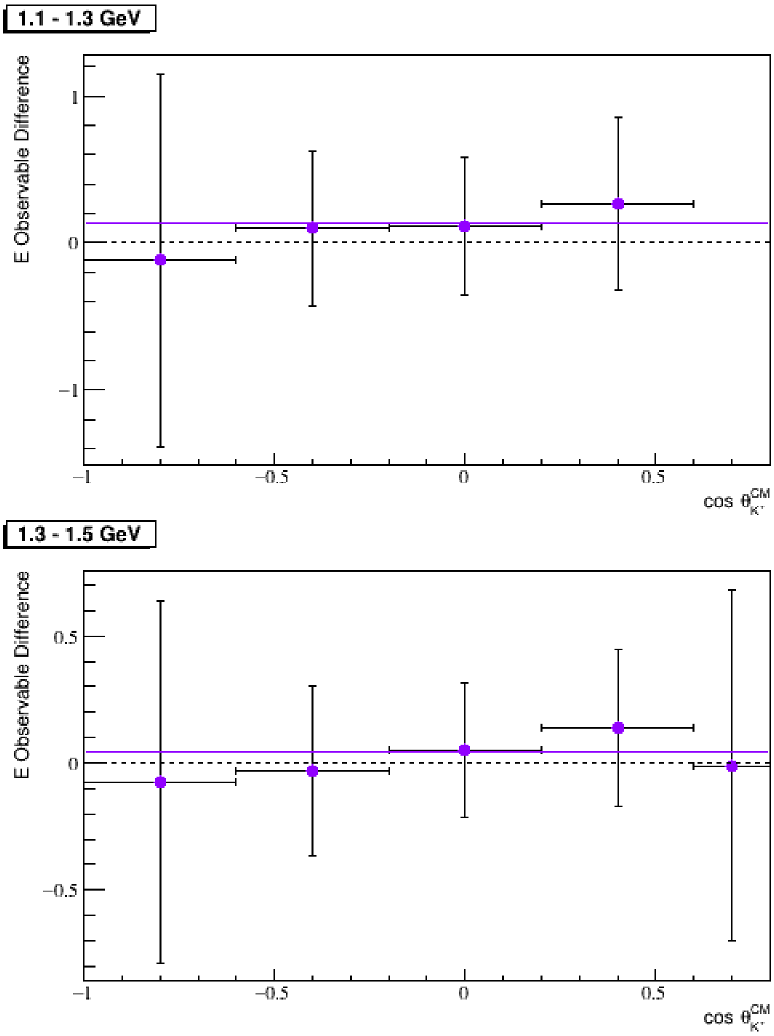

Figure 4.19: Difference in $\mathbb{E}$ for both target methods; 1.1-1.3 GeV (upper), 1.3-1.5 GeV (lower).

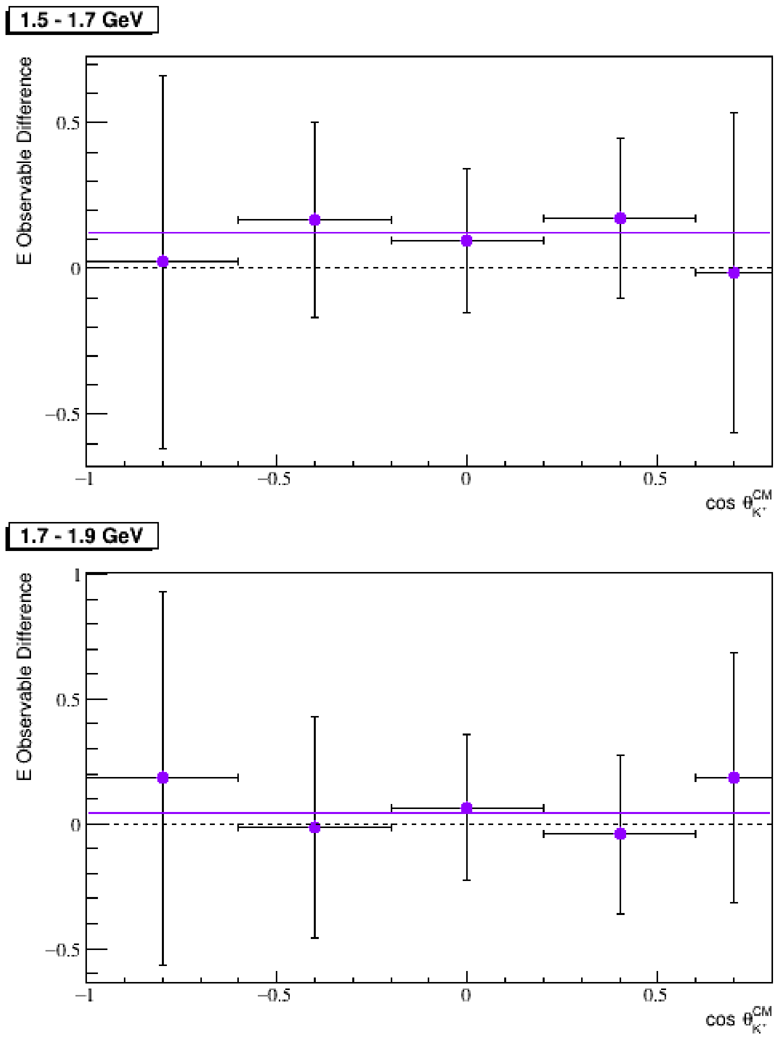

Figure 4.20: Difference in $\mathbb{E}$ for both target methods; 1.5-1.7 GeV (upper), 1.7-1.9 GeV (lower).

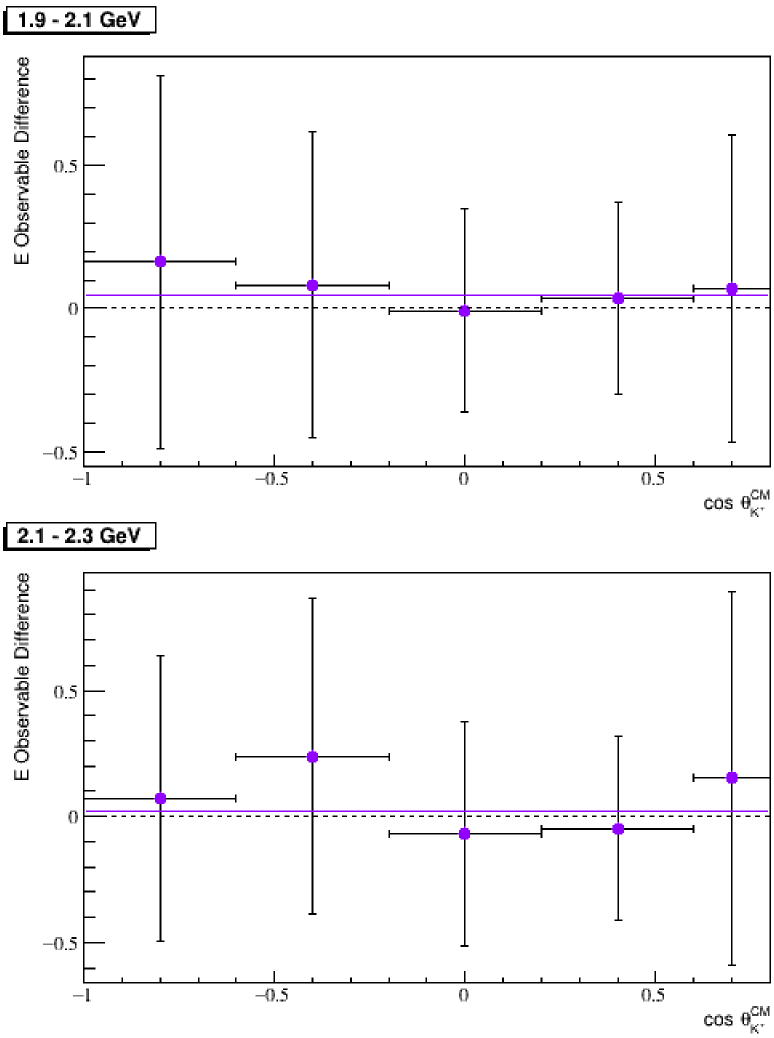

Figure 4.21: Difference in $\mathbb{E}$ for both target methods; 1.9-2.1 GeV (upper), 2.1-2.3 GeV (lower).

The two target methods are consistent within statistics, as should be expected. The low value of the chi^2/dof is a reminder that these datasets are highly correlated and as such the error bars are excessively large. These results indicate that the HD target used in this experiment is indeed a relatively clean target where the empty target subtraction method is valid.

E_γ Bin (GeV)	Fit value	Fit Error	χ^2/dof
All Energies	0.05	0.07	0.02
1.1-1.3	0.13	0.29	0.10
1.3-1.5	0.05	0.16	0.18
1.5-1.7	0.12	0.15	0.15
1.7-1.9	0.04	0.18	0.20
1.9-2.1	0.05	0.19	0.06
2.1-2.3	0.02	0.22	0.24

Table 4.4: Summary of the differences in the target methods, using a 0^{th} degree polynomial fit.

4.3 Systematic Effects in the Extraction of an Asymmetry

This section presents results from investigations into potential systematics in the extraction of the asymmetry, $\mathcal{A}$, arising from detector acceptance effects. The extracted value for the asymmetry should not show any dependence on the azimuthal angle of the reaction products. This lack of dependence on ϕ was checked using the final state kaon in the analysis presented below.

The initial step is to plot the polarisation observable $\mathbb{E}$ versus ϕ of the kaon, Figures 4.22 - 4.25. This allows the value of $\mathcal{A}_\phi$ to be compared to the double-polarisation observable $\mathbb{E}$ [2]. This comes from rearranging Equation 1.6 into:

$$\mathcal{A}_\phi = P_\gamma P_\oplus \mathbb{E}. \tag{4.11}$$

[2] Note that the region $\phi = 0 - 30°$ have been shifted to $360 - 390°$ so that no sectors are split while plotting.

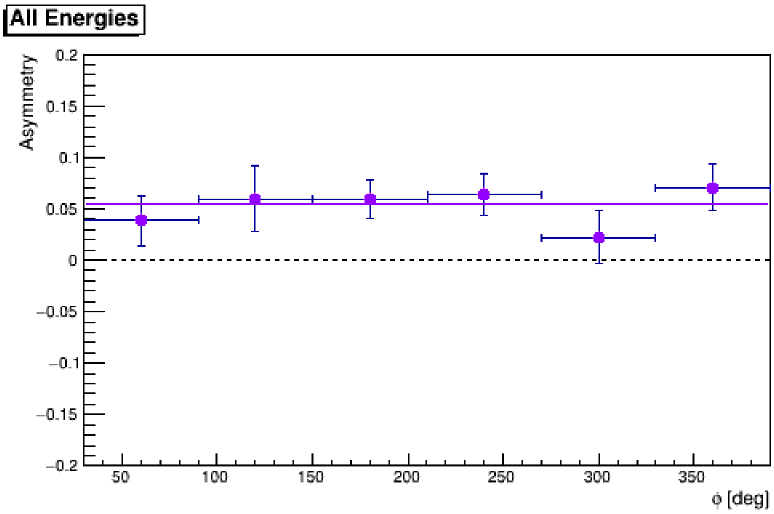

Figure 4.22: $\mathbb{E}$ double-polarisation observable in terms of the azimuthal angle ϕ: *all energies* (1.1-2.3 GeV).

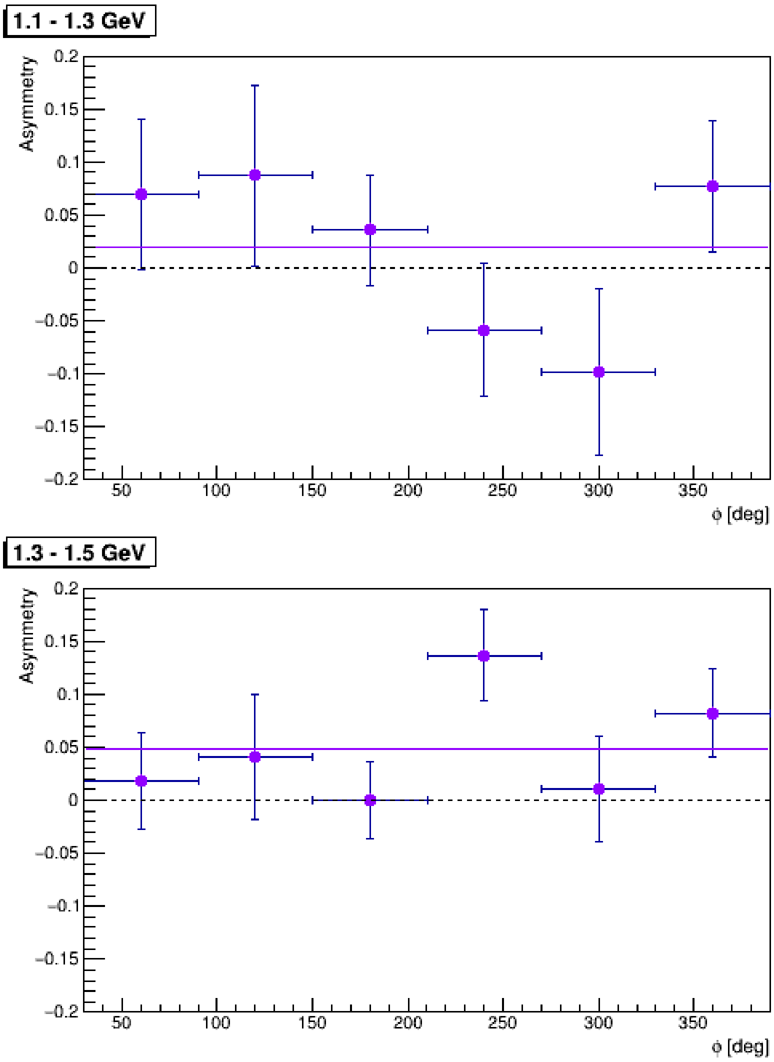

Figure 4.23: $\mathbb{E}$ double-polarisation observable in terms of the azimuthal angle ϕ: 1.1-1.3 GeV (upper), 1.3-1.5 GeV (lower).

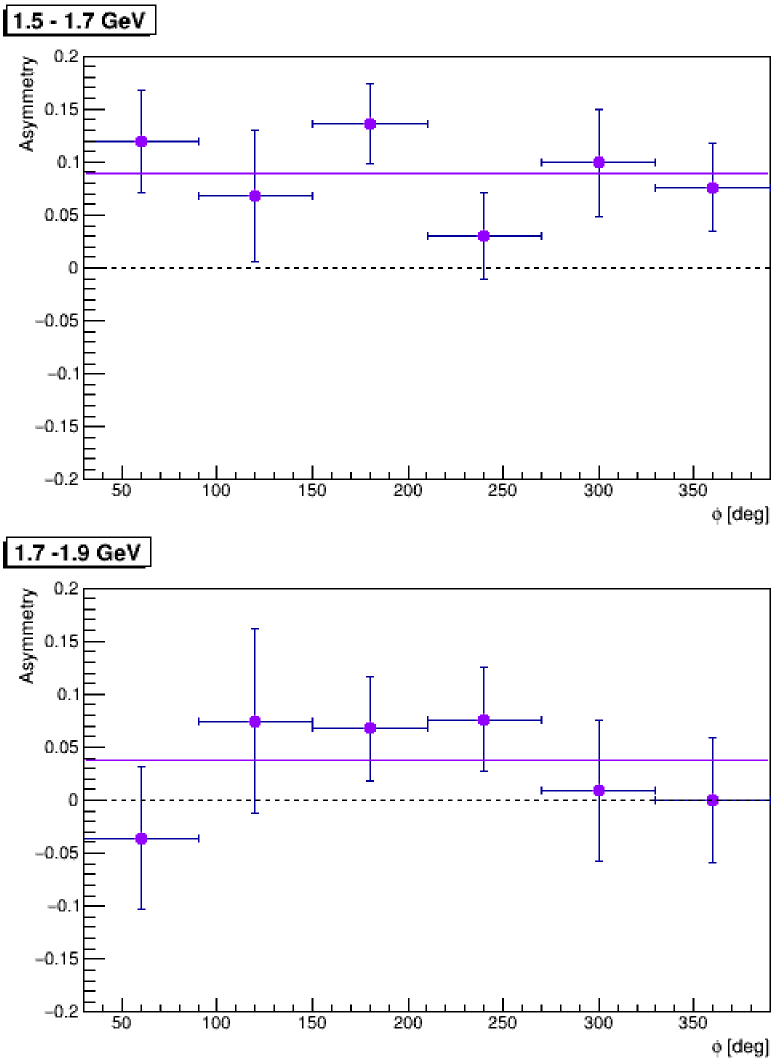

Figure 4.24: $\mathbb{E}$ double-polarisation observable in terms of the azimuthal angle ϕ: 1.5-1.7 GeV (upper), 1.7-1.9 GeV (lower).

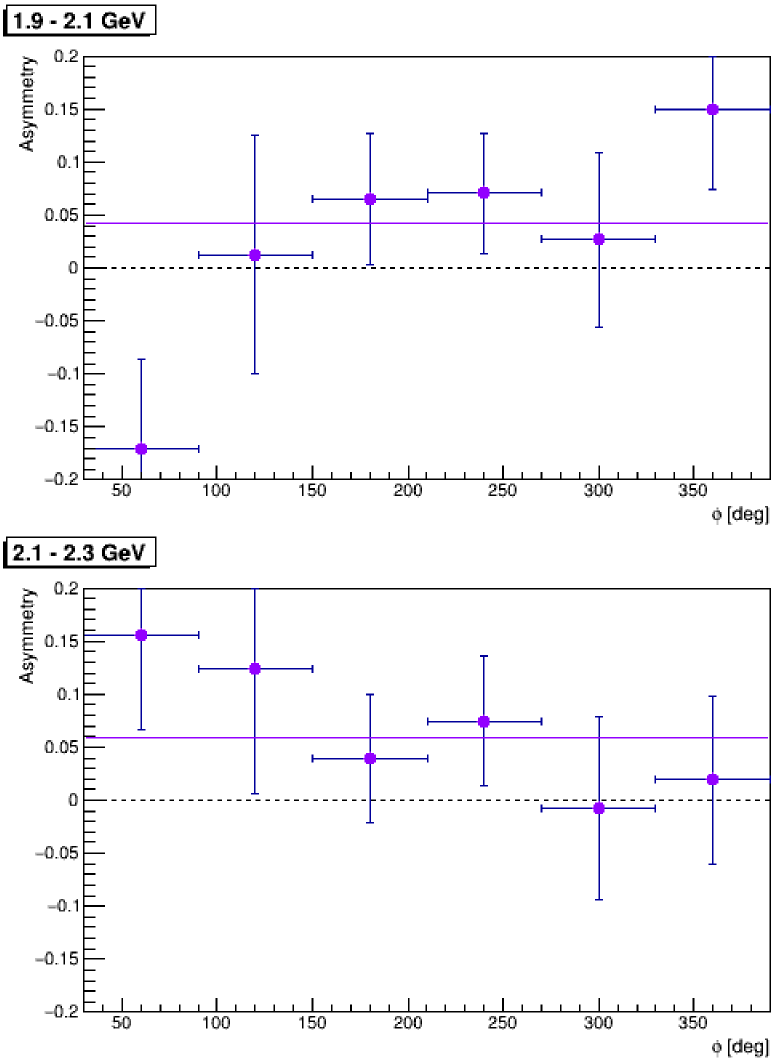

Figure 4.25: $\mathbb{E}$ double-polarisation observable in terms of the azimuthal angle ϕ: 1.9-2.1 GeV (upper), 2.1-2.3 GeV (lower).

A fit was made with a zero degree polynomial, the results of which are shown in Table 4.5, giving an average value for $\mathcal{A}_\phi$ in each energy bin. The average value for $\mathbb{E}$ was calculated from this and could be compared to the values of the asymmetry $\mathcal{A}$, calculated for $\cos\theta_{K^+}^{CM}$.

These results indicate that the calculated value of $\mathbb{E}$ in terms of ϕ is statistically consistent with the average value seen in terms of $\cos\theta_{K^+}^{CM}$. This is shown in all E_γ bins and integrated over all kaon angles. A study was also performed in order to see how the way in which the ϕ acceptance is modelled

E_γ Bin (GeV)	$\mathcal{A}_\phi$ fit	Calculated $\mathbb{E}$	Fitted $\mathbb{E}$ ($\cos\theta^{CM}_{K^+}$)	Fit Error	χ^2/dof
1.1-2.3	0.054	0.30	0.29	0.01	0.56
1.1-1.3	0.020	0.11	0.13	0.19	1.17
1.3-1.5	0.048	0.26	0.29	0.10	1.43
1.5-1.7	0.089	0.48	0.48	0.10	0.86
1.7-1.9	0.038	0.21	0.18	0.12	0.59
1.9-2.1	0.042	0.23	0.19	0.14	1.47
2.1-2.3	0.059	0.33	0.26	0.14	0.50

Table 4.5: Summary of the $\mathbb{E}$ double-polarisation observable, as calculated in terms of ϕ. This can be compared with the average value of the $\mathbb{E}$ observable plotted with $\cos\theta^{CM}_{K^+}$.

influences the results of the observable $\mathbb{E}$.

4.3.1 Effect of ϕ Acceptance

Further studies of any potential ϕ dependent systematics were explored using simulated pseudo-data. Events were generated using an event generator with a fixed value for $\mathbb{E}$. These data were then passed through the data analysis code used for the real data. Different conditions were placed on this pseudo-data sample to explore possible systematic effect. These were assessed by comparison of the extracted value of $\mathbb{E}$ from the data. Three scenarios were considered for this study:

- Uniform acceptance in ϕ.
- Removing fiducial regions in CLAS, which limit the ϕ acceptance of the final state particles.
- Realistic cosine function (mimicking some realistic CLAS acceptance)[3].

Each time the generator was run, plots were made of $\mathbb{E}$ vs ϕ for each scenario. These plots were then fitted with a zero degree polynomial and compared to the

[3]This function was obtained from Nicholas Zachariou.

'true' value of $\mathbb{E}$ given to the generator (taken as +0.7 for these studies). As well as investigating the acceptance effects described above in extracting $\mathbb{E}$, two different methods were explored:

1. Using the histograms for the asymmetry method.

2. Using bins for the asymmetry method then performing a *pol*0 fit of the observable in ϕ.

An example of the results obtained from one run is given in Figure 4.26 with fitted values given in Table 4.6. where the value of $\mathbb{E}$ is shown for all three acceptance scenarios. It should be noted that this only indicated one trial, so there will be some natural deviation from the *true* value of $\mathbb{E}$.

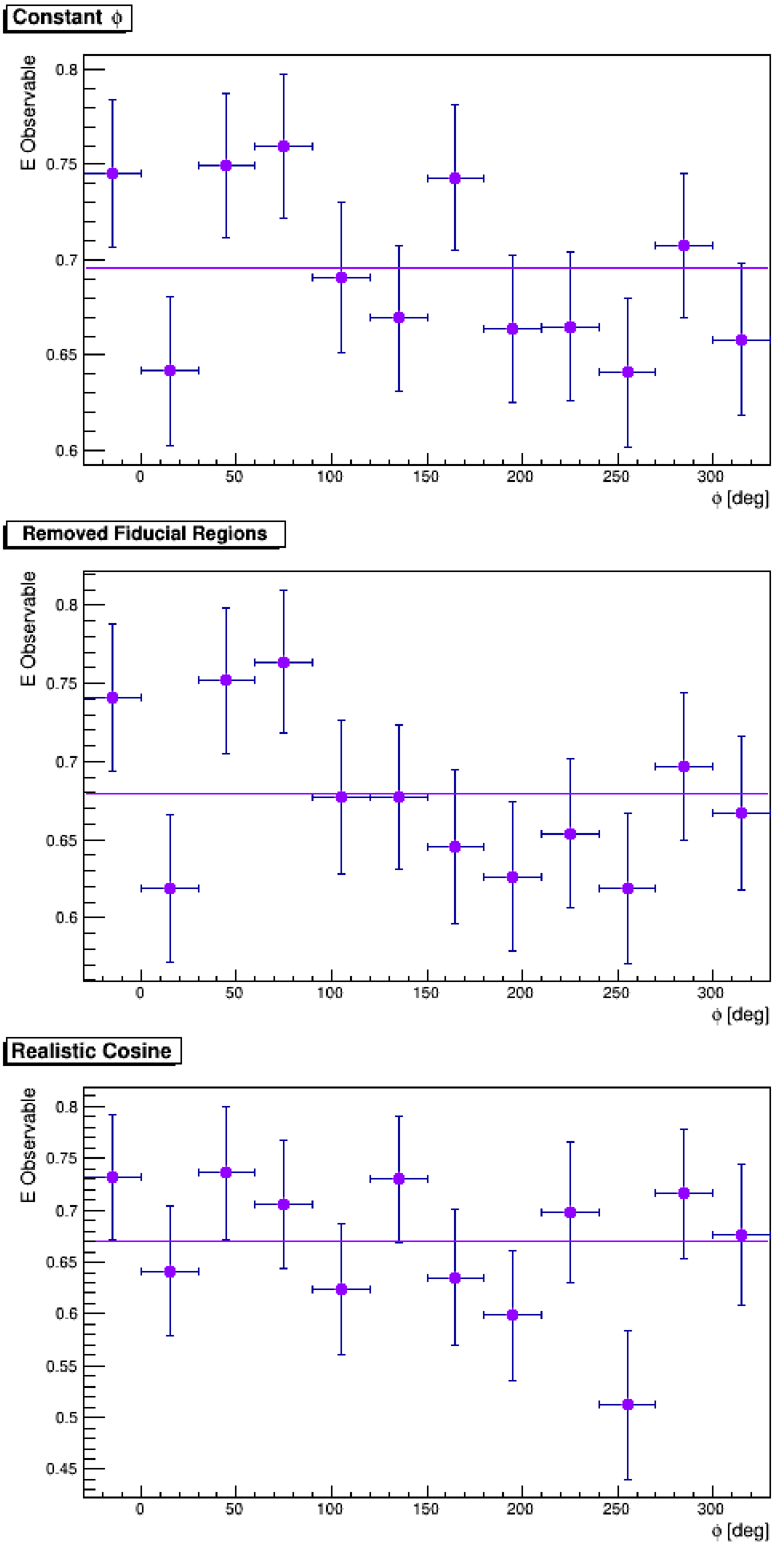

Figure 4.26: An event generator is used to compare the results of three acceptances to a given *true* value of the double-polarisation observable $\mathbb{E}$ (0.7). This shows the results for one trial.

Acceptance	Fit Value	Fit Error	χ^2/dof
Constant	0.695	0.011	1.30
Fiducial Regions	0.680	0.014	1.17
Realistic CLAS Acceptance	0.670	0.018	1.02

Table 4.6: Summary of produced values of $\mathbb{E}$ for the three acceptances. The *true* value of $\mathbb{E}$ given to the generator was 0.7.

Many trials are carried out in order to account for any statistical deviation and in aid of obtaining a more accurate estimate of the observable $\mathbb{E}$. The *true* value, was fixed for the study, so that any deviations coming from the ϕ acceptance or extraction method could be easily identified.

A detailed run was performed where 5000 trials, in each of which $25K$ events were produced. The results from these trials are plotted to give a Gaussian distribution which is then fitted. Results from these trials are presented in Figures 4.27 and 4.28, using the ratio and fit methods respectively.

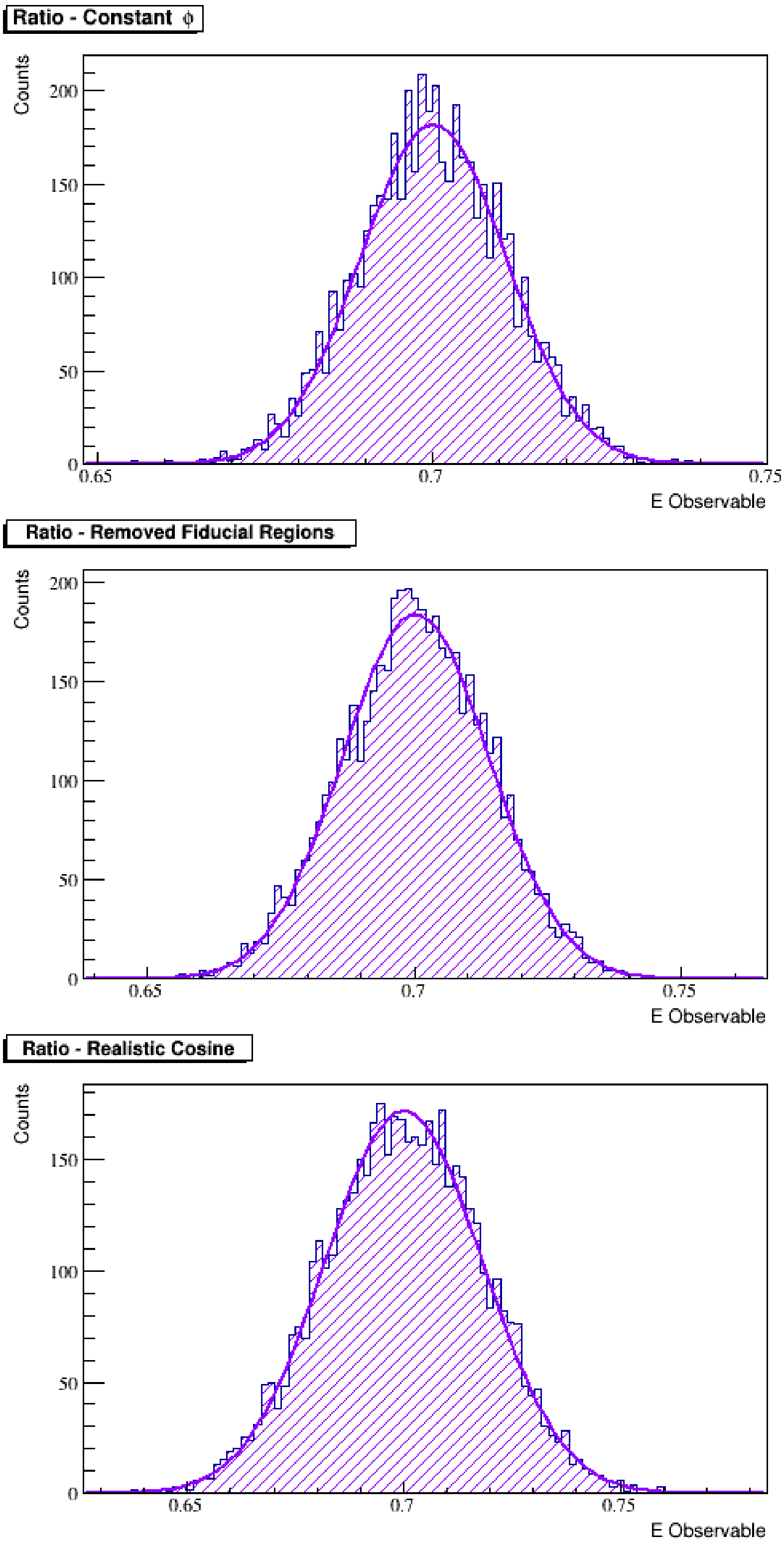

Figure 4.27: Collated results for 5000 generated trials, with the value of the $\mathbb{E}$ observable calculated using the ratio method.

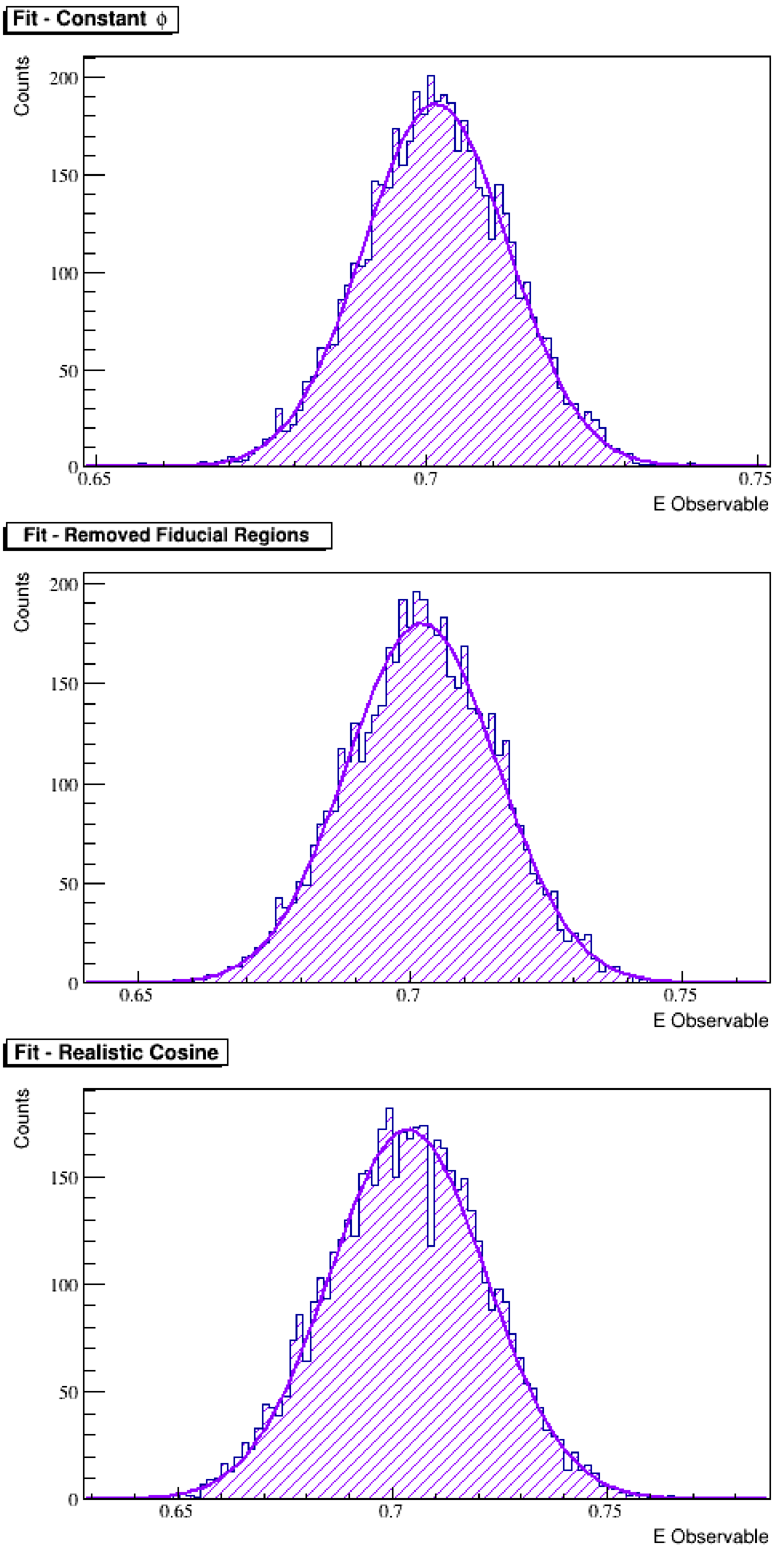

Figure 4.28: Collated results for 5000 generated trials, with the value of the $\mathbb{E}$ observable calculated using the fitting method.

As expected from these, we see that there is a clear distribution forming around the *true* value of 0.7. This is shown for both methods of calculating the polarisation observable, note that these methods are only comparable because we have chosen for $\mathbb{E}$ to be a constant, rather than having a dependence in energy or ϕ. The results of fitting these two methods are presented in Tables 4.7 and 4.8.

Acceptance	Fit Mean	Fit σ
Constant	0.7	0.011
Fiducial Regions	0.7	0.014
Realistic CLAS Acceptance	0.7	0.018

Table 4.7: Summary of produced values of $\mathbb{E}$ for the three acceptances over 5000 trials. The value of $\mathbb{E}$ was calculated using the ratio method.

Acceptance	Fit Mean	Fit σ
Constant	0.7	0.011
Fiducial Regions	0.7	0.014
Realistic CLAS Acceptance	0.7	0.18

Table 4.8: Summary of produced values of $\mathbb{E}$ for the three acceptances over 5000 trials. The value of $\mathbb{E}$ was calculated using the fitting method.

These show that for both methods and all acceptances that the obtained values for $\mathbb{E}$ are consistent with the initial value given to the generator within 1σ. This illustrates that there is no effect of the ϕ acceptance on the construction of the $\mathbb{E}$ observable.

4.4 Study of Dependence of Extracted $\mathbb{E}$ on Spectator Momentum

Ideally the event sample for analysis would be made using the complete final state, $K^+\pi^-n$, allowing the spectator proton (p_s) momentum to be reconstructed on an event-by-event basis; but as was shown in Section 3.2.20, isolating the exlusive $K^+\pi^-n$ final state lowers the statistics by a factor of ~ 20. A study to constrain any dependencies of $\mathbb{E}$ on the spectator proton momentum was carried out as described below.

The kinetic energy of the K^+ can be calculated from the kinematics of the two-body reaction, allowing the comparison of the measured and calculated values of kinetic energy. By considering the difference, ΔT_{K^+}, the quasi-free events can be emphasised with an appropriate cut. Figure 4.29 highlights the separation achievable in spectator momentum by careful selection of ΔT_{K^+}

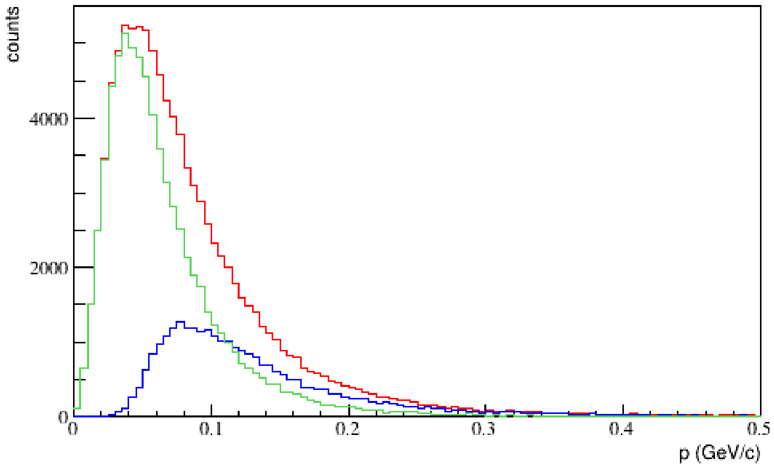

Figure 4.29: Momentum of the spectator proton; shown for all ΔT_{K^+}, for $|\Delta T_{K^+}| < 0.05\ GeV$ and for $|\Delta T_{K^+}| > 0.05\ GeV$.

It is constructive to calculate and compare the double-polarisation observable $\mathbb{E}$ with results obtained for the *nominal* selection, in order to show the effect of emphasising/suppressing the quasi-free events, Figure 4.30.

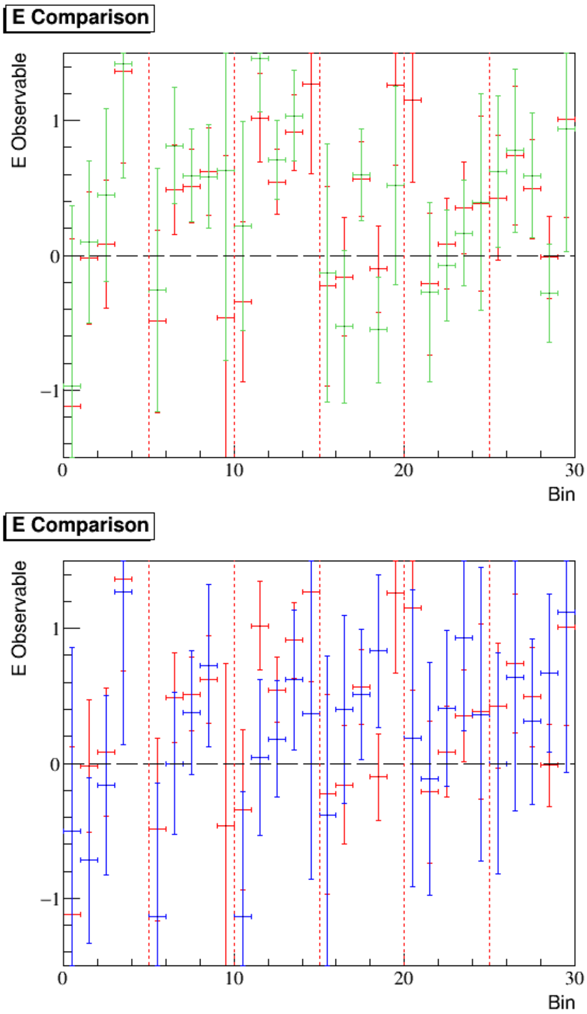

Figure 4.30: Comparisons of the calculated values of the $\mathbb{E}$ observable for the quasi-free emphesised selection cut (upper) and the quasi-free suppressed selection cut (lower) compared with the nominal selection cut for kinetic energy selection.

It can be seen from Figure 4.30 that the results for emphasising and suppressing the quasi-free contributions are consistent with the results from the *nominal* selection, with only a handful of bins falling outwith the statistical errors. Therefore, we can conclude that any benefit that would be derived by emphasising these events is far outweighed by the statistics available in this analysis. Furthermore, if we consider the results of the selections together, Figure 4.31, we see that the differences obtained are statistically consistent with zero.

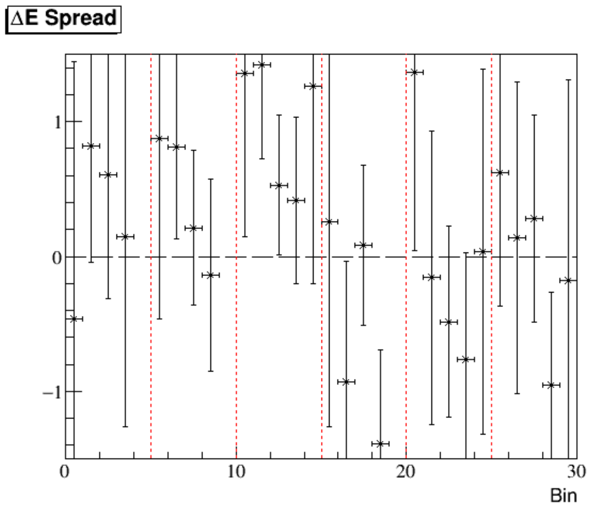

Figure 4.31: Differences in the calculated values of the $\mathbb{E}$ observable for the quasi-free emphasised and quasi-free suppressed selections of the spectator momentum.

4.5 Systematic Studies on Selection Cuts

It is important to quantify the effect of selection cuts on the extracted $\mathbb{E}$ observable. In order to study the stability of these selection cuts, all 30 bins (5 bins of $\cos\theta_{K^+}^{CM}$ within 6 bins of E_γ) were considered and the difference in the observable ($\Delta\mathbb{E}$) investigated. The cuts investigated are shown in Table 4.9.

Selection Cut	Method of Variation
Best Photon	0.5 ns Expansion/Contraction
$\Delta\beta_{K^+\pi^-}$	σ Contraction
Reconstructed Neutron	σ Expansion
K^+ Z Vertex	0.2 cm Expansion/Contraction
Fiducial Region	2° Expansion/Contraction
Σ^- Mass Window	σ Contraction
MisIdentification Removal	$2D$ Variation

Table 4.9: Summary of selection cut studies.

The difference in the observed values of $\mathbb{E}$ ($\Delta\mathbb{E}$) are considered, although it should be noted that for each value there will be both a statistical and a systematic component present. The systematics are presented as the average mean of the observable difference ($\overline{\Delta\mathbb{E}}$) as follows:

$$\sigma_{sys}(cut) = \sqrt{\frac{1}{N}\sum_{i=1}^{N}\Delta\mathbb{E}_i} \tag{4.12}$$

where N represents the total number of bins available. This method is used in order to minimise the influence of statistical fluctuations.

The following sections will discuss the nature of each of the cuts. The overall systematic effects of the cut variations are discussed in Section 4.5.8.

4.5.1 Photon Timing

The spectrum of the timing difference between the start counter and the time-of-flight scintillators was shown in Figure 3.8. To assess the stability of the $|\Delta t_{\pi^-}| < 1.5\ ns$ cut, the width is expanded and contracted by 0.5 ns, shown in Figure 4.32.

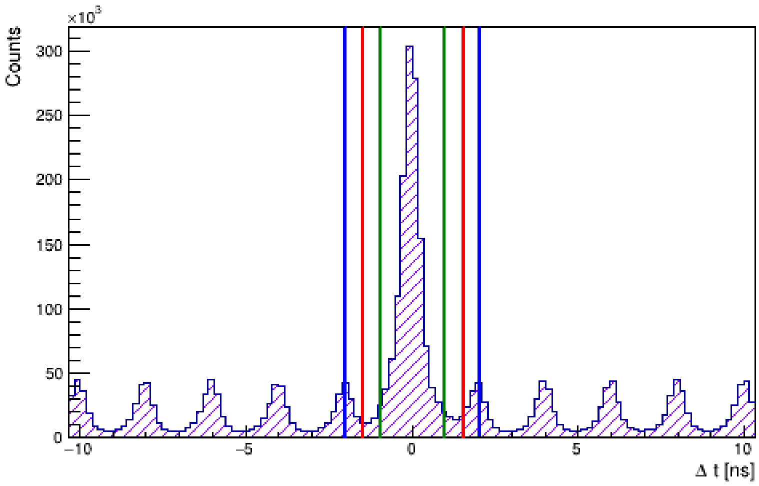

Figure 4.32: π^- timing difference using the selected best photon. The selection cuts used for the systematic studies are shown; $|\Delta t_{\pi^-}| <$ 1.0 ns, 1.5 ns, 2.0 ns.

For each of these selections, the observable $\mathbb{E}$ is calculated. The new selections for the systematic studies are compared to the *nominal* selection. These are shown together in Figure 4.33 [4]:

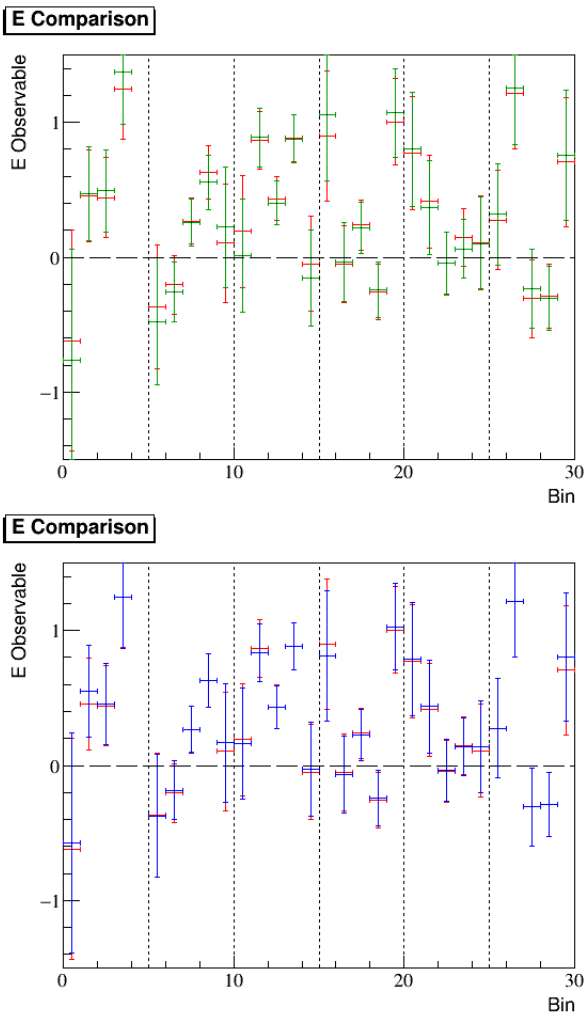

Figure 4.33: Comparisons of the calculated values of the $\mathbb{E}$ observable for the contracted selection cut (upper) and the expanded selection cut (lower) compared with the nominal selection cut for photon timing.

From Figure 4.33, we can see that the variation in the value of the $\mathbb{E}$ observable is well within the statistical errors for the data, showing that the statistical uncertainties are dominant over the systematic uncertainties. In order to limit the effect of this, the difference in $\mathbb{E}$ is considered and averaged over all energy bins in order to minimise the influence of statistical fluctuations, however this should

[4] Within these plots, all bins in E_γ and $\cos\theta_{K^+}^{CM}$ are shown with each 200 MeV energy bins separated by the dashed lines.

still be considered as an upper limit of the systematic error. The differences in the observable $\mathbb{E}$ are shown in Figure 4.34 [5].

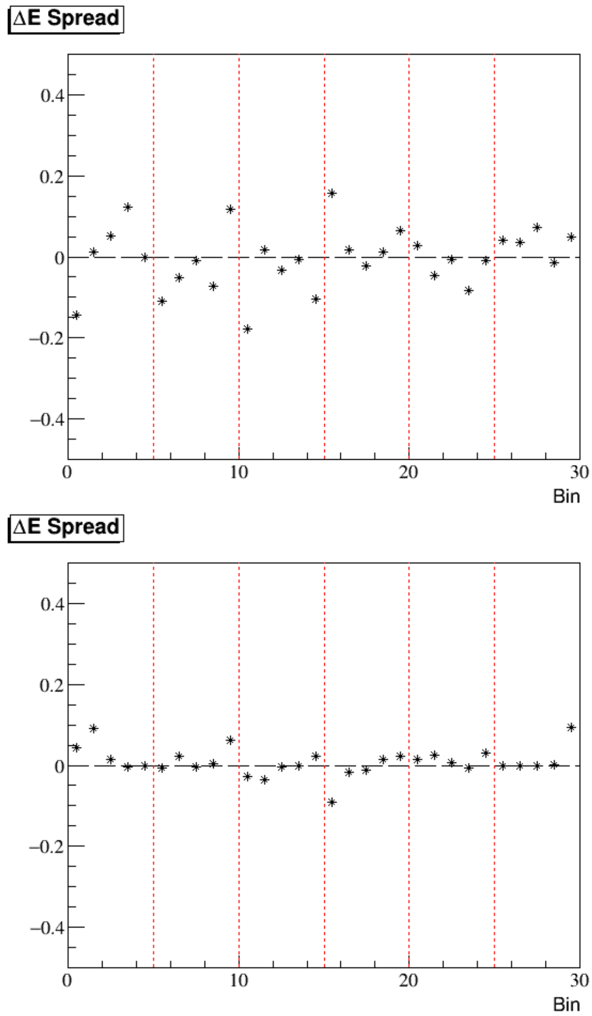

Figure 4.34: Differences in the calculated values of the $\mathbb{E}$ observable for the contracted selection cut (upper) and the expanded selection cut (lower) from the nominal selection cut for photon timing.

From Figure 4.34, we can see that there seems to be no obvious E_γ or $\cos\theta^{CM}_{K^+}$ dependence on the values of $\Delta\mathbb{E}$. The average values obtained are presented in Table 4.10.

[5] Within these plots, all bins in E_γ and $\cos\theta^{CM}_{K^+}$ are shown with each 200 MeV energy bins separated by the dashed lines. Error bars are not shown on this plot because the values of $\mathbb{E}$ are not truly independent as they are formed from non-exclusive subsets of the same dataset.

Selection Cut	Average $\Delta\mathbb{E}$
Contracted Timing	-0.0031
Expanded Timing	0.0097

Table 4.10: Summary of the average $\Delta\mathbb{E}$ values obtained for the best photon timing cut.

As stated before, the systematics shown here realistically represent an upper estimate. As such, the larger of these are chosen to represent the systematic uncertainty inherent in the best photon timing cut.

4.5.2 $\Delta\beta_{K^+\pi^-}$

The distributions of momentum vs $\Delta\beta$ for both K^+ and π^- candidates, after data corrections, were shown in Figure 3.11. To assess the stability of the $|\Delta\beta_{K^+\pi^-}| < 0.036$ cut, this is contracted from 3σ to 2σ. The K^+ and π^- selections are now split into two subsections.

4.5.2.1 $\Delta\beta_{K^+}$

The selections for the systematic study of the $\Delta\beta_{K^+}$ are shown in Figure 4.35.

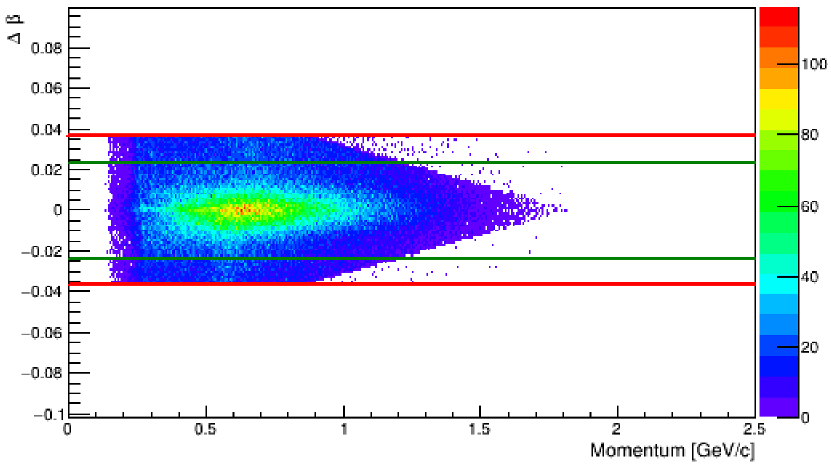

Figure 4.35: Momentum vs $\Delta\beta_{corrected}$ distribution for K^+ candidates. The selection cuts used for the systematic studies are shown; $|\Delta\beta_{K^+}| < 0.024\ (2\sigma)$, $0.036\ (3\sigma)$.

For the contracted selection, the observable $\mathbb{E}$ is calculated and compared with the nominal. These are shown together in Figure 4.36. Once again we can see that the variation in the value of the $\mathbb{E}$ observable is well within the statistical errors for the data, showing that the statistical uncertainties are dominant over the systematic uncertainties. The differences in the observable $\mathbb{E}$ are shown in Figure 4.37.

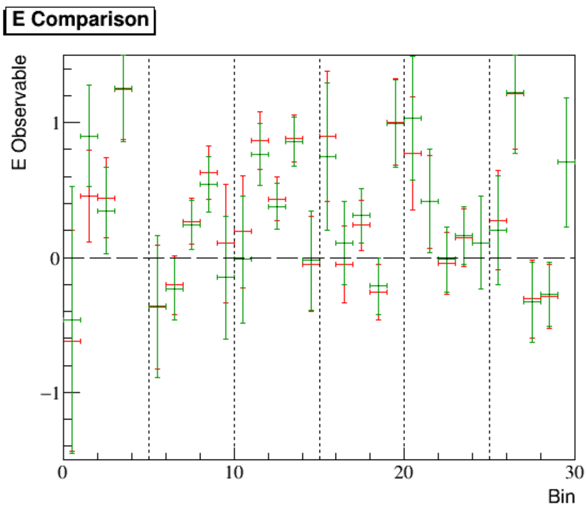

Figure 4.36: Comparison of the calculated values of the $\mathbb{E}$ observable for the contracted (2σ) selection cut compared with the nominal (3σ) selection cut for $\Delta\beta_{K^+}$.

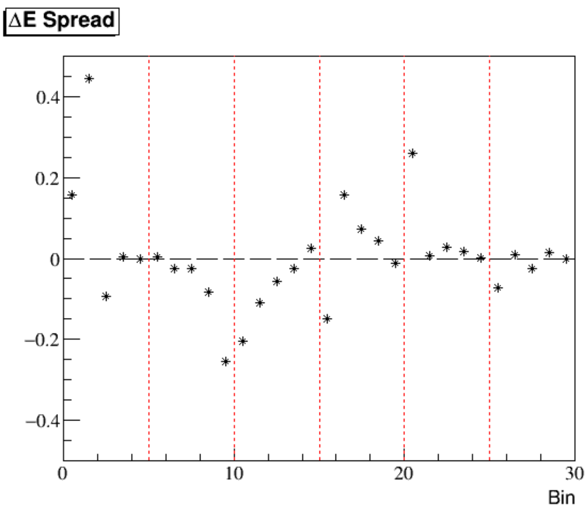

Figure 4.37: Differences in the calculated values of the $\mathbb{E}$ observable for the contracted selection cut from the nominal selection cut for $\Delta\beta_{K^+}$.

From Figure 4.37, we can again see that there seems to be no obvious E_γ or $\cos\theta_{K^+}^{CM}$ dependence on the values of $\Delta\mathbb{E}$. The average value obtained is presented in Table 4.11.

Selection Cut	Average $\Delta\mathbb{E}$
Contracted $\Delta\beta$ for K^+	0.0076

Table 4.11: The average $\Delta\mathbb{E}$ value obtained for the $\Delta\beta_{K^+}$ cut.

4.5.2.2 $\Delta\beta_{\pi^-}$

The selections for the systematic study of the $\Delta\beta_{\pi^-}$ are shown in Figure 4.38.

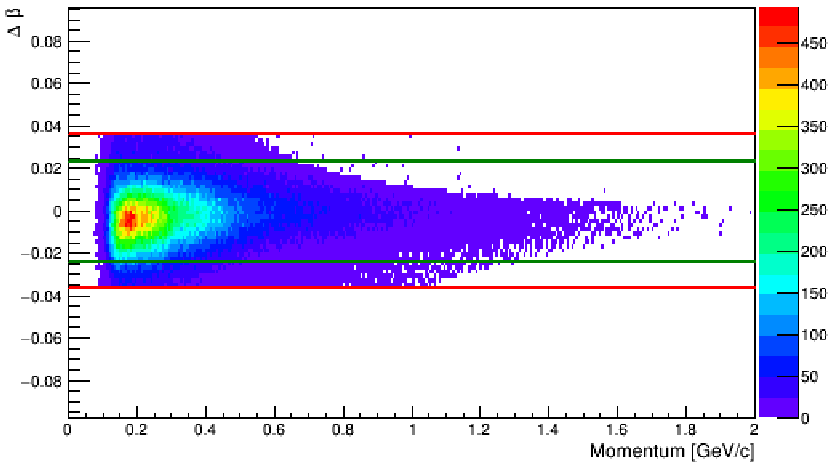

Figure 4.38: Momentum vs $\Delta\beta_{corrected}$ distribution for π^- candidates. The selection cuts used for the systematic studies are shown; $|\Delta\beta_{\pi^-}| < 0.024$ (2σ), 0.036 (3σ).

For the contracted selection, the observable $\mathbb{E}$ is calculated and compared with the nominal. These are shown together in Figure 4.39. Once again we can see that the variation in the value of the $\mathbb{E}$ observable is well within the statistical errors for the data, showing that the statistical uncertainties are dominant over the systematic uncertainties. The differences in the observable $\mathbb{E}$ are shown in Figure 4.40.

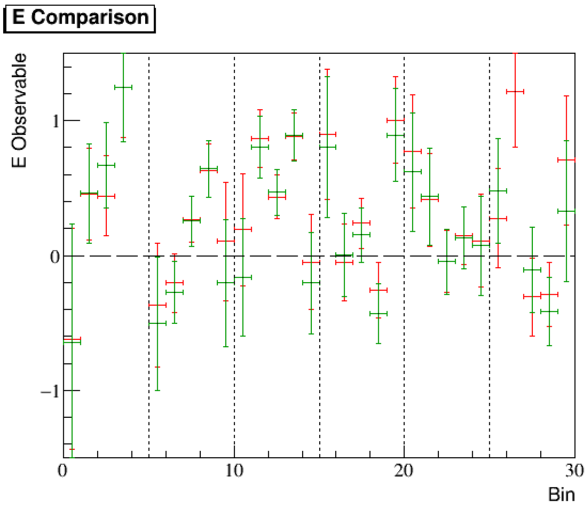

Figure 4.39: Comparison of the calculated values of the $\mathbb{E}$ observable for the contracted (2σ) selection cut compared with the nominal (3σ) selection cut for $\Delta\beta_{\pi^-}$.

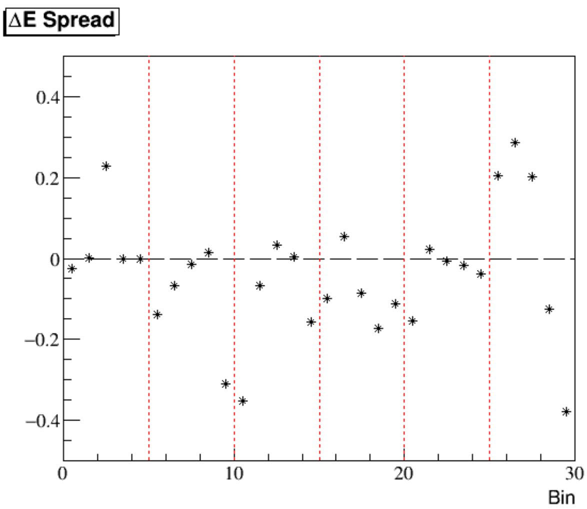

Figure 4.40: Differences in the calculated values of the $\mathbb{E}$ observable for the contracted selection cut from the nominal selection cut for $\Delta\beta_{\pi^-}$.

From Figure 4.40, we can again see that there seems to be no obvious E_γ or $\cos\theta_{K^+}^{CM}$ dependence on the values of $\Delta\mathbb{E}$. The average value obtained is presented in Table 4.12.

Selection Cut	Average $\Delta\mathbb{E}$
Contracted $\Delta\beta$ for π^-	-0.041

Table 4.12: The average $\Delta\mathbb{E}$ value obtained for the $\Delta\beta_{\pi^-}$ cut.

4.5.3 Reconstructed Neutron

The selections for the systematic study of the reconstructed neutron mass ($MM(K^+\pi^-)$) are shown in Figure 4.41.

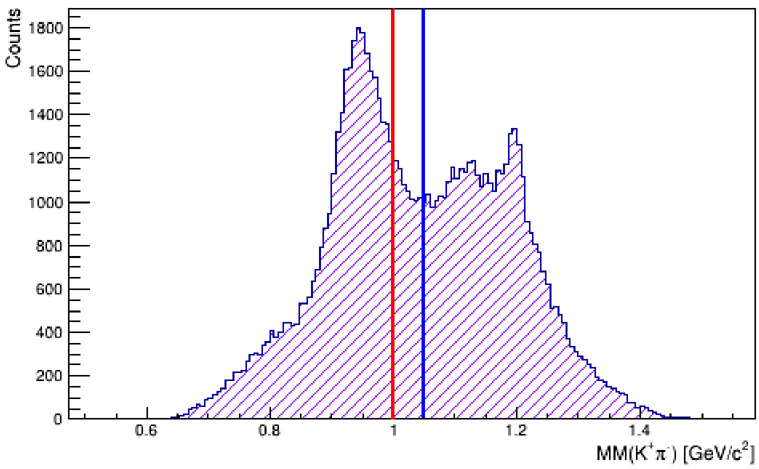

Figure 4.41: Reconstructed neutron using the missing mass technique. The selection cuts used for the systematic studies are shown; $MM(K^+\pi^-) < 1.0$ GeV/c^2 (1σ), 1.05 GeV/c^2 (2σ).

For the expanded selection, the observable $\mathbb{E}$ is calculated and compared to the nominal. These are shown together in Figure 4.42. Once again we can see that the variation in the value of the $\mathbb{E}$ observable is well within the statistical errors for the data. The differences in the observable $\mathbb{E}$ are shown in Figure 4.43.

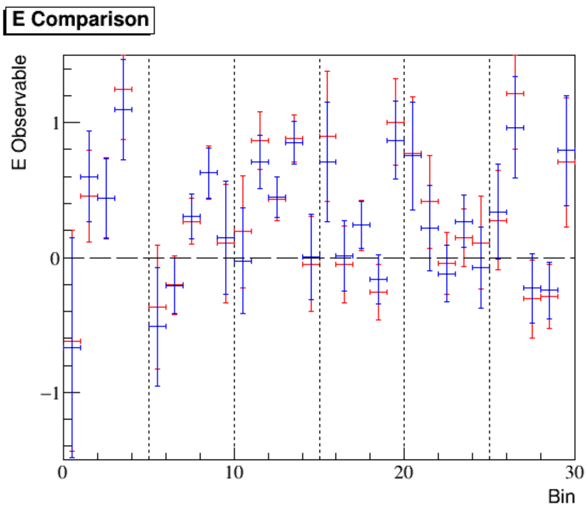

Figure 4.42: Comparison of the calculated values of the $\mathbb{E}$ observable for the expanded (2σ) selection cut compared with the nominal (1σ) selection cut for the reconstructed neutron.

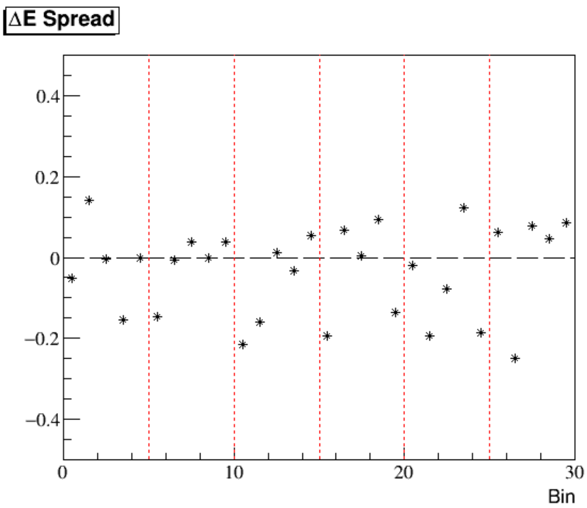

Figure 4.43: Differences in the calculated values of the $\mathbb{E}$ observable for the expanded selection cut from the nominal selection cut for the reconstructed neutron.

From Figure 4.43, we can again see that there seems to be no obvious E_γ or $\cos\theta_{K^+}^{CM}$ dependence on the values of $\Delta\mathbb{E}$. The average value obtained is presented in Table 4.13.

Selection Cut	Average $\Delta\mathbb{E}$
Expanded $MM(K^+\pi^-)$	-0.0337

Table 4.13: The average $\Delta\mathbb{E}$ value obtained for the $MM(K^+\pi^-)$ cut.

4.5.4 Z-Vertex

The spectrum of the kaon z-vertex from the centre of CLAS was shown in Figure 3.27. To assess the stability of the $(-10.5) < Z^{K^+}_{vert} < (-5.5)$ cm cut, the width is expanded and contracted by 0.2 cm, shown in Figure 4.44.

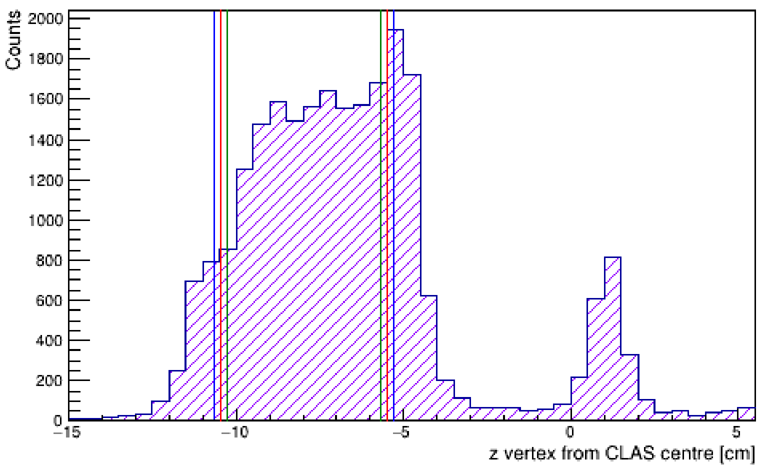

Figure 4.44: K^+ z-vertex from the centre of CLAS. The selection cuts used for the systematic studies are shown; $Z^{K^+}_{vert}$ $[-10.3, -5.7]$ cm, $[-10.5, -5.5]$ cm, $[-10.7, -5.3]$ cm.

For each of these selections, the observable $\mathbb{E}$ is calculated. The new selections for the systematic studies are compared to the *nominal* selection, which are shown together in Figure 4.45.

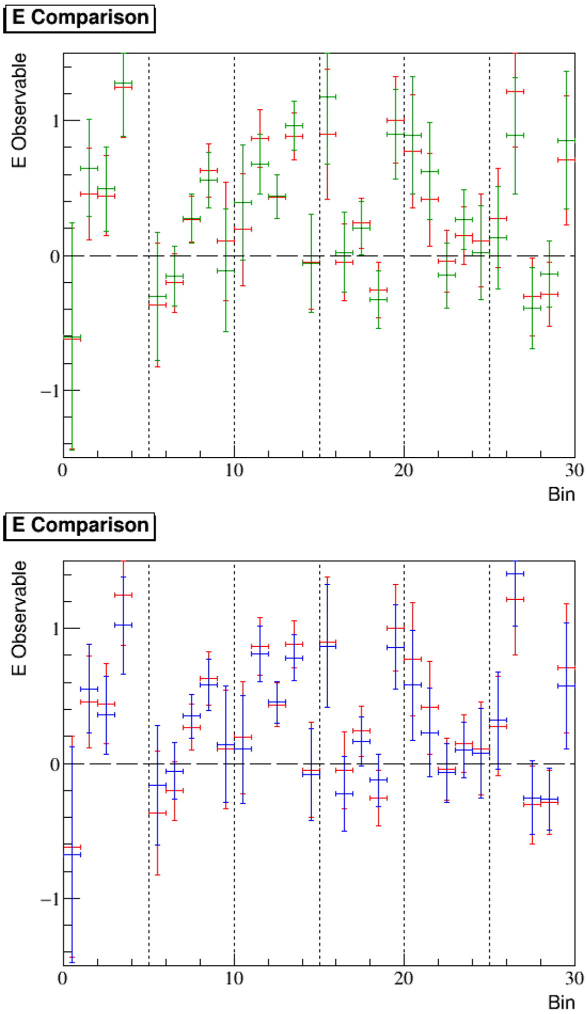

Figure 4.45: Comparisons of the calculated values of the $\mathbb{E}$ observable for the contracted selection cut (upper) and the expanded selection cut (lower) compared with the nominal selection cut for the z-vertex of the K^+.

From Figure 4.45, we can see that the variation in the value of the $\mathbb{E}$ observable is well within the statistical errors for the data, The differences in the observable $\mathbb{E}$ are shown in Figure 4.46.

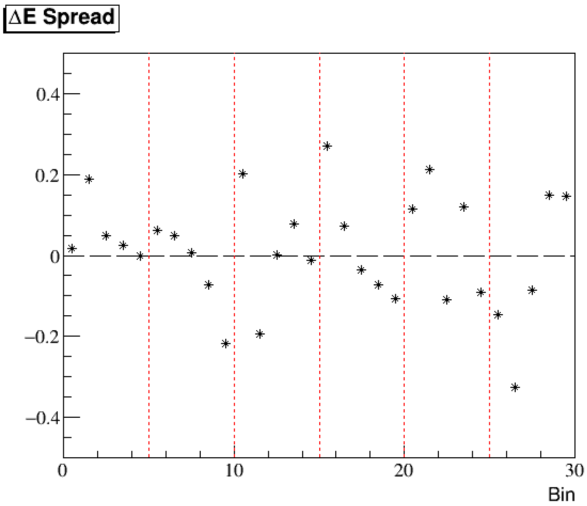

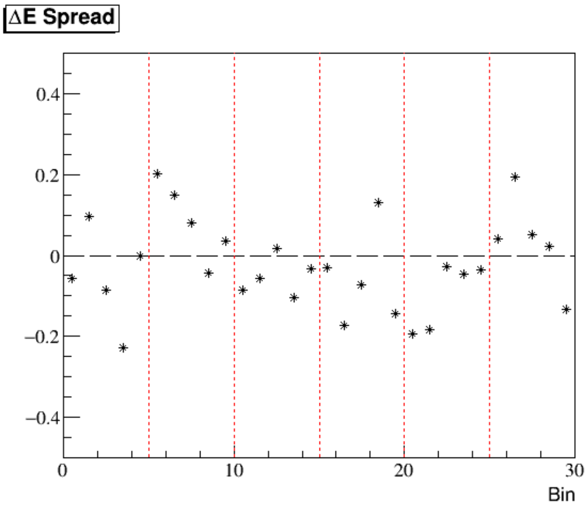

Figure 4.46: Differences in the calculated values of the $\mathbb{E}$ observable for the contracted selection cut (upper) and the expanded selection cut (lower) from the nominal selection cut for the z-vertex of the K^+.

From Figure 4.46, we can see that there seems to be no obvious E_γ or $\cos\theta^{CM}_{K^+}$ dependence on the values of $\Delta\mathbb{E}$. The average values obtained are presented in Table 4.14.

As stated before, the systematics shown here realistically represent an upper estimate. As such, the larger of these are chosen to represent the systematic uncertainty inherent in the z-vertex cut.

Selection Cut	Average $\Delta\mathbb{E}$
Contracted Z-vertex	0.0122
Expanded Z-vertex	-0.0261

Table 4.14: Summary of the average $\Delta\mathbb{E}$ values obtained for the z-vertex cut.

4.5.5 Fiducial Cuts

The spectrum of the polar and azimuthal angles of the K^+ were shown in Figure 3.30. To assess the stability of the fiducial region cut ($\pm 5°$), the width is expanded and contracted by $2°$, shown in Figure 4.47.

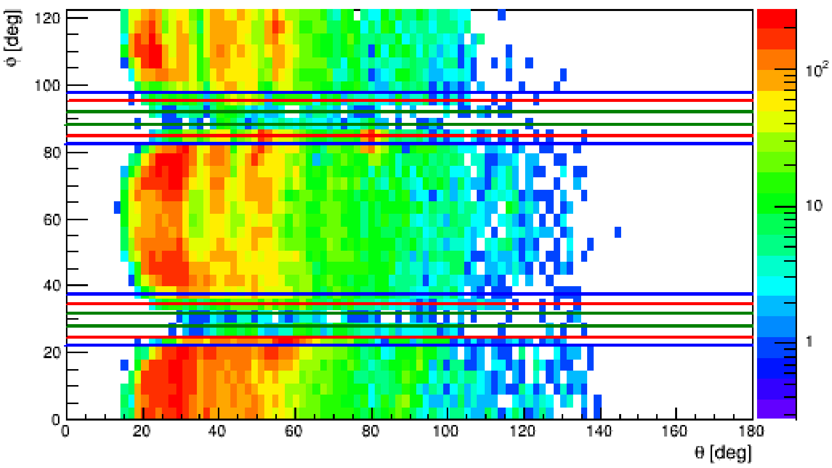

Figure 4.47: K^+ polar vs azimuthal angles (log scale). The selection cuts used for the systematic studies are shown; $|\phi_{K^+}| < \pm 3°$, $\pm 5°$, $\pm 7°$.

For each of these selections, the observable $\mathbb{E}$ is calculated. The new selections for the systematic studies are compared to the *nominal* selection. These are shown together in Figure 4.48.

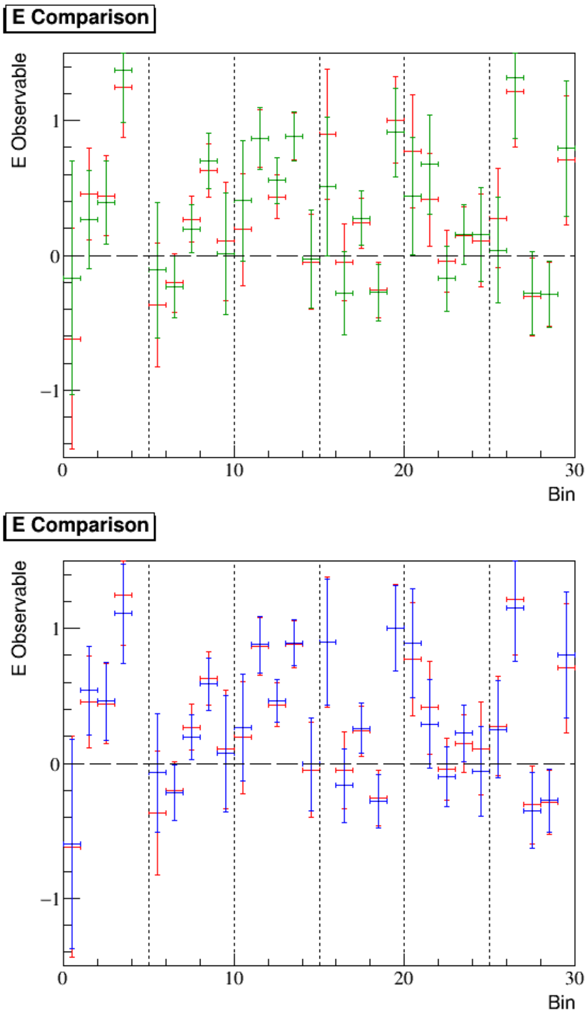

Figure 4.48: Comparisons of the calculated values of the $\mathbb{E}$ observable for the contracted selection cut (upper) and the expanded selection cut (lower) compared with the nominal selection cut for the fiducial regions.

From Figure 4.48, we can see that the variation in the value of the $\mathbb{E}$ observable is again well within the statistical errors for the data. The differences in the observable $\mathbb{E}$ are shown in Figure 4.49.

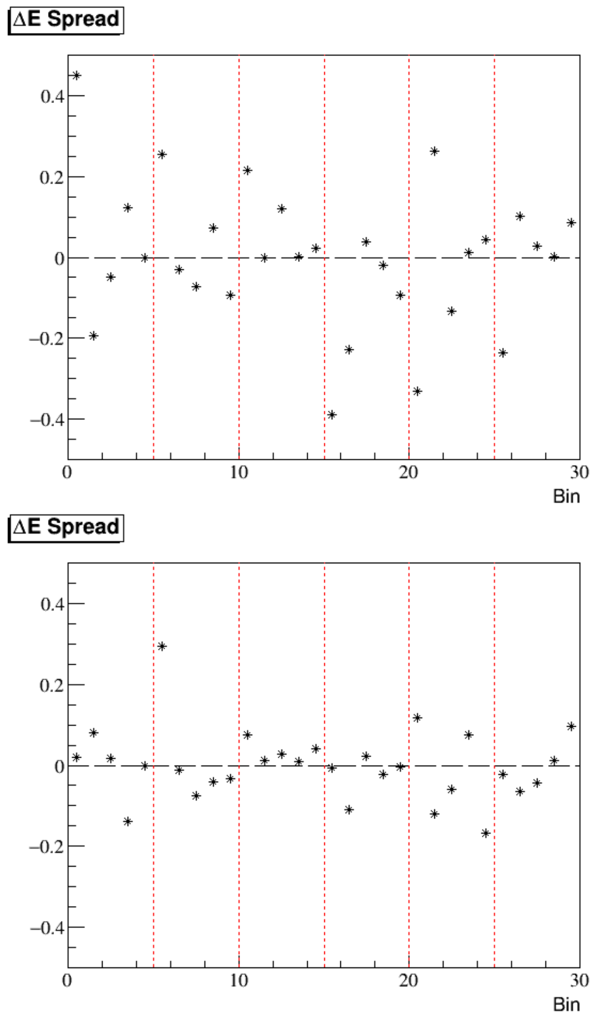

Figure 4.49: Differences in the calculated values of the $\mathbb{E}$ observable for the contracted selection cut (upper) and the expanded selection cut (lower) from the nominal selection cut for the fiducial regions.

From Figure 4.49, we can see that there seems to be no obvious E_γ or $\cos\theta_{K^+}^{CM}$ dependence on the values of $\Delta\mathbb{E}$. The average values obtained are presented in Table 4.15.

The larger of these are chosen to represent the systematic uncertainty inherent in the fiducial region cut.

Selection Cut	Average $\Delta\mathbb{E}$
Contracted Fiducial Region	0.0012
Expanded Fiducial Region	-0.0007

Table 4.15: Summary of the average $\Delta\mathbb{E}$ values obtained for the fiducial cuts.

4.5.6 Σ^- Mass

The spectrum of the reconstructed Σ^- mass, using the missing mass technique ($MM(K^+)$), was shown in Figure 3.31. To assess the stability of this selection cut, the width is expanded and contracted by 1σ, shown in Figure 4.50.

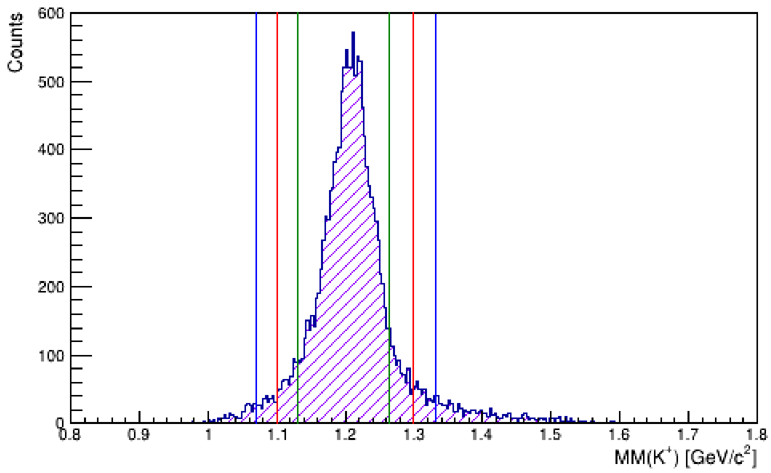

Figure 4.50: Reconstructed Σ^- mass spectrum. The selection cuts used for the systematic studies are shown; M_{Σ^-} 2σ, 3σ, 4σ.

For each of these selections, the observable $\mathbb{E}$ is calculated and compared to the *nominal* selection. These are shown together in Figure 4.51.

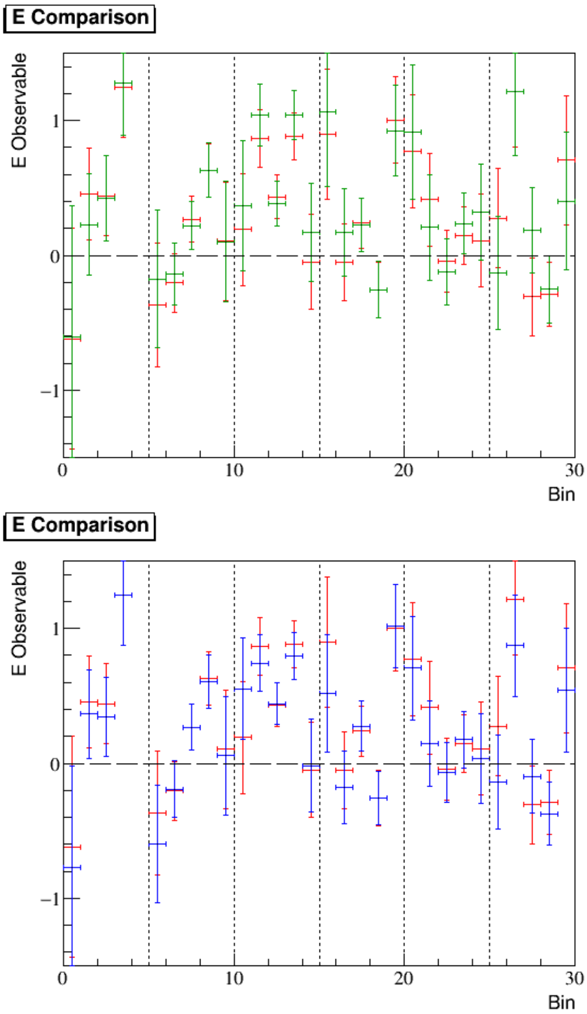

Figure 4.51: Comparisons of the calculated values of the $\mathbb{E}$ observable for the contracted selection cut (upper) and the expanded selection cut (lower) compared with the nominal selection cut for the reconstructed Σ^-.

1140 From Figure 4.51, the variation in the value of the $\mathbb{E}$ observable is well within
1141 the statistical errors for the data. The differences in the observable $\mathbb{E}$ are shown
1142 in Figure 4.52.

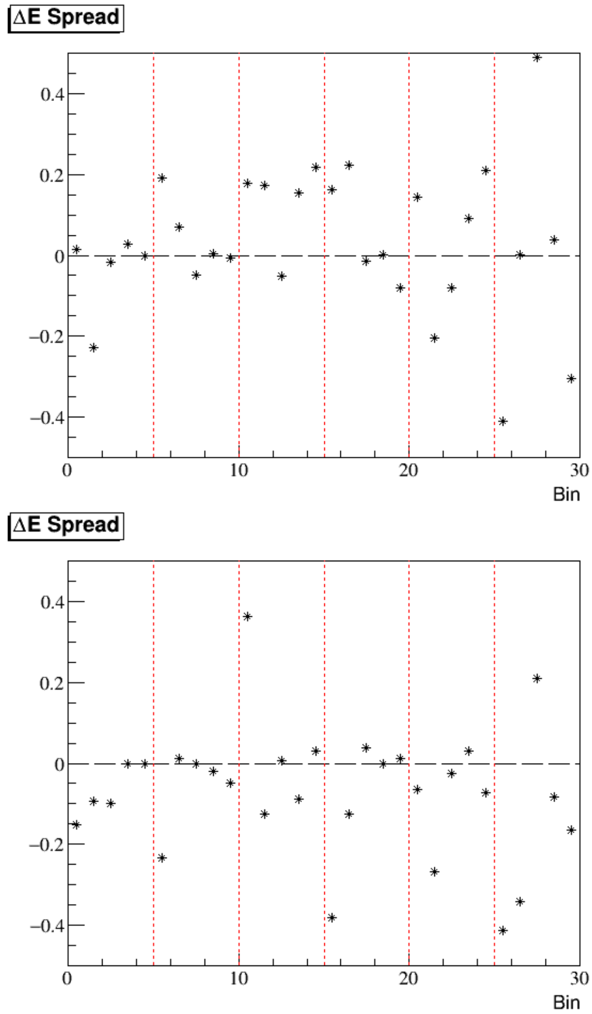

Figure 4.52: Differences in the calculated values of the $\mathbb{E}$ observable for the contracted selection cut (upper) and the expanded selection cut (lower) from the nominal selection cut for the reconstructed Σ^-.

From Figure 4.52, we can see that there seems to be no obvious E_γ or $\cos\theta^{CM}_{K^+}$ dependence on the values of $\Delta\mathbb{E}$. The average values obtained are presented in Table 4.16.

Again, the larger of these are chosen to represent the systematic uncertainty inherent in the Σ^- mass window.

Selection Cut	Average $\Delta\mathbb{E}$
Contracted Σ^- Mass Window	0.0298
Expanded Σ^- Mass Window	-0.0730

Table 4.16: Summary of the average $\Delta\mathbb{E}$ values obtained for the Σ^- mass window.

4.5.7 MisIdentification Cuts

The removal of the misidentified background was discussed in Section 3.2.12. This outlined the selections in $2D$, which will be discussed individually here.

4.5.7.1 $MM(K^+\pi^-)$ vs. $MM(\pi^+\pi^-)$

$$MM(K^+_{\pi^+_{PDG}}) = \underline{\underline{\gamma}} + \underline{\underline{n}} - \underline{\underline{K^+}}_{\pi^+_{PDG}}, \tag{4.13}$$

Equation 4.13 was used in order to identify pions which have been misidentified as kaons. The contamination from this was shown in Figure 3.14. To assess the stability of this selection cut, the cut is expanded and contracted by 1σ in the projection of $MM(K^+_{\pi^+_{PDG}}\pi^-)$, shown in Figure 4.53.

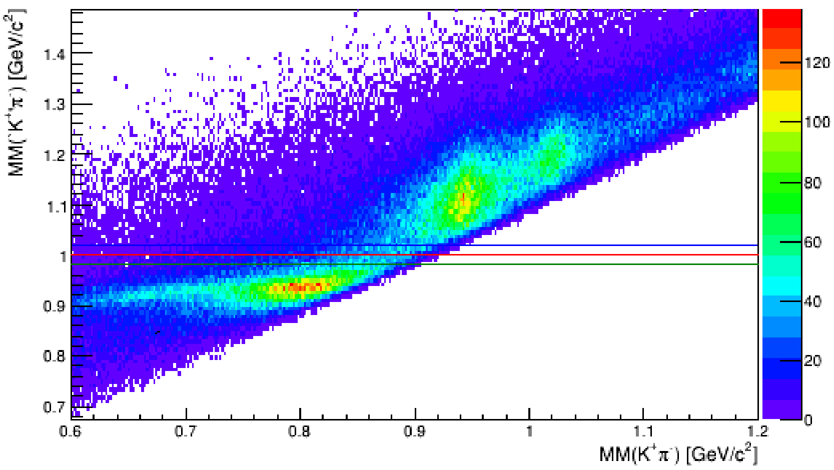

Figure 4.53: Missing mass of $K^+\pi^-$ vs 'K^+'π^-, where 'K^+' has the PDG mass of a π^+. The selection cuts used for the systematic studies are shown; MM('K^+'π^-) 2σ, 3σ, 4σ.

The observable $\mathbb{E}$ is calculated and compared to the *nominal* selection; shown together in Figure 4.54.

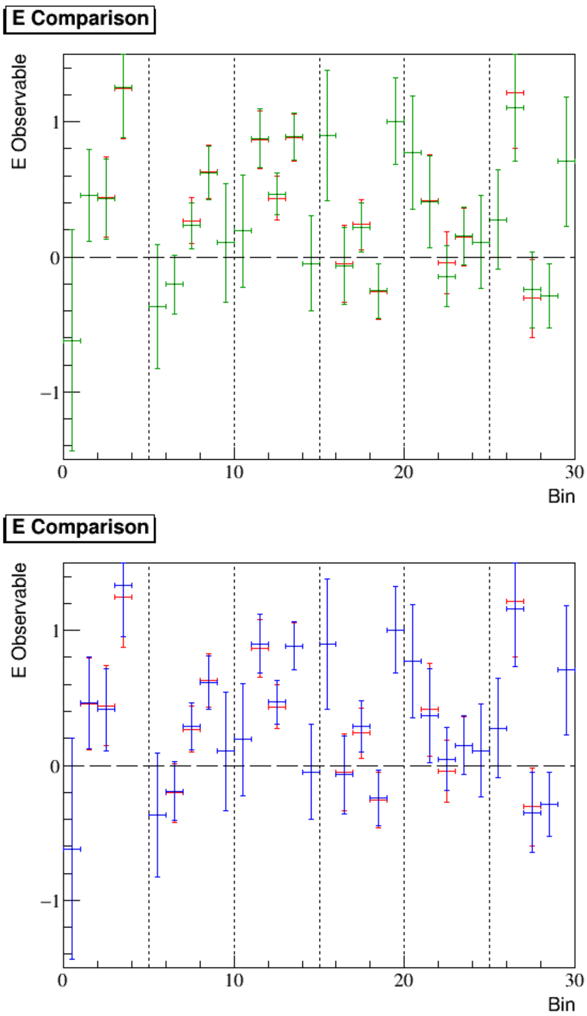

Figure 4.54: Comparisons of the calculated values of the $\mathbb{E}$ observable for the contracted selection cut (upper) and the expanded selection cut (lower) compared with the nominal selection cut to remove pions misidentified as kaons.

From Figure 4.54, we can see that the variation in the value of the $\mathbb{E}$ observable is well within the statistical errors for the data. The differences in the observable $\mathbb{E}$ are shown in Figure 4.55.

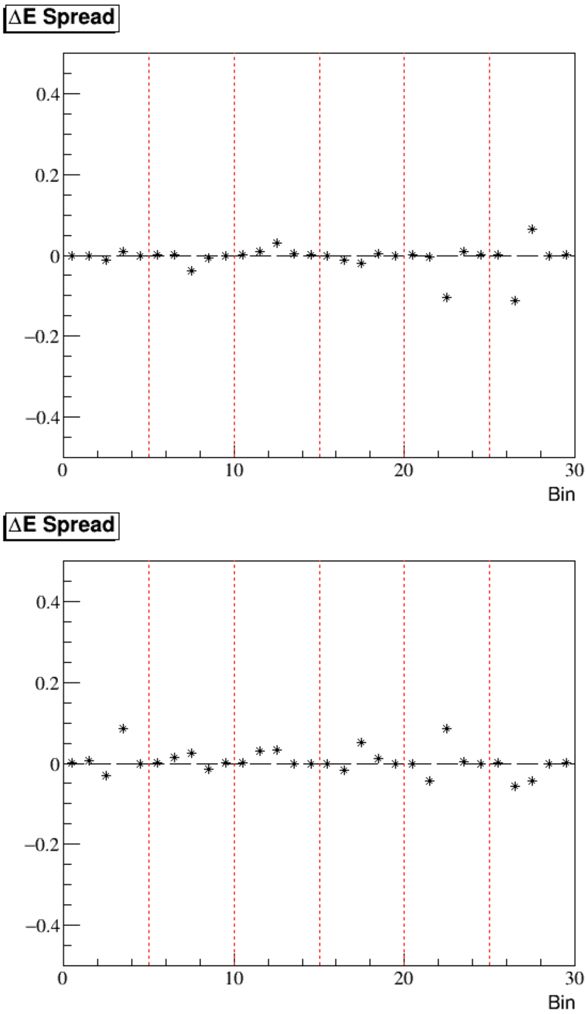

Figure 4.55: Differences in the calculated values of the $\mathbb{E}$ observable for the contracted selection cut (upper) and the expanded selection cut (lower) from the nominal selection cut to remove pions misidentified as kaons.

From Figure 4.55, we can see that there seems to be no obvious E_γ or $\cos\theta^{CM}_{K^+}$ dependence on the values of $\Delta\mathbb{E}$. The average values obtained are presented in Table 4.17.

Once again the larger of these are chosen to represent the systematic uncertainty inherent in the misidentification of pions as kaons.

4.5.7.2 $MM(K^+\pi^-)$ vs. $MM(K^+K^-)$

$$MM(K^+\pi^-_{K^-_{PDG}}) = \underline{\underline{\gamma}} + \underline{\underline{n}} - \underline{\underline{K}}^+ - \underline{\underline{\pi}}^-_{K^-_{PDG}}. \tag{4.14}$$

Selection Cut	Average $\Delta\mathbb{E}$
Contracted $MM(\text{`}K^{+}\text{'}\pi^{-})$ Cut	-0.0060
Expanded $MM(\text{`}K^{+}\text{'}\pi^{-})$ Cut	0.0053

Table 4.17: Summary of the average $\Delta\mathbb{E}$ values obtained for the $MM(\text{`}K^{+}\text{'}\pi^{-})$ selection.

Equation 4.14 was used in order to identify kaons which have been misidentified as pions. The contamination from this was shown in Figure 3.15. To assess the stability of this selection cut, the cut is expanded by 1σ in the projection of $MM(K^{+}\pi^{-}{}_{K^{-}_{PDG}})$, shown in Figure 4.56 [6].

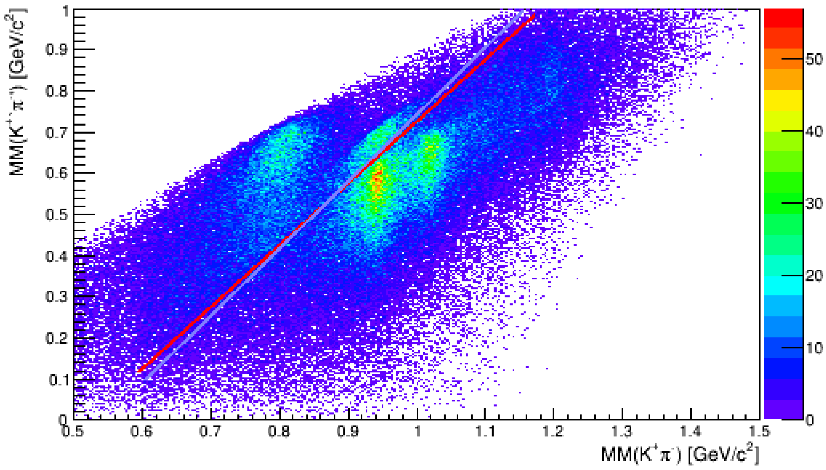

Figure 4.56: Missing mass of $K^{+}\pi^{-}$ vs $K^{+}\text{`}\pi^{-}\text{'}$, where '$\pi^{-}$' has the PDG mass of a $K^{-}$. The selection cuts used for the systematic studies are shown; $MM(K^{+}\text{`}\pi^{-}\text{'})$ 1σ, 2σ.

As with the other cases the observable $\mathbb{E}$ is calculated and compared to the *nominal* selection. This is shown in Figure 4.57.

[6]Colour change for clarity.

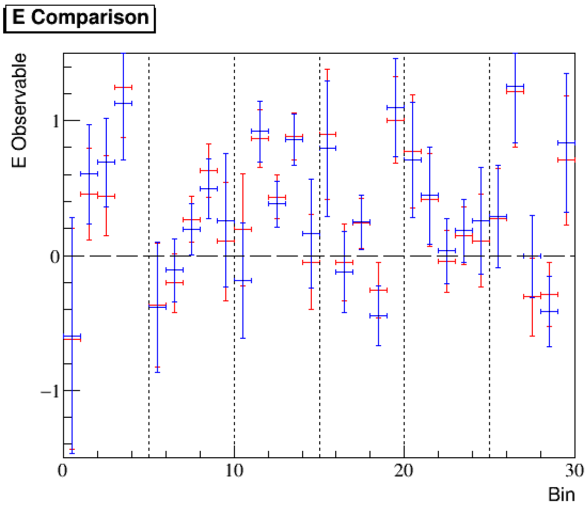

Figure 4.57: Comparisons of the calculated values of the $\mathbb{E}$ observable for the expanded selection cut compared with the nominal selection cut to remove kaons misidentified as pions.

From Figure 4.57, we can see that the variation in the value of the $\mathbb{E}$ observable is well within the statistical errors for the data. The differences in the observable $\mathbb{E}$ are shown in Figure 4.58.

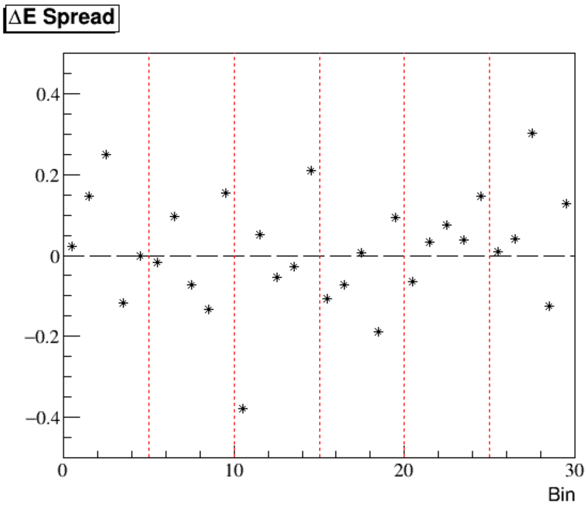

Figure 4.58: Differences in the calculated values of the $\mathbb{E}$ observable for the expanded selection cut from the nominal selection cut to remove kaons misidentified as pions.

From Figure 4.58, we can see that there seems to be no obvious E_γ or $\cos\theta^{CM}_{K^+}$ dependence on the values of $\Delta\mathbb{E}$. The average value obtained is presented in Table 4.18.

Selection Cut	Average $\Delta\mathbb{E}$
Expanded $MM(K^+`\pi^-')$ Cut	0.0173

Table 4.18: Summary of the average $\Delta\mathbb{E}$ value obtained for the $MM(K^+`\pi^-')$ selection.

4.5.7.3 $MM(K^+\pi^-)$ vs. $MM(p\pi^-)$

$$MM(K^+_{p_{PDG}}\pi^-) = \underline{\underline{\gamma}} + \underline{\underline{n}} - \underline{\underline{K}}^+_{p_{PDG}} - \underline{\underline{\pi}}^-. \tag{4.15}$$

Equation 4.15 was used in order to identify protons which have been misidentified as kaons. The contamination from this was shown in Figure 3.17. To assess the stability of this selection cut, the cut is expanded and contracted by 1σ in the projection of $MM({K^+}_{p_{PDG}}\pi^-)$, shown in Figure 4.59.

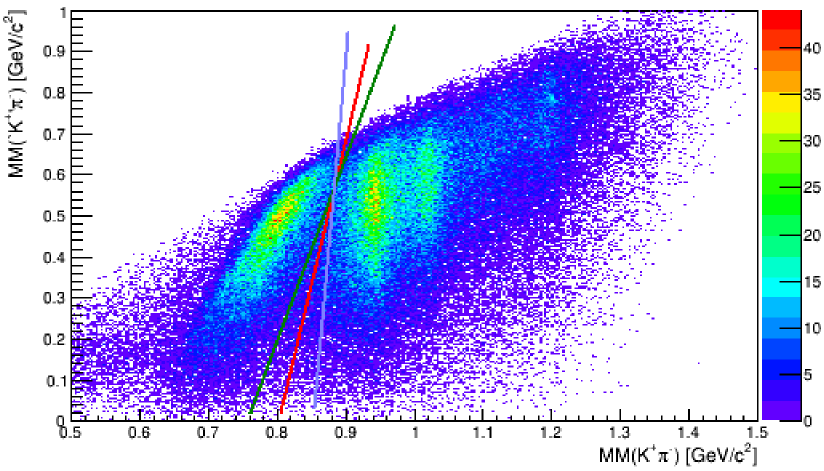

Figure 4.59: Missing mass of $K^+\pi^-$ vs 'K^+'π^-, where 'K^+' has the PDG mass of a p. The selection cuts used for the systematic studies are shown; $MM(`K^+'\pi^-)$ 2σ, 3σ, 4σ.

For each of these selections, the observable $\mathbb{E}$ is calculated and compared to the *nominal* selection. These are shown together in Figure 4.60.

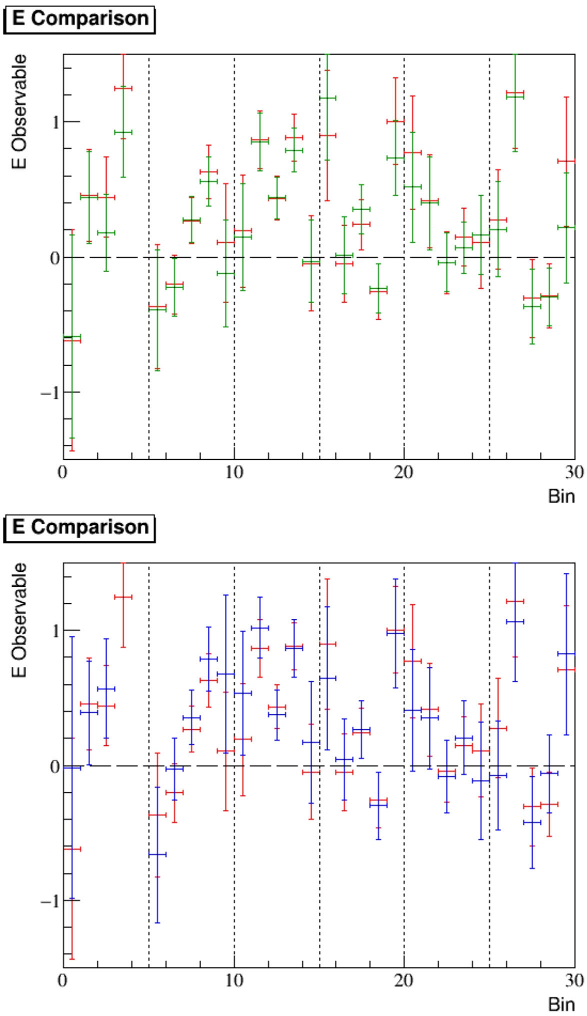

Figure 4.60: Comparisons of the calculated values of the $\mathbb{E}$ observable for the contracted selection cut (upper) and the expanded selection cut (lower) compared with the nominal selection cut to remove protons misidentified as kaons.

From Figure 4.60, we can see once again that the variation in the value of the $\mathbb{E}$ observable is well within the statistical errors for the data. The differences in the observable $\mathbb{E}$ are shown in Figure 4.61.

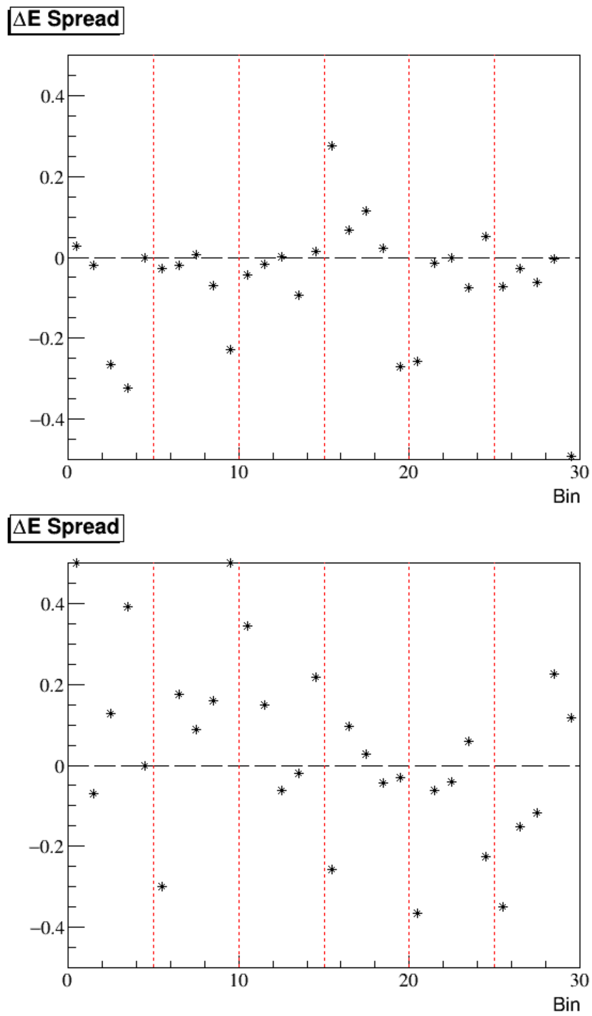

Figure 4.61: Differences in the calculated values of the $\mathbb{E}$ observable for the contracted selection cut (upper) and the expanded selection cut (lower) from the nominal selection cut to remove protons misidentified as kaons.

From Figure 4.61, we can see that there seems to be no obvious E_γ or $\cos\theta_{K^+}^{CM}$ dependence on the values of $\Delta\mathbb{E}$. The average values obtained are presented in Table 4.19.

The larger of these are chosen to represent the systematic uncertainty inherent in the misidentification of protons as kaons.

Selection Cut	Average $\Delta\mathbb{E}$
Contracted $MM($'K^+'$\pi^-)$ Cut	-0.0650
Expanded $MM($'K^+'$\pi^-)$ Cut	0.0508

Table 4.19: Summary of the average $\Delta\mathbb{E}$ values obtained for the $MM($'K^+'$\pi^-)$ selection.

4.5.7.4 $MM(K^+)$ vs. $MM(K^+\pi^-)$

The reconstructed Σ^- and n were used in order to separate different final state contributions. This was shown in Figure 3.19. To assess the stability of this selection cut, the cut is expanded and contracted by 1σ in the projection of $MM(K^+)$, shown in Figure 4.62.

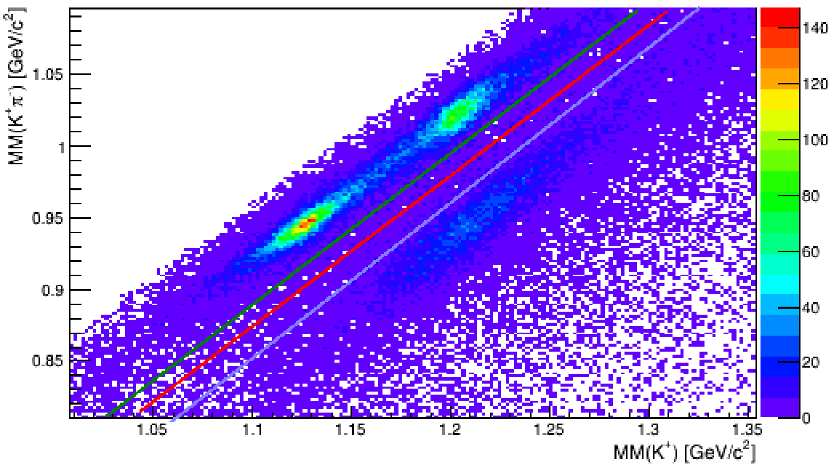

Figure 4.62: Missing mass of K^+ vs $K^+\pi^-$. The selection cuts used for the systematic studies are shown; $MM(K^+)$ 2σ, 3σ, 4σ.

For each of these selections, the observable $\mathbb{E}$ is calculated. The new selections for the systematic studies are compared to the *nominal* selection. These are shown together in Figure 4.63.

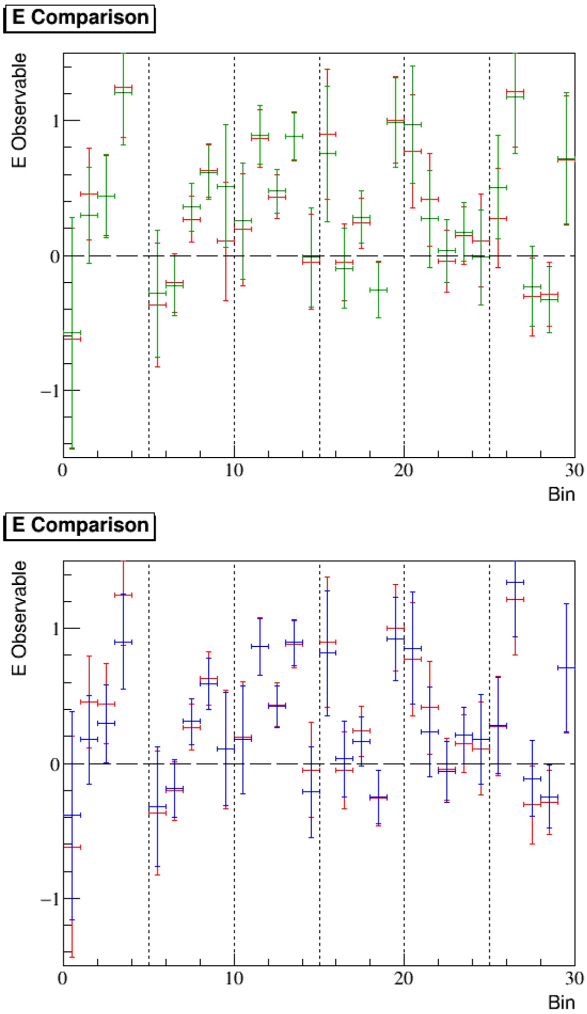

Figure 4.63: Comparisons of the calculated values of the $\mathbb{E}$ observable for the contracted selection cut (upper) and the expanded selection cut (lower) compared with the nominal selection cut to isolate the Σ^- peak.

From Figure 4.63, we can see that the variation in the value of the $\mathbb{E}$ observable is well within the statistical errors for the data. The differences in the observable $\mathbb{E}$ are shown in Figure 4.64.

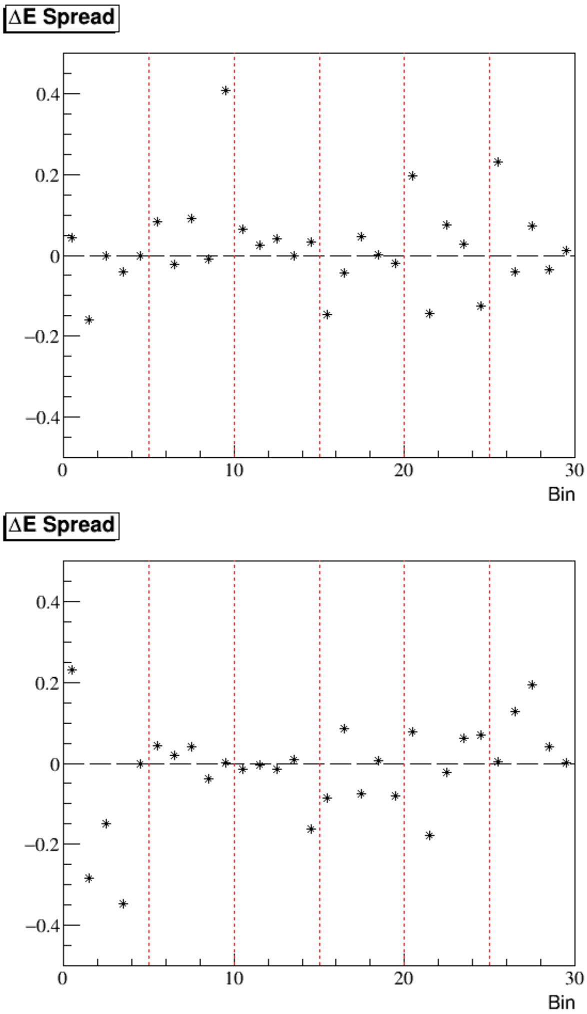

Figure 4.64: Differences in the calculated values of the $\mathbb{E}$ observable for the contracted selection cut (upper) and the expanded selection cut (lower) from the nominal selection cut to isolate the Σ^- peak.

From Figure 4.64, we can see that there seems to be no obvious E_γ or $\cos\theta^{CM}_{K^+}$ dependence on the values of $\Delta\mathbb{E}$. The average values obtained are presented in Table 4.20.

As in other cases, the larger of these are chosen to represent the systematic uncertainty inherent in the misidentification of protons as kaons.

Selection Cut	Average $\Delta\mathbb{E}$
Contracted Cut	0.0206
Expanded Cut	−0.0190

Table 4.20: Summary of the average $\Delta\mathbb{E}$ values obtained for the $MM(`K^+`\pi^-)$ selection.

4.5.8 Combining Selection Systematics

From these individual contributions of the systematic uncertainties for the event selection a total error may be obtained by combining these in quadrature. This, however is not trivial, since in order to preserve statistics the misidentification selections were made simultaneously, meaning they are highly correlated. This correlation means that the systematics from the misidentification of particles cannot be considered as independent effects. The largest of these systematic uncertainties was chosen to represent the contribution from the misidentification selection. These were then combined in quadrature, which are summarised in Table 4.21.

Selection Cut	Associated Systematic Uncertainty
Best Photon Timing	0.0097
$\Delta\beta_{K^+}$	0.0076
$\Delta\beta_{\pi^-}$	−0.0406
Reconstructed Neutron	−0.0337
Z-Vertex	−0.0261
Fiducial Regions	0.0012
Σ^- Mass	−0.0730
MisIdentification	−0.065
Combined	0.11

Table 4.21: Summary of the systematic uncertainties for selection cut studies.

Results for all bins of the $\mathbb{E}$ observable are shown with this combined systematic uncertainty included in Figure 4.65.

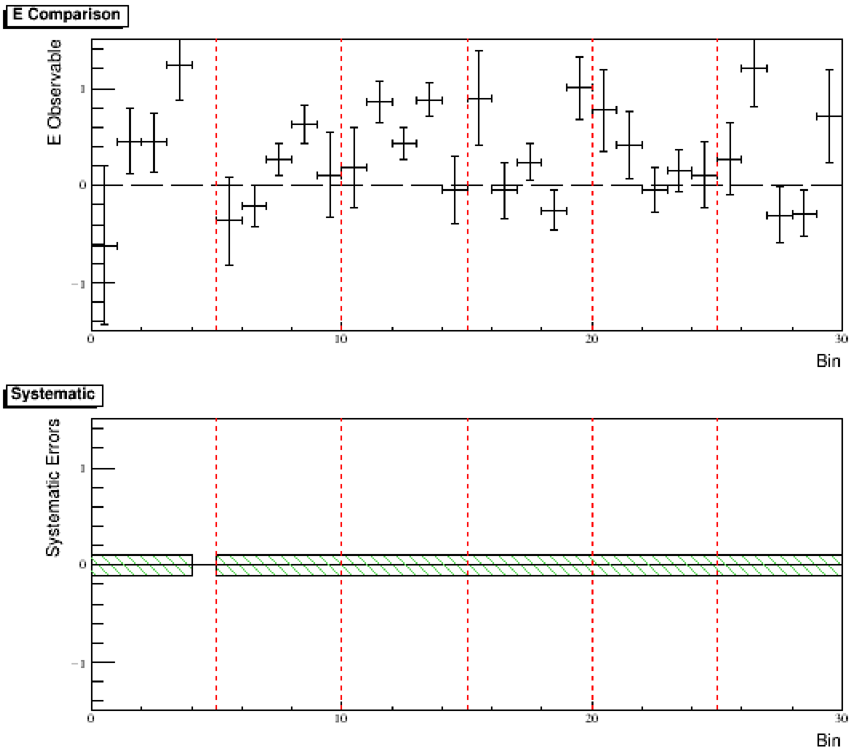

Figure 4.65: Results for the $\mathbb{E}$ double-polarisation in 200 MeV bins in E_γ, shown with statistical errors (upper). The combined systematic errors for the selection cuts are also shown (lower).

4.6 Polarisation Systematic

Systematics arising from the target polarisation, the photon beam polarisation and the beam-charge asymmetry which must be considered. The systematic uncertainty of the target polarisation is summarised in Table 4.22. The photon beam polarisation for each run period was presented in Table 2.3, based on Møller measurements. The uncertainty in the photon beam polarisation was calculated to be $3.3 - 3.5\%$ for $82 - 88\%$ polarisation. This was shown to dominate the uncertainty in the beam-charge asymmetry, which was of order 0.1% [14]. This leads to the systematic uncertainties presented in Table 4.23.

The systematic error associated with the empty target subtraction was taken to be negligible compared to the statistical error, from the agreement between different analysis methods, shown in Section 4.2.3.3. Systematics in the measured

Uncertainties in reference to ***T***hermal ***E***quilibrium (TE) Measurements		
PD Noise	0.3%	White noise in PD NMR while in HDice lab
Temperature	0.2%	Drift, thermal gradients in HD from radiant heat load
H Background	0.4%	H background with no target
Stochiometry	0.1%	Deviation of $H : D$ of $1 : 1$, due to H_2 and D_2 impurities
Background Subtraction	0.6%	Error in signal integral from imperfect separation of background
Incomplete Relaxation	0.5%	$T1$ for TE measurement can be comparable to sweep time
Uncertainties in measurement of ***F***rozen-***S***pin (FS) signal		
IBC Noise	0.6%	Residual effect of white noise in IBC NMR and PD
Hall-B Noise Jumps	0.5%	Variations in signal area after correction for signal jumps
Circuit Non-linearity	4.0%	From the quadratic dependence of the circuit transducer gain
RF Inhomogeneity	1.4%	Field inhomogeneity
RF Depolarisation	0.1%	Residual uncorrected decrement from repeated RF sweeps
Uncertainties in relating the FS signal to the TE measurement		
Circuit Drift	1.8%	Variation from connecting the FS signal to the TE reference
Lock-in Gain Error	2.9%	SRS 844 manufacturer's gain error
Differential Ramp-rate	1.0%	Actual ramp-rate differs from nominal
TC Transfer Losses	2.0%	Variation in polarisation loss during a TC transfer
Total Systematic Error	6.0%	For both H and D polarisation

Table 4.22: Summary of the systematic uncertainties for HD polarisation measurement [14].

photon flux are assumed to cancel in the asymmetry and to be of similar magnitude for both helicities. There was no significant variation in the asymmetry found when varying the particle selection cuts, these were found to be consistent within uncertainties.

These polarisation uncertainties are combined in quadrature in order to give a systematic in the polarisation factor of the $\mathbb{E}$ observable:

$$\frac{1}{P_\gamma P_\oplus}. \tag{4.16}$$

Contribution to Polarisation Systematic	Uncertainty
HD Polarisation Measurement	6.0%
Photon Beam Polarisation	3.4%
Beam-charge Asymmetry	0.1%
Total Polarisation Systematic Uncertainty	6.9%

Table 4.23: Summary of the systematic uncertainties for polarisation measurements.

Results for all bins of the $\mathbb{E}$ observable are shown with this combined systematic uncertainty from selection cuts and polarisation included in Figure 4.66.

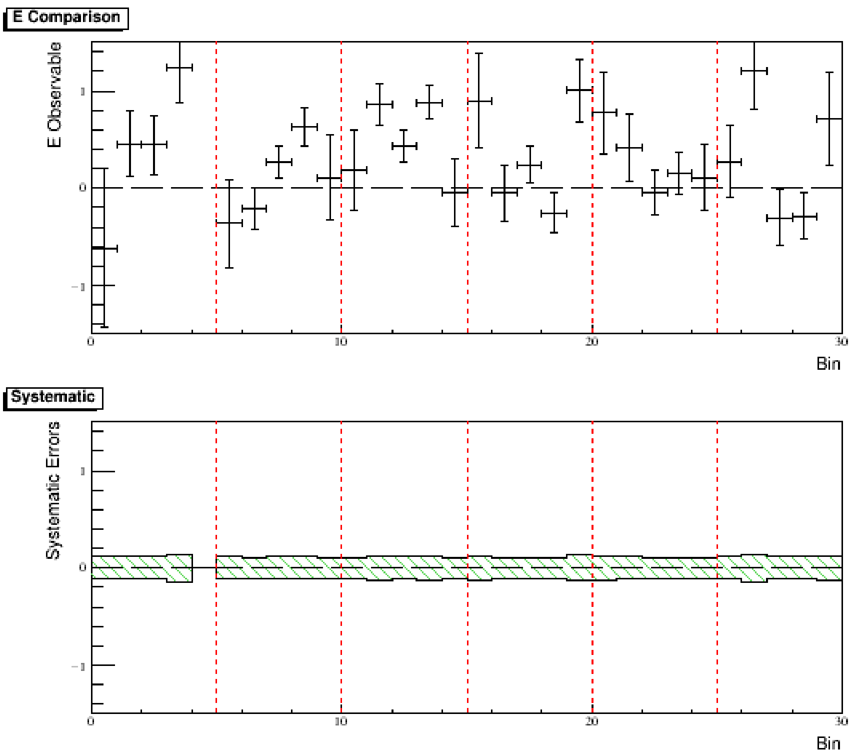

Figure 4.66: Results for the $\mathbb{E}$ double-polarisation in 200 MeV bins in E_γ, shown with statistical errors (upper). The combined systematic errors for the selection cuts and polarisation are also shown (lower).

4.7 Background Estimation from the $K^+\Sigma^0$ Channel

The main backgrounds present in the $K^+\Sigma^-$ channel arise from the decays of Λ and Σ^0. As was presented, in Section 3.2.13, the contribution from $K^+\Lambda$ can be efficiently removed using the data selection cuts. The $K^+\Sigma^0$ channel has a similar kinematics to the channel of interest and its full suppression is not possible. An accurate estimate of the contribution from $K^+\Sigma^0$ to the $K^+\Sigma^-$ yield can be made using the experimental data.

The background contribution coming from the proton in this channel can be estimated by considering the inclusive K^+X skim. This allows for proton events to be included in the selection rather than being removed during the initial skim.

This is useful because if we remember that CLAS does not have 100% detector acceptance, some of these events will be incorrectly selected because the proton, which would usually be used to veto the event, was not detected. This can occur when the proton hits the torus coils for example.

It is possible to include a final state proton in the particle selection, where these events can be considered, while allowing all other selection requirements to remain intact. This means that we can evaluate the contribution of events containing an undetected proton by comparing events with detected protons and evaluating the detection efficiency of protons in CLAS.

Using the K^+X skim, the standard analysis code can be run alongside a code which includes the proton. This leaves us with two different final states:

- $K^+\pi^-n$,
- $K^+\pi^-p$,

where if there is a third particle detected it must be a neutron or a proton respectively. These final states can be compared which indicates the ratio of Σ^0 events which are rejected using the exclusive $K^+\Sigma^-$ skim. Considering all energies and angles, the comparison between the events in these final states are shown in Table 4.24.

Events Present $K^+\pi^-n$	Events Present $K^+\pi^-p$	Proton Final State Percentage (%)
10193	1662	16.3

Table 4.24: Summary of the number of final state events when excluding and including a final state proton.

The total amount of Σ^0 which can contaminate the final sample, of course, depends on the proton detection efficiency of CLAS. For the $g14$ run period this was calculated to be $\sim 60\%$[7], meaning that $\sim 40\%$ of the proton events were not detected and removed but remain in the sample.

The percentage contamination over all energies and angles can be calculated to be 10.5(3)%.

[7]From private conversations with Franz Klein; periods *silver*1 and *silver*2 had a proton efficiency of $\sim 70\%$, whereas all other periods were $\sim 60\%$. We use the worst case scenario for the calculations here.

Energy Bin GeV	Proton Contamination (%)	Error (%)
1.1-1.3 GeV	12.5	2.1
1.3-1.5 GeV	12.7	1.5
1.5-1.7 GeV	11.7	1.3
1.7-1.9 GeV	17.9	2.4
1.9-2.1 GeV	14.1	1.9
2.1-2.3 GeV	14.8	2.4

Table 4.25: Outline of how the proton contribution evolves with the photon energy, E_γ.

4.7.1 Energy Dependence of $K^+\Sigma^0$

The percentage of proton events mixing with the $K^+\Sigma^-$ channel can be considered in terms of the photon energy. The contributions in each 200 MeV energy bin are outlined in Table 4.25.

There is some variation in the contribution with energy, particularly in the fourth energy bin, detailed further in Section 4.7.2. Otherwise, these results indicate that the contribution is relatively stable with respect to photon energy, which is expected as the cross section for the $K^+\Sigma^0$ channel mirrors that of the $K^+\Sigma^-$ channel well.

4.7.2 Angular Dependence of $K^+\Sigma^0$

Similarly, the contribution can be expanded in terms of the kaon production angle, these are separated into cases for parallel and anti-parallel beam-target helicities. These shown in Tables 4.26, 4.27 and Tables 4.28, 4.29 for parallel and anti-parallel respectively.

A key feature seen here is the strong contribution at very backward angles, as much as a factor 2 or in some cases greater, than at central and forward angles. Considering the issue seen in the photon energy bin 1.7-1.9 GeV; we see that in the first angular bin the contamination is $\sim$ 40%. This is a significantly larger value than other bins effect of the background.

An estimation of the background is included in the systematic error estimate for the final results.

Angular Bin ($\cos\theta^{CM}_{K^+}$)	Contamination (%)	Error (%)
1.1-1.3 GeV		
(-1.0)-(-0.6)	25.6	7.8
(-0.6)-(-0.2)	10.6	2.0
(-0.2)-0.2	6.1	1.4
0.2-0.6	7.5	2.1
0.6-1.0	N/A	N/A
1.3-1.5 GeV		
(-1.0)-(-0.6)	16.9	4.0
(-0.6)-(-0.2)	14.8	2.0
(-0.2)-0.2	9.8	1.2
0.2-0.6	5.5	1.0
0.6-1.0	16.7	5.9
1.5-1.7 GeV		
(-1.0)-(-0.6)	22.8	5.2
(-0.6)-(-0.2)	13.5	2.3
(-0.2)-0.2	6.9	1.0
0.2-0.6	8.5	1.3
0.6-1.0	6.9	2.4

Table 4.26: Outline of how the proton contribution evolves with the cosine of the K^+ centre-of-mass angle, $\cos\theta^{CM}_{K^+}$, from 1.1- 1.7 GeV for parallel beam-target helicity, $N_{\frac{3}{2}}$.

Angular Bin ($\cos\theta^{CM}_{K^+}$)	Contamination (%)	Error (%)
1.7-1.9 GeV		
(-1.0)-(-0.6)	39.3	10.3
(-0.6)-(-0.2)	16.7	3.5
(-0.2)-0.2	14.2	2.1
0.2-0.6	9.6	1.7
0.6-1.0	9.8	3.3
1.9-2.1 GeV		
(-1.0)-(-0.6)	23.8	7.2
(-0.6)-(-0.2)	14.6	4.3
(-0.2)-0.2	16.0	2.8
0.2-0.6	8.0	1.8
0.6-1.0	8.0	3.2
2.1-2.3 GeV		
(-1.0)-(-0.6)	16.7	5.4
(-0.6)-(-0.2)	25.0	8.5
(-0.2)-0.2	14.9	3.8
0.2-0.6	5.7	1.7
0.6-1.0	11.8	5.2

Table 4.27: Outline of how the proton contribution evolves with the cosine of the K^+ centre-of-mass angle, $\cos\theta^{CM}_{K^+}$, from 1.7- 2.3 GeV for parallel beam-target helicity, $N_{\frac{3}{2}}$.

Angular Bin ($\cos\theta^{CM}_{K^+}$)	Contamination (%)	Error (%)
1.1-1.3 GeV		
(-1.0)-(-0.6)	41.2	11.4
(-0.6)-(-0.2)	13.8	2.3
(-0.2)-0.2	9.4	1.8
0.2-0.6	6.7	1.8
0.6-1.0	N/A	N/A
1.3-1.5 GeV		
(-1.0)-(-0.6)	27.8	6.0
(-0.6)-(-0.2)	12.8	1.7
(-0.2)-0.2	6.6	1.0
0.2-0.6	5.9	1.0
0.6-1.0	11.1	4.5
1.5-1.7 GeV		
(-1.0)-(-0.6)	25.2	5.6
(-0.6)-(-0.2)	11.1	1.8
(-0.2)-0.2	8.5	1.1
0.2-0.6	6.3	1.0
0.6-1.0	5.5	1.9

Table 4.28: Outline of how the proton contribution evolves with the cosine of the K^+ centre-of-mass angle, $\cos\theta^{CM}_{K^+}$, from 1.1- 1.7 GeV for anti-parallel beam-target helicity, $N_{\frac{1}{2}}$.

Angular Bin ($\cos\theta_{K^+}^{CM}$)	Contamination (%)	Error (%)
1.7-1.9 GeV		
(-1.0)-(-0.6)	34.2	9.7
(-0.6)-(-0.2)	17.5	3.4
(-0.2)-0.2	11.1	1.6
0.2-0.6	10.8	1.8
0.6-1.0	6.3	2.1
1.9-2.1 GeV		
(-1.0)-(-0.6)	27.8	7.4
(-0.6)-(-0.2)	17.3	5.2
(-0.2)-0.2	15.1	2.8
0.2-0.6	7.8	1.8
0.6-1.0	3.8	1.9
2.1-2.3 GeV		
(-1.0)-(-0.6)	27.0	7.3
(-0.6)-(-0.2)	17.5	6.2
(-0.2)-0.2	19.1	4.0
0.2-0.6	10.8	2.6
0.6-1.0	1.8	1.8

Table 4.29: Outline of how the proton contribution evolves with the cosine of the K^+ centre-of-mass angle, $\cos\theta_{K^+}^{CM}$, from 1.7- 2.3 GeV for anti-parallel beam-target helicity, $N_{\frac{1}{2}}$.

4.7.3 Producing a Correction

Accounting for the dilution in the $\mathbb{E}$ observable from the $K^+\Sigma^0$ channel requires careful treatment of the construction of the observable.

$\mathbb{E}$ was defined in Equation 1.6, but is shown again here:

$$\mathbb{E} = \frac{1}{P_\gamma P_\oplus}\mathcal{A}, \tag{4.17}$$

where $\mathcal{A}$ was defined as:

$$\mathcal{A} = \frac{N_{\frac{1}{2}}(\rightarrow\Leftarrow) - N_{\frac{3}{2}}(\leftarrow\Leftarrow)}{N_{\frac{1}{2}}(\rightarrow\Rightarrow) + N_{\frac{3}{2}}(\leftarrow\Rightarrow)}, \tag{4.18}$$

where N represents the appropriate number of events for the corresponding target $(\rightarrow)$ and beam $(\Rightarrow)$ polarisation vectors.

If we realise that the observable $\mathbb{E}$ we measure is really some combination of the observable from the $K^+\Sigma^-$ channel ($\mathbb{E}_{\Sigma^-}$) and the $K^+\Sigma^0$ channel ($\mathbb{E}_{\Sigma^0}$), we can consider the measured observable as the *total* ($\mathbb{E}_{total}$):

$$\mathbb{E}_{total} = \epsilon\mathbb{E}_{\Sigma^-} + \xi\mathbb{E}_{\Sigma^0}, \tag{4.19}$$

where $\epsilon, \xi \in \mathbb{Q}[0,1]$ and $\epsilon + \xi \stackrel{!}{=} 1$. N can be expanded in a similar way:

$$N^{total} = N^{\Sigma^-} + N^{\Sigma^0}, \tag{4.20}$$

where we wish to isolate the Σ^- term:

$$N^{total} = N^{\Sigma^-}(1 + \frac{N^{\Sigma^0}}{N^{\Sigma^-}}). \tag{4.21}$$

Equation 4.21 can then be simplified:

$$N^{total} = N^{\Sigma^-}(1 + C). \tag{4.22}$$

where the contamination, C, is defined as $\frac{N^{\Sigma^0}}{N^{\Sigma^-}}$. It should be noted that these should be treated separately, in the $\frac{1}{2}$ and $\frac{3}{2}$ case:

$$\begin{aligned} N^{total}_{\frac{1}{2}} &= N^{\Sigma^-}_{\frac{1}{2}}(1 + C_{\frac{1}{2}}), \\ N^{total}_{\frac{3}{2}} &= N^{\Sigma^-}_{\frac{3}{2}}(1 + C_{\frac{3}{2}}). \end{aligned} \tag{4.23}$$

The values of $C_{\frac{1}{2}}$ and $C_{\frac{3}{2}}$ are those which have been calculated for the contaminations throughout Tables 4.26-4.29. We can therefore construct the asymmetry $\mathcal{A}$ in this notation:

$$\mathcal{A} = \frac{N_{\frac{1}{2}}^{\Sigma^-}(1 + C_{\frac{1}{2}}) - N_{\frac{3}{2}}^{\Sigma^-}(1 + C_{\frac{3}{2}})}{N_{\frac{1}{2}}^{\Sigma^-}(1 + C_{\frac{1}{2}}) + N_{\frac{3}{2}}^{\Sigma^-}(1 + C_{\frac{3}{2}})}. \tag{4.24}$$

In the case where the target-asymmetry of the two channels are the same, we have the case, $C_{\frac{1}{2}} = C_{\frac{3}{2}}$.

Finally we wish to present the *true* $\mathbb{E}$ observable for the $K^+\Sigma^-$ channel.

$$\begin{aligned} N_{\frac{1}{2}}^{\Sigma^-} &= \frac{N_{\frac{1}{2}}^{total}}{(1 + C_{\frac{1}{2}})}, \\ N_{\frac{3}{2}}^{\Sigma^-} &= \frac{N_{\frac{3}{2}}^{total}}{(1 + C_{\frac{3}{2}})}. \end{aligned} \tag{4.25}$$

The double-polarisation observable $\mathbb{E}$ can then be presented in this form:

$$\mathbb{E}_{\Sigma^-} = \frac{1}{P_\gamma P_\oplus}\left[\left(\frac{N_{\frac{1}{2}}^{total}}{(1 + C_{\frac{1}{2}})} - \frac{N_{\frac{3}{2}}^{total}}{(1 + C_{\frac{3}{2}})}\right) \Big/ \left(\frac{N_{\frac{1}{2}}^{total}}{(1 + C_{\frac{1}{2}})} + \frac{N_{\frac{3}{2}}^{total}}{(1 + C_{\frac{3}{2}})}\right)\right]. \tag{4.26}$$

This corrected for of the $\mathbb{E}$ double-polarisation observable is used to provide the final results shown in the coming chapter.

Chapter 5

Extraction of Polarisation Observables

This chapter outlines the extraction of the double-polarisation observable $\mathbb{E}$ for the reaction $\gamma n \rightarrow K^+\Sigma^-$ from the $g14$ experimental data.

5.1 Angle and Energy Bin Choice

The extraction of the $\mathbb{E}$ observable from the $\gamma n \rightarrow K^+\Sigma^-$ reaction is considered as a function of E_γ (lab frame) and $cos\theta^{CM}_{K^+}$ (centre-of-mass frame).

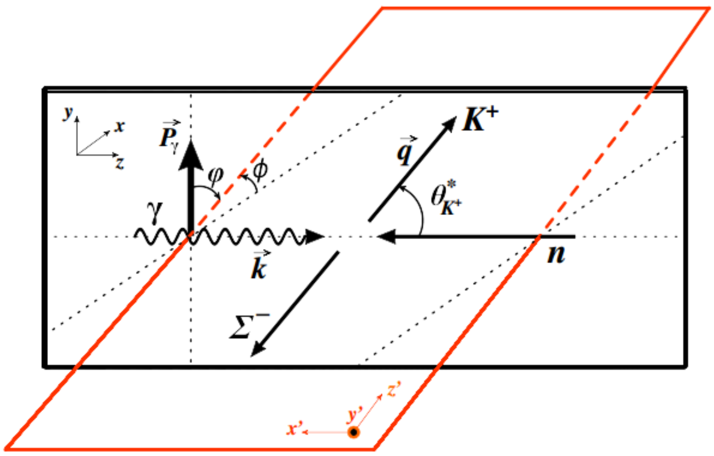

Figure 5.1: Diagram showing the kinematics for the $\gamma n \rightarrow K^+\Sigma^-$ in the centre-of mass frame [23].

The binning of each of these must be carefully chosen. There are were two possibilities considered:

- Bin according to some standard spacing of bin centres.
- Bin according to equal bin statistics.

In the first case, some bins can suffer from very low statistics and therefore be of little use in terms of analysing power. In the second case, bins are often asymmetric and may be problematic when integrating over large intervals. Therefore, it can be seen that there is a balance to consider between these two binning methods.

5.1.1 E_γ Binning

The binning in E_γ, was chosen to be 200 MeV. This was chosen after considering the total statistics available to the channel. Although more bins are preferable, this would mean that the errors within each E_γ bin would be considerably larger. Fortunately, the $\mathbb{E}$ observable does not evolve quickly in terms of photon energy and at the scale of 200 MeV there is limited movement. The theoretical predictions of the observable are considered explicitly in Section 5.4.

The full photon energy spectrum is shown in Figure 5.2.

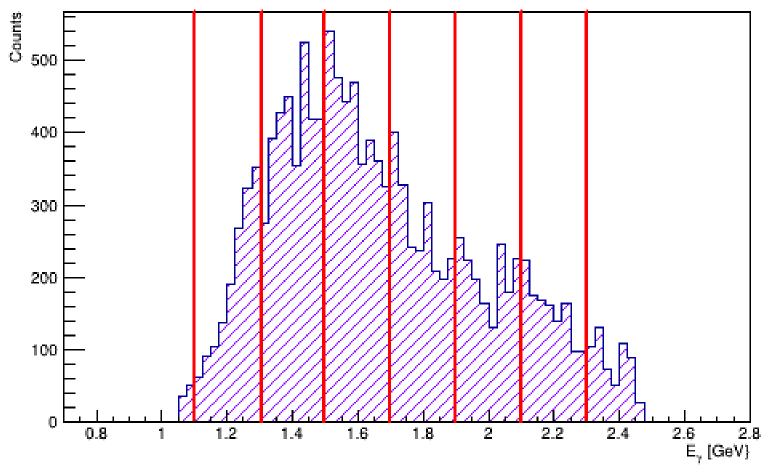

Figure 5.2: Photon energy spectrum, after all event selections have taken place. The binning is shown in red.

The photon energy bins chosen are shown in Table 5.1, along with the respective statistics of each bin.

E_γ Bin	Energies (GeV)	Percentage of Events (approx. %)
1	1.1-1.3	13.1
2	1.3-1.5	23.6
3	1.5-1.7	24.3
4	1.7-1.9	15.5
5	1.9-2.1	12.9
6	2.1-2.3	10.6

Table 5.1: Energy bins (200 MeV width) used for the polarisation observable measurement.

5.1.2 $cos\theta_{K^+}^{CM}$ Binning

The binning in $cos\theta_{K^+}^{CM}$ was selected using symmetric bins over the complete angular range of $\theta_{K^+}^{CM}$ ($\cos\theta_{K^+}^{CM}$) $= [-1, 1]$. Again, due to statistics a relatively small number of angular bins were selected. Five angular bins per photon energy were used to extract the measurement of $\mathbb{E}$. The distribution of $\cos\theta_{K^+}^{CM}$ over all energies is shown in Figure 5.3.

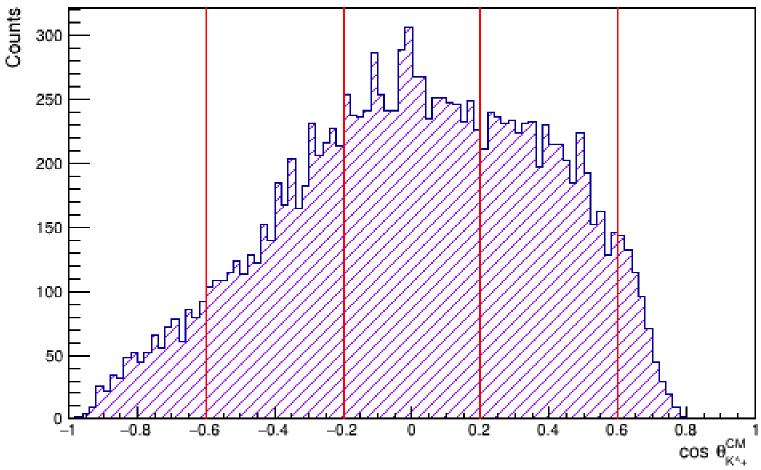

Figure 5.3: Centre-of-mass angular distribution for K^+. The binning is shown in red.

From this distribution, it is clear that it is the central bins which contain most of the events, and although this is roughly symmetric, it is skewed towards the backward angles. An equal bin width was chosen in order to maintain the good statistics in the central bins. The bins were chosen to be of width 0.4 in $\cos\theta^{CM}_{K^+}$; these are shown explicitly in Table 5.2.

$\cos\theta^{CM}_{K^+}\theta$ Bin	Values	Percentage of Events (approx. %)
1	(-1.0)-(-0.6)	7.3
2	(-0.6)-(-0.2)	19.7
3	(-0.2)-0.2	36.0
4	0.2-0.6	31.1
5	0.6-0.8	5.9

Table 5.2: Angular bins (of width 0.4) used for the polarisation observable measurement.

5.2 Extracting Observables for Kaon Photoproduction

The three parameters to consider in the extraction of the $\mathbb{E}$ observable are the beam-asymmetry ($\mathcal{A}$), the polarisation of the photon (P_γ) and the polarisation of the target ($P_\oplus$).

The beam-asymmetry is calculated as shown in Equation 1.5, while the target polarisation was calculated using NMR measurements during the run and are shown in Table 2.3. The photon polarisation however, is calculated on an event by event basis.

The circularly polarised photons are produced using a longitudinally polarised electron beam, incident on a bremsstrahlung radiator. The degree of polarisation depends on the ratio of energies, $x = E_\gamma / E_{e^-}$. This ratio allows for calculation of the polarisation of the incident photon [26]:

$$P_\gamma = P_{e^-} \frac{4x - x^2}{4 - 4x + 3x^2}. \tag{5.1}$$

The degree of photon polarisation is considered separately in each energy bin as there is a photon energy dependence that must be accounted for. So the mean value of photon polarisation is taken for each bin. The evolution of photon polarisation with photon energy is shown in Figure 5.4, while the photon polarisation for each energy bin is considered in Table 5.3.

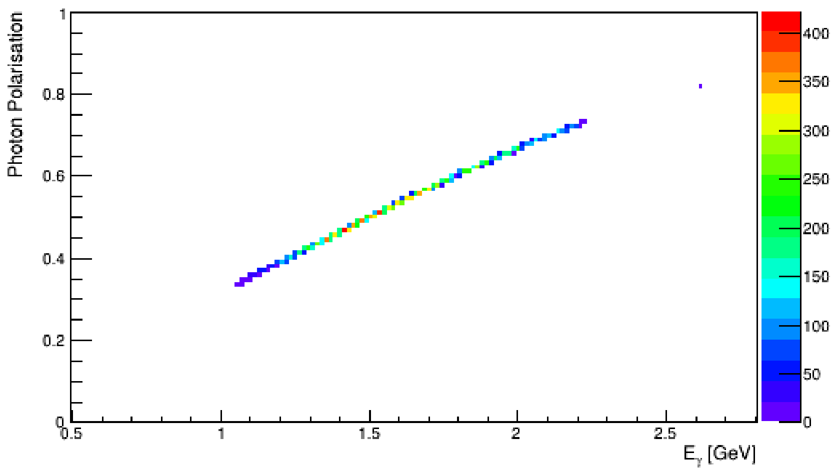

Figure 5.4: Photon energy (E_γ) vs photon polarisation.

E_γ Bin (GeV)	Average Photon Polarisation (approx. %)
1.1-1.3	60
1.3-1.5	68
1.5-1.7	76
1.7-1.9	82
1.9-2.1	86
2.1-2.3	87
1.1-2.3	76

Table 5.3: Summary of how average photon beam polarisation relates to the selected photon energy bins.

5.3 Combining Period Results

The *Gold2* and *Silver* periods were combined into one complete dataset in order to improve the statistics for calculating the beam-asymmetry and therefore the errors of the observable $\mathbb{E}$. It is important to ensure that these periods are appropriately weighted when they are combined as each will have differing statistics. This can be thought of as weighting the value of the polarisation observable in accordance with the error on the value; i.e. imprecise values with large errors are thought of as less reliable while more accurate values with smaller errors are weighted more heavily.

A weighted mean was used when periods were combined to ensure that contributions from each target period are appropriately accounted for. For a set of data, $[x_1, x_2, ..., x_n]$, the weighted arithmetic mean is written as:

$$\bar{x} = \frac{\sum\limits_{i=1}^{n} w_i x_i}{\sum\limits_{i=1}^{n} w_i}, \tag{5.2}$$

where w_i is the variable which is being used to weight the data[1].

5.4 Current Theoretical Model Prediction

The two models used as a first comparison were KaonMAID, and Bonn-Gatchina. The plots of the polarisation observable $\mathbb{E}$, use two theoretical predictions for each model. These show the predictions from the extreme values of each bin which are relatively wide (200 MeV) due to the low statistics available. The predictions at the high E_γ end of the bin are shown in red and the lower in blue.

5.4.1 KaonMAID

Predictions from the KaonMAID model [27] as a function of photon energy are shown in Figures 5.5 and 5.6[2]

[1] In our case, the number of events in the target period is used to represent the analysing power of each period.

[2] Predictions received from Terry Mart, of the Universitas Indonesia, in October 2016.

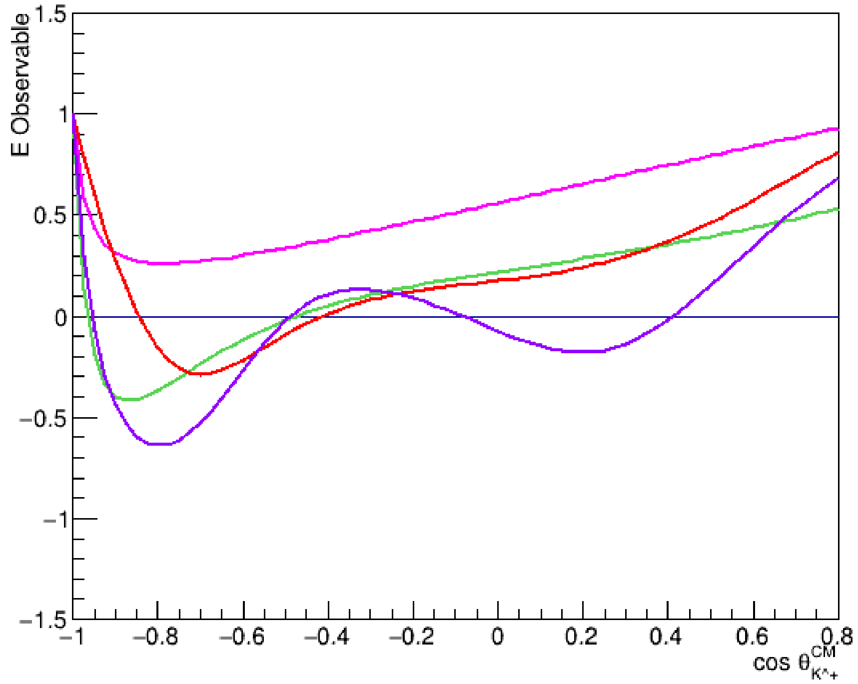

Figure 5.5: Predictions from KaonMAID for $\mathbb{E}$ in the reaction $\gamma n \to K^+\Sigma^-$. These are plotted every 200 MeV: 1100, 1300, 1500, 1700.

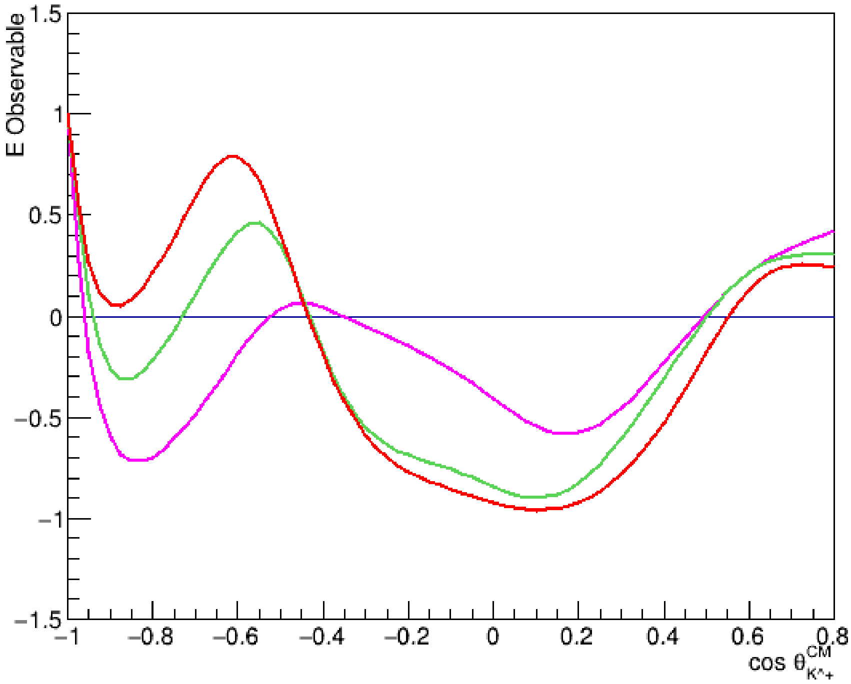

Figure 5.6: Predictions from KaonMAID for $\mathbb{E}$ in the reaction $\gamma n \rightarrow K^+\Sigma^-$. These are plotted every 200 MeV: 1900, 2100, 2300.

We see that at low energies ($< 1700\ MeV$), the prediction is largely featureless with only a minimum at backward angles ($cos\theta^{CM}_{K^+} \sim -0.8$). As the energy increases, the minimum widens and becomes more pronounced, as well as a second minimum developing at central angles ($cos\theta^{CM}_{K^+} \sim 0$). As photon energy continues to increase a maximum develops at small backward angles ($cos\theta^{CM}_{K^+} \sim -0.6$). As the energy limit of the KaonMAID model is reached, the backward minimum has become more pronounced and a very wide minimum at central angles has developed.

5.4.2 Bonn-Gatchina

Predictions from the Bonn-Gatchina model as a function of photon energy are shown in Figures 5.7 and 5.8. These predictions were requested from the Bonn-Gatchina group specifically for this analysis and include the most recent data on

1413 resonances[3].

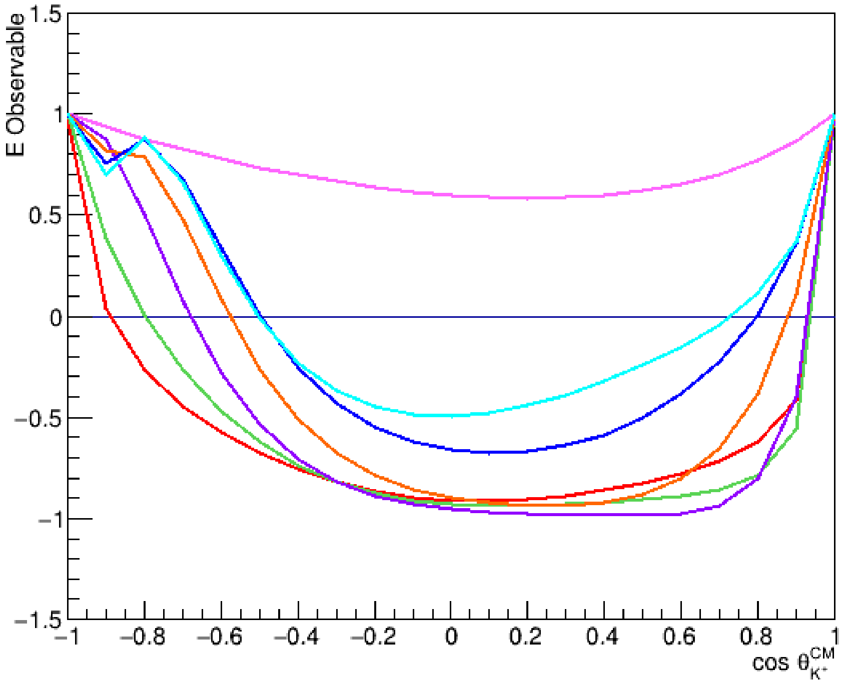

Figure 5.7: Predictions from Bonn-Gatchina for $\mathbb{E}$ in the reaction $\gamma n \rightarrow K^+\Sigma^-$. These are plotted every 100 MeV: 1050, 1150, 1250, 1350, 1450, 1550, 1650.

[3]Predictions received from Andrey Sarantsev of the Universität Bonn in May 2016.

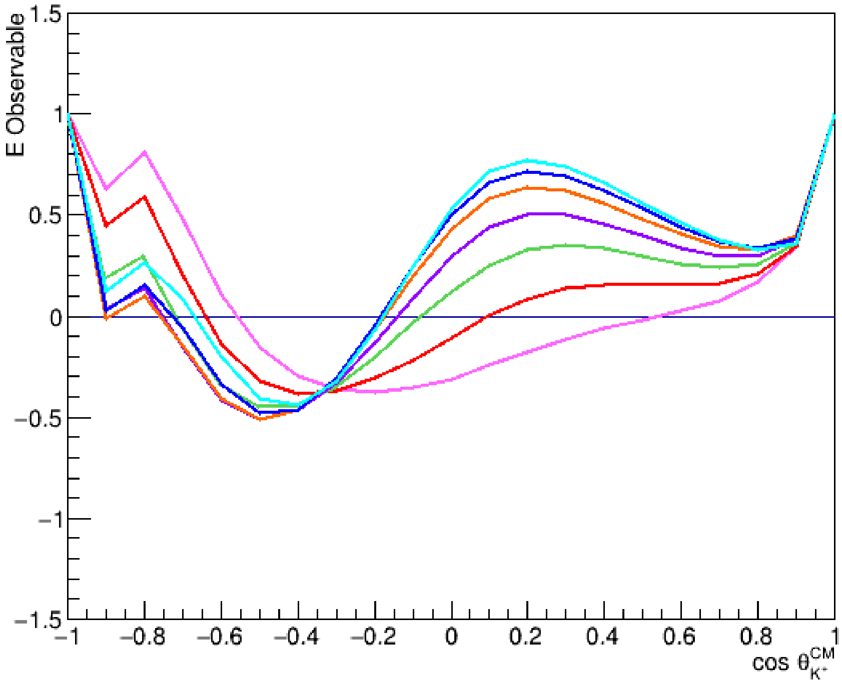

Figure 5.8: Predictions from Bonn-Gatchina for $\mathbb{E}$ in the reaction $\gamma n \rightarrow K^+\Sigma^-$. These are plotted every 100 MeV: 1750, 1850, 1950, 2050, 2150, 2250, 2350.

Similarly to KaonMAID, at low energies Bonn-Gatchina is largely featureless with a minimum at central angles, although this is much wider in the BoGa case. As the photon energy reaches $\sim$ 1450 MeV the prediction begins to see an additional minimum develop at very backward angles, as the central minimum thins. At photon energies of $\sim$ 1750 MeV the central minimum begins to shift towards backward angles while a central maximum begins to evolve, with a corresponding minimum at very forward angles.

It is clear that the KaonMAID and Bonn-Gatchina models are not currently in agreement for the $\mathbb{E}$ observable in the $\gamma n \rightarrow K^+\Sigma^-$ channel.

Chapter 6

Results and Discussion of the Double-polarisation Observable $\mathbb{E}$

This chapter will present the results of the analysis, describing the results of the polarisation observable $\mathbb{E}$ for the $\gamma n \rightarrow K^+\Sigma^-$ reaction. $\mathbb{E}$ will be compared to predictions from the KaonMAID model and the Bonn-Gatchina model, as these are the only theoretical models currently available for this channel.

6.1 $\mathbb{E}$ Observable Results Compared with Model Predictions

The results obtained for the $\mathbb{E}$ observable must be compared to the available theoretical models in order to be able to draw any conclusions from the analysis. As discussed in Section 1.3, the available models for this thesis are KaonMAID and Bonn-Gatchina and in the absence of available data with which to compare the results, model predictions are used[1].

6.1.1 KaonMAID

KaonMAID predictions for the $\mathbb{E}$ observable are compared with the $K^+\Sigma^-$ data in Figure 6.1. These KaonMAID predictions are shown for the extreme bin end points, corresponding to each bin of the experimental data[2]. This gives

[1] Only statistical errors are presented in this these final plots.
[2] The end point energies are indicated by blue for the lower edge and red for the upper edge.

an indication of the variation in the model predictions over the bin.

The experimental data for $\mathbb{E}$ generally shows a positive asymmetry for most of the measured photon energy range. The data near threshold has somewhat poorer statistical accuracy due to the smaller cross section. At the lower photon energies, the backward kaon angle data indicates a small or possibly negative asymmetry.

The KaonMAID model gives a reasonable description of the experimental data within statistical uncertainties up to photon energies around 1.5 GeV. Above this energy the model gives poorer agreement, predicting a smaller (and generally negative) asymmetry at backward and central angles than indicated in the data. Despite these discrepancies at backward and central angles, forward angles see reasonable agreement at these energies.

A clear point of interest is the poor agreement in the 1.5-1.7 GeV E_γ bin. It will be interesting to see the effects on the fit when new data is included.

6.1.2 Bonn-Gatchina

Bonn-Gatchina predictions for the $\mathbb{E}$ observable are compared with the $K^+\Sigma^-$ data, in Figures 6.2. Once again the predictions are included for the bin end point energies.

The Bonn-Gatchina predictions do not show very significant variation across the experimental bins, with predictions from the bin edges indicating similar trends and magnitude. The Bonn-Gatchina model predicts more negative asymmetries than KaonMAID for photon energies below 1.7 GeV. This behaviour is not well reflected in the data, as we see a clear difference in sign between the model and data at central kaon angles. At higher photon energies the smaller predicted asymmetries show better general agreement with the data within uncertainties. The Bonn-Gatchina model is constrained by a much larger database including recent meson photoproduction data, so this poorer agreement is interesting.

6.2 Summary

The first measurement of the $\mathbb{E}$ observable for $\gamma n \to K^+\Sigma^-$ has been extracted.

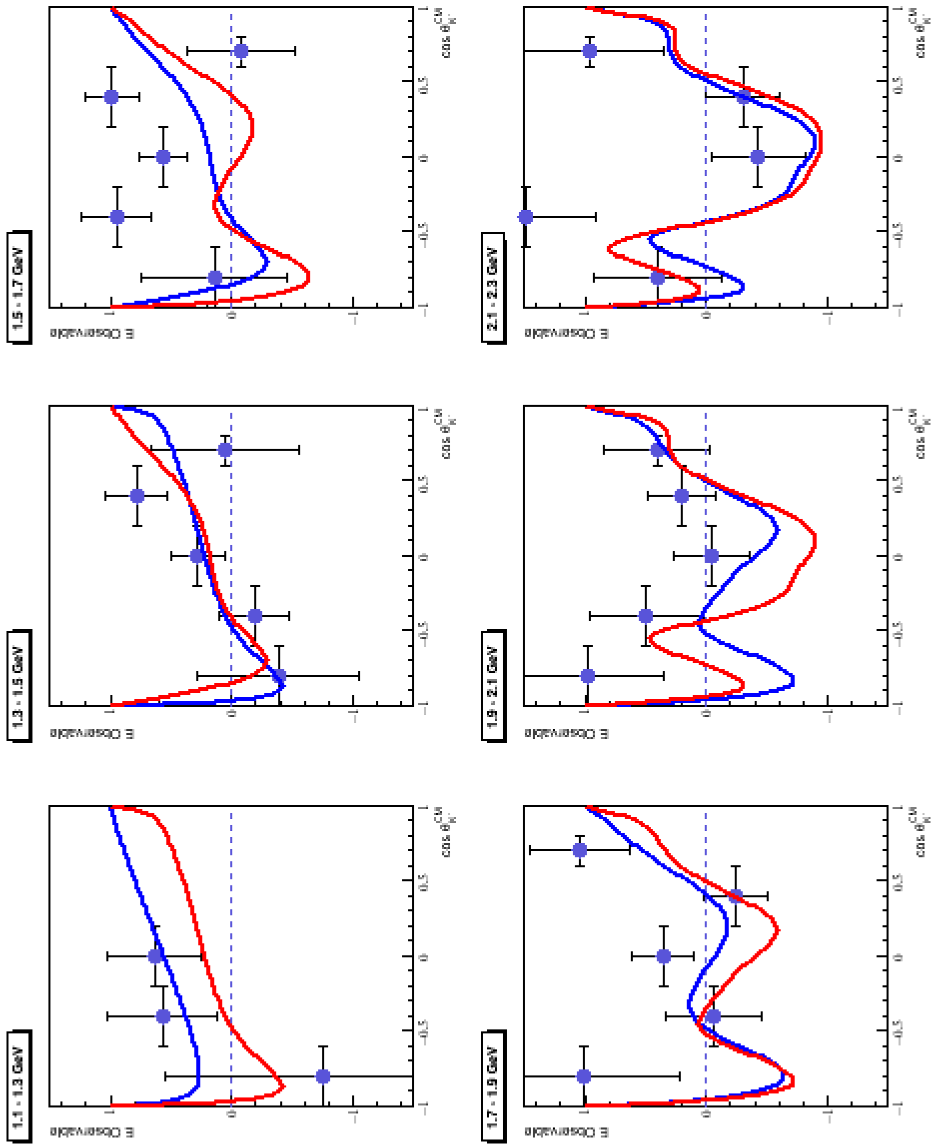

Figure 6.1: Results for the $\mathbb{E}$ double-polarisation observable including the bin end point predictions from KaonMAID.

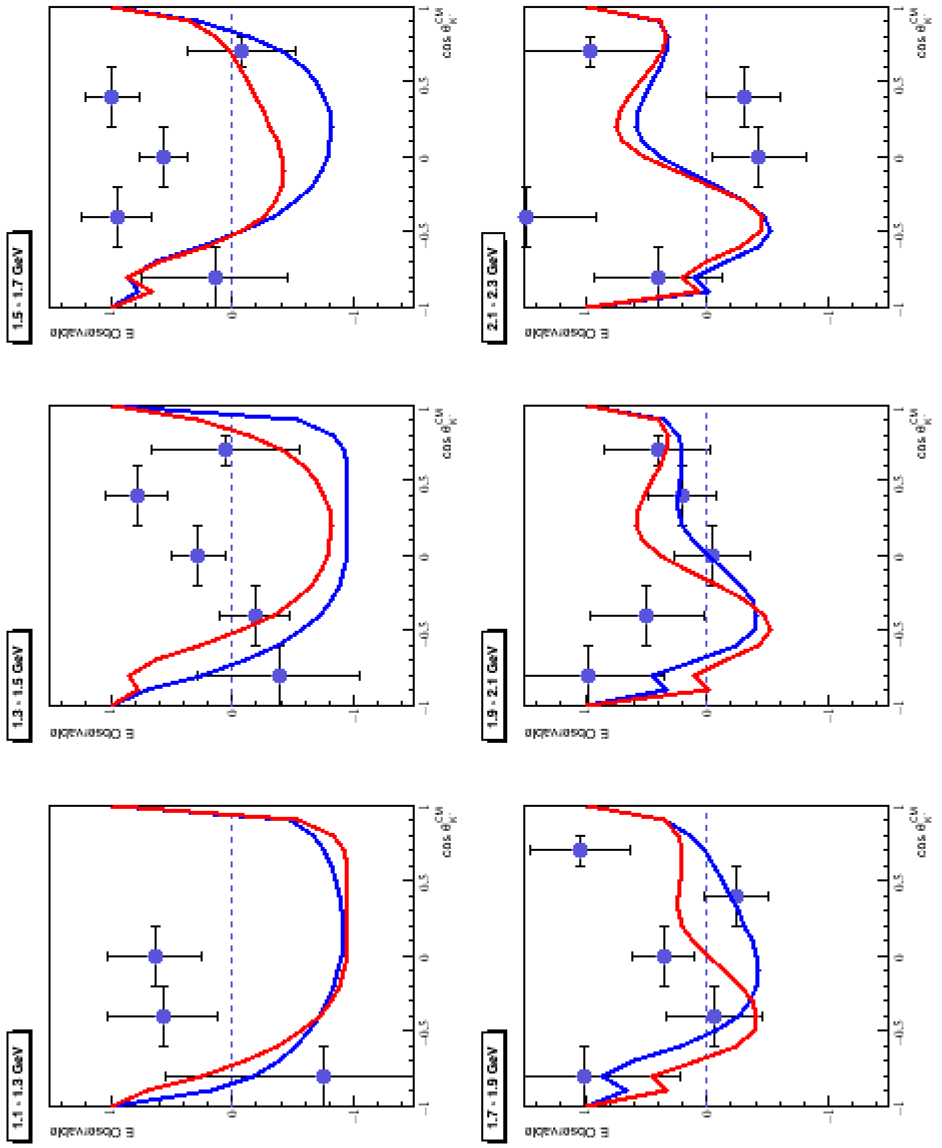

Figure 6.2: Results for the $\mathbb{E}$ double-polarisation observable including the bin end point predictions from Bonn-Gatchina.

The results were compared with the latest available reaction models for the process. These give divergent predictions for this observable for certain regions of photon energy and kaon angle. The KaonMAID tends to give better agreement in the lower photon energy ranges while at higher photon energies, both KaonMAID and Bonn-Gatchina give similar, although imperfect agreement. The sign difference seen, particularly in the $1,5$-1.7 GeV energy bin, provides some interesting insight in the data.

The new experimental data will provide valuable constraints on these models and the properties of nucleon resonances contributing at these photon energies. Definitive physics conclusions will await the new data being incorporated into the database for these models and systematic studies of the effect on resonance properties.

Chapter 7

Conclusions

A measurement of the double-polarisation observable $\mathbb{E}$ has been presented for the $K^+\Sigma^-$ channel from the $g14$ ($HDice$) run period at CLAS. These results were presented in the photon energy (E_γ) range 1.1-2.5 GeV and the complete range of the cosine of the kaon centre-of-mass angle ($\cos\theta^{CM}_{K^+}$). The modest statistics of the data allowed for a bin width of 200 MeV in E_γ and 0.4 in $\cos\theta^{CM}_{K^+}$. This measurement represents the first measurement of the $\mathbb{E}$ double-polarisation observable for the $K^+\Sigma^-$ channel.

The data were compared with the current solutions of two theoretical models, KaonMAID and Bonn-Gatchina. These gave divergent predictions for the observable and the new data gave better agreement with KaonMAID at low E_γ ($< 1.5\ GeV$), and showing broad agreement with KaonMAID and Bonn-Gatchina at higher E_γ. The new data will be an important new constraint on these models. More definitive physics conclusions regarding nucleon resonance properties will await the new data being incorporated into the theoretical predictions, for example probing which resonances could contribute to the sign difference noted between 1.5-1.7 GeV. This will occur after the data is published.

Future analysis of the channel would benefit from the capability of achieving a sufficiently large data sample in which the final state neutron is also detected. This would allow cleaner event identification (removing the largest systematic error in the current analysis) and also allow more restrictions on the spectator proton momentum to reduce potential contributions from final state interactions. However, the current data is an important first step.

Bibliography

[1] I.S. Barker and A. Donnachie. Complete Experiments in Pseudoscalar Photoproduction. *Nucl. Phys. B*, 95:347–356, 1975.

[2] S. Strauch et al. First Measurement of the Polarization Observable E in the $p(\gamma, \pi^+)n$ Reaction up to 2.25 GeV. *Phys. Lett. B*, 750:53, 2015.

[3] A.M. Sandorfi et al. Determining Pseudoscalar Meson Photo-production Amplitudes from Complete Experiments. 2011. arXiv:nucl-th/1010.4555v2.

[4] A.V. Anisovich et al. The Impact of New Polarization Data from Bonn, Mainz and Jefferson Laboratory on $\gamma p \to \pi N$ Multipoles. 2016. arXiv:nucl-th/1604.05704v1.

[5] F.X. Lee et al. Quasifree Kaon Photoproduction on Nuclei. *Nucl. Phys. A*, 695:237, 2001.

[6] X. Cao. Disentangling the Nature of Resonances in Coupled-channel Models. *Chinese Phys. C*, 39:041002, 2015.

[7] Andrey Sarantsev. Properties of Baryons from Bonn-Gatchina Partial Wave Analysis. *JPS Conf. Proc.*, 10:010005, 2016.

[8] J. McAndrew. *Measurement of the G Double-Polarisation Observable in Positive Pion Photoproduction.* PhD thesis, University of Edinburgh, 2011.

[9] G. Rouille et al. A Polarized HD Target Factory in Europe. *Nucl. Inst. Meth. A*, 464:428–432, 2001.

[10] F. Klein et al. N Resonances in Pseudo-scalar Meson Photo-production from Polarized Neutrons in HD and a Complete Determination of the $\gamma n \to K^{\circ}\Lambda$ amplitude. *HDice Proposal*, 2010.

[11] V. Laine. *Polarimetry of the Polarized Hydrogen Deuteride HDice Target Under an Electron Beam.* PhD thesis, Universite Blaise Pascal, 2013.

[12] D.H. Ho. *Measurement of the E Polarisation Observable for $\gamma d \to \pi^- p(p_s)$, $\gamma d \to K^0\Lambda(p_s)$, and $\gamma d \to \pi^+\pi^- d(0)$ using CLAS g14 Data at Jefferson Lab.* PhD thesis, Carnegie Mellon University, 2015.

[13] V. Blobel. *The BOS System for CLAS Detector.* Institut für Experimental Physik, Universität Hamburg, 1995.

[14] D. Ho et al. E Asymmetry for $\gamma n \rightarrow \pi^- p$ from $g14$ (HDice) Data, CLAS Analysis Note 2016. Currently in review.

[15] CERN. ROOT a Data Analysis Framework. `https://root.cern.ch/`.

[16] K. Livingston. RootBeer. `http://nuclear.gla.ac.uk/~kl/rootbeer/manual/html/rootbeer.php`.

[17] E. Pasyuk. A Brief User Guide to GPID, CLAS NOTE 2007-008.

[18] I. Zonta. *Polarization Observables from* $2-$*pion and* ρ *Meson Photoproduction on Polarized HD target at JLab*. PhD thesis, Universita Delgi Studi di Roma, 2014.

[19] S. Brandt. *Statistical and Compuattional Methods in Data Analysis*. North Holland Publishing Company, 1970.

[20] Jefferson Lab. JLab Picture Exchange. `http://www1.jlab.org/ul/jpix`.

[21] M. Williams. *Measurement of Differential Cross Sections and Spin Density Matrix Elements along with a Partial Wave Analysis for* $\gamma p \rightarrow p\omega$ *using CLAS at Jefferson Lab*. PhD thesis, Carnegie Mellon University, 2007.

[22] E. Pasyuk. Energy Loss Corrections for Charged Particles in CLAS, CLAS Internal Report: CLAS-Note 2007-016 2007.

[23] E. Munevar. *Photon Beam Asymmetry Measurement from the* $\gamma n \rightarrow K^+\Sigma^-$ *Reaction*. PhD thesis, George Washington University, 2014.

[24] S.A Pereira et al. Differential Cross Section of $\gamma n \rightarrow K^+\Sigma^-$ on Bound Neutrons with Incident Photons from $1.1 - 3.6$ GeV. *Phys. Lett. B*, 688:289–293, 2010.

[25] B.A. Mecking et al. The CEBAF Large Acceptance Spectrometer. *Nucl. Inst. Meth. A*, 503:513, 2003.

[26] H. Olsen and L.C. Maximon. Photon and Electron Polarization in High-Energy Bremsstrahlung and Pair Production with Screening. *Phys. Rev.*, 114:887, 1959.

[27] Institut für Kernphysik. An effective Lagrangian Model for Kaon Photo- and Electroproduction on the Nucleon. `http://portal.kph.uni-mainz.de/MAID//kaon/`.